# Self-propelled droplet driven by Marangoni flow and its applications

Dissertation

zur Erlangung des Grades

des Doktors der Naturwissenschaften

der Naturwissenschaftlich-Technischen Fakultät

der Universität des Saarlandes

von

Menglin Li (Leonard)

Saarbruecken

(2019)

Tag des Kolloquiums: 02.12.2019

Dekan: Prof. Dr. Guido Kickelbick

Berichterstatter: Prof. Dr. Ralf Seemann
Jun.-Prof. Dr. Franziska Lautenschläger

Vorsitz: Prof. Dr. Michael Vielhaber
Akad. Mitarbeiter: Dr. Christian Spengler

# Contents

# Summary

We developed a new class of self-propelled droplet, which is made of water/ethanol dispersed in squalane/monoolein. During the propulsion, a spontaneous phase separation of the droplet occurs due to the release of ethanol and the uptake of monoolein. This phase separation can lead to the formation of a Janus droplet consisting of a water-rich phase and an ethanol-rich phase. The droplet moves as a pusher, which is determined by $\mu$PIV, before the phase separation and as a neutral squirmer after it. The time before phase separation can be quantified by a model. Additionally the quantitative analysis of the driving mechanisms before and after the phase separation are presented.

Depending on salt concentration, added DNA or RNA can be controlled to accumulate either in the water-rich or in the ethanol-rich phase as a 'cargo'. This 'cargo' can be selectively delivered to a target controlled by hydrodynamic interaction and wettability.

The same water/ethanol droplet in an ethanol-saturated squalane shows chemotaxic attraction. In this system, the droplet uptakes ethanol from squalane and droplets are attracted to each other supposably driven by this ethanol gradient, which is created by themselves.

Large numbers of droplets can form patterns with different shapes, which is controlled by number density and vertical confinement.

Keywords: self-propelled droplet, cargo delivery, chemotaxis, collective behavior

# Kurzzusammenfassung

Wir haben eine neue Klasse von selbst-angetriebenen Tropfen entwickelt, die aus Wasser / Ethanol bestehen und in Squalan / Monoolein dispergiert sind. Während der Bewegung kommt es zu einer spontanen Phasentrennung des Tropfens aufgrund der Abgabe von Ethanol und der Aufnahme von Monoolein. Diese Phasentrennung kann zur Ausbildung eines Janus-Tropfens führen, der aus einer wasserreichen Phase und einer ethanolreichen Phase besteht. Der Tropfen bewegt sich vor der Phasentrennung als 'Pusher', der durch $\mu$PIV bestimmt wird, und danach als neutraler 'Squirmer'. Die Zeit vor der Phasentrennung kann durch ein Modell quantifiziert. Zusätzlich wird die quantitative Analyse der Antriebsmechanismen vor und nach der Phasentrennung vorgestellt.

Abhängig von der Salzkonzentration kann die zugesetzte DNA oder RNA so gesteuert werden, dass sie sich entweder in der wasserreichen oder in der ethanolreichen Phase als "Ladung" ansammelt. Diese 'Ladung' kann selektiv an ein Ziel geliefert werden und durch hydrodynamische Wechselwirkung und Benetzbarkeit gesteuert werden.

Der gleiche Wasser/Ethanol Tropfen in ethanolgesättigten Squalan zeigt eine chemotaktische Anziehungskraft. In diesem System nehmen die Tropfen Ethanol aus Squalan auf und die Tropfen werden vermutlich durch diesen Ethanolgradienten, der von ihnen selbst erzeugt wird, voneinander angezogen.

Die Ansammlung vieler Tropfen können Muster bilden. Das Muster wird von der Tropfendichte und der vertikalen Ausdehnung kontrolliert.

Stichwörter: selbst-angetriebene Tropfen, Ladungs-Lieferung, Chemotaxis, kollektives Verhalten

# Chapter 1

# State of the art

To see a World in a Grain of Sand
And a Heaven in a Wild Flower,
Hold Infinity in the palm of your hand
And Eternity in an hour.
-translated by William Blake from Avatamsaka Sutra, Buddhist texts

There is a complete different world on small scale. Now we know that a drop of water can contain thousands of tiny organisms. Since the microscope was invented by an unknown Dutch, people started to take a close look at the 'small world'. In 1670s, Antonie van Leeuwenhoek observed red blood cells under microscope and later reported the discovery of micro-organisms [1]. In 1866, Karl Moritz Diesing reported single-cell microorganism with flagella for the first time [2].

## 1.1 Biological microorganism

A flagellum is a hair-like appendage from certain bacterial cells and cells move by striking flagella [3]. But the swimming behavior in confinements on the micrometer scale is very different from it in the macro-world as we intuitively know. One of the primary differences is that swimmers on the micro-scale swim at low Reynolds numbers [4], which means viscous dominates over inertia. In this situation, when a bacteria strike once, the body move forward and when the forward propulsion stops, the bacteria stops immediately. And if the bacteria move the 'arm' back along the track, the body will go back to the original point.

To break the symmetry [4], microorganisms developed different modes moving flagella. A Chlamydomonas reinhardtii (an alga) propels itself by moving its two flagella like a breaststroke swim [5][6][7] (Fig. 1.1a). A sperm cell propels itself by striking a single flagellum behind it left and right [8][9] (Fig. 1.1b). An E. coli cell has up to ten helical flagella and it moves by rotating the flagella like a screw [10][11] (Fig. 1.1c). A Paramecium cell is covered by many short 'flagella' (cilia) and the cilia move synchronized in one direction. This synchronized movement creates a flow

and propels the cell move [12] (Fig. 1.1d).

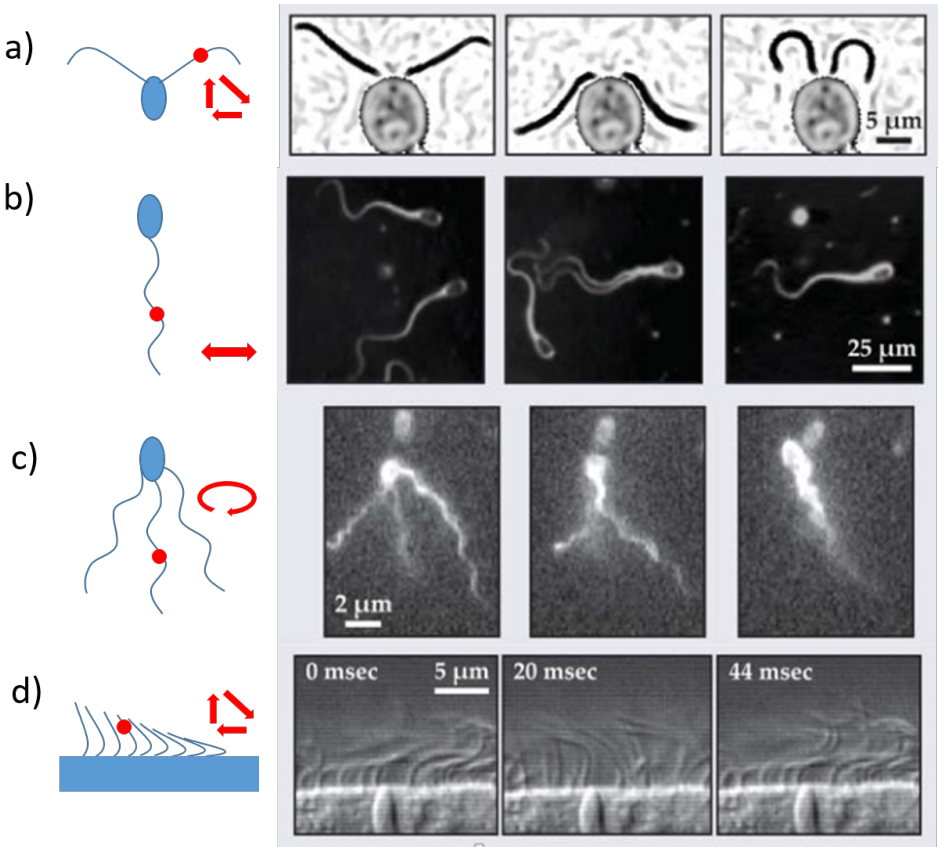


**Figure 1.1: Sketches and snapshots of different types of flagella.** a) A Chlamydomona cell (reprinted from [5] with permission from AAAS), b) sperm cells (reprinted from [9] with permission), c) an E. coli cell (Reprinted by permission from [11]) and d) the surface of a Paramecium ([12], copyright MBoC).

The nature of the swimming mode (how microorganisms striking flagella) decides the flow field around the cell. Pushers, including sperm cells and E. coli, propelled by trailing flagella. They repel surrounding fluid at the head and tail and draw it on the sides. They generate a dipolar field as indicated in Fig. 1.2a. In contrast, pullers such as Chlamydomonas pull the fluids from the head and tail and generate the opposite flow field [13] (Fig. 1.2b).

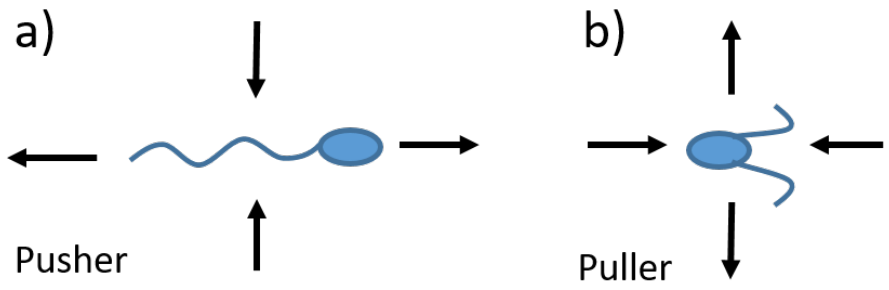


**Figure 1.2: A sketch of flow field around pusher and puller.** The arrows indicate the flow directions.

## 1.2 Janus particles

Recently there are many artificial microswimmers designed to simulate the movement of microorganisms and to understand their propulsion mechanism and collective behavior with controlled chemical or physical interactions. Although the driving mechanism of artificial microswimmers are different from the propulsion of microorganism stroking flagella, artificial microswimmers can be characterized by the same method based on flow field [14]. Consider about a spherical particle propelled by a certain tangential flow on the surface. If the tangential flow at the rearing end is stronger, the squirmer is characterized as a pusher. In contrast, if the tangential flow is stronger at the leading end, the squirmer is characterized as a puller (Fig. 1.3). If the tangential flow is uniform, it is characterized as a neutral squirmer.

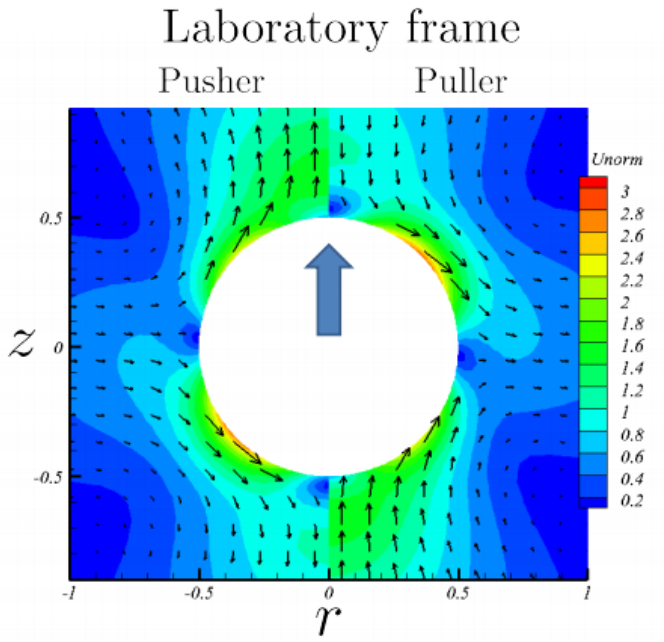


**Figure 1.3: Simulation of flow field around spherical squirmer (pusher (left) and puller (right)).** (Reprinted from [16], with the permission of AIP Publishing.) The color code indicates the flow velocity.

Janus particles are one representative category of artificial microswimmers. They are named after the Roman god Janus with two faces because these particles have two different physical properties [17], like hydrophilic/hydrophobic or different light absorption rate. In general, Janus particles can create a local (temperature or chemical) gradient by themselves to break the symmetry [4] and drive the motion.

There are different types of Janus particles breaking the symmetry by self-diffusiophoresis [18] [19] [20] [21], self-thermophoresis [22] and self-electrophoresis [23] [24] [25]: In [20], when a polystyrene sphere with a platinum cap is put in hydrogen peroxide solution, only platinum catalyzes the local decomposition of hydrogen peroxide into water and oxygen (Fig. 1.4a). The asymmetric distribution of reaction products

propels the particle by self-diffusiophoresis. In [22], Janus particles are made of 1 $\mu m$ silica with Au coating on only one side. By applying a laser beam, the Au cap absorbs more heat and generates a temperature difference between the two sides of the Janus particle. Then the Janus particle diffuses in this temperature gradient (Fig. 1.4b). In [24], a micro-rod is coated with Pt and Au on the respective side and put in hydrogen peroxide solution. On the Pt end, hydrogen peroxide is oxidized and generate protons in solution. On the Au end, protons and electron are coupled to the reduction of $H_2O_2$. This chemical reaction results in ion flux on the surface of the micro-rod and in the solution (Fig. 1.4c). The generated electric field propels the micro-rod toward the platinum end.

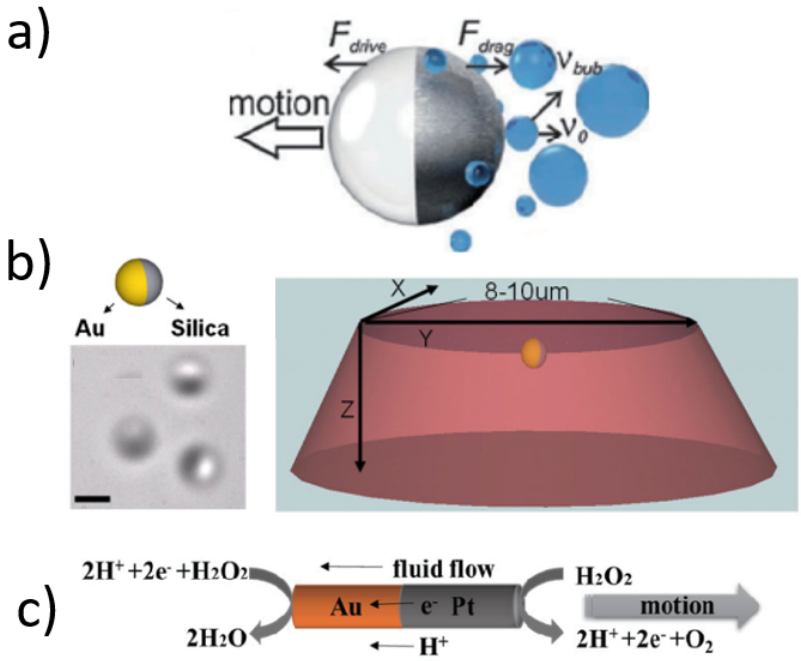


**Figure 1.4: Different types of Janus particles.** a) The platinum coating on the Janus droplet catalyzes hydrogen peroxide into water and oxygen (Reprinted figure with permission from [20]. Copyright (2007) by the American Physical Society). b) An Au coated Janus particle in the laser spot (indicated in dark red. Reprinted figure with permission from [22]. Copyright (2010) by the American Physical Society). c) A micro-rod coated with Pt and Au oxidizes hydrogen peroxide and propels in hydrogen peroxide solution (Reprinted with permission from [24]. Copyright (2006) American Chemical Society).

As mentioned in the previous example, it is a common strategy to fabricate Janus particles that are half side metal coated polystyrene. But with heavy metal coating (e.g. Au or Pt), some processes of the propulsion (e.g. laser) and the often agressive environment (e.g. hydrogen peroxide), Janus particles are not desirable for biological applications.

## 1.3 Self-propelled droplets

Self-propelled droplets, on the other hand, are more bio-compatible. They are mostly driven by Marangoni flow, which is a flow due to surface tension gradient. In this context, surface tension gradient / Marangoni flow occurs on the interface of the droplets. The surface tension gradient is caused by a chemical reaction [26] [27] [28] [29] or a phase transformation [30] [31] [32] [33]. For instance: in [26] it was shown that when a bromine-water droplet is put in monoolein (surfactant) oil solution, the droplet interface is covered by monoolein almost immediately. And due to the bromine inside the droplet, the monoolein on the interface will be brominated (Fig. 1.5). This chemical reaction decrease the surface activity of the surfactant, therefore increase the local surface tension on molecule level. If the brominated monoolein accumulate by chance preferentially on one side of a droplet, the Marangoni flow propels the droplet move on the opposite direction. As the droplet starts to move, fresh monoolein molecule in the oily phase will supply to the front end of the interface and maintain the interfacial tension gradient as long as the bromination reaction continues.

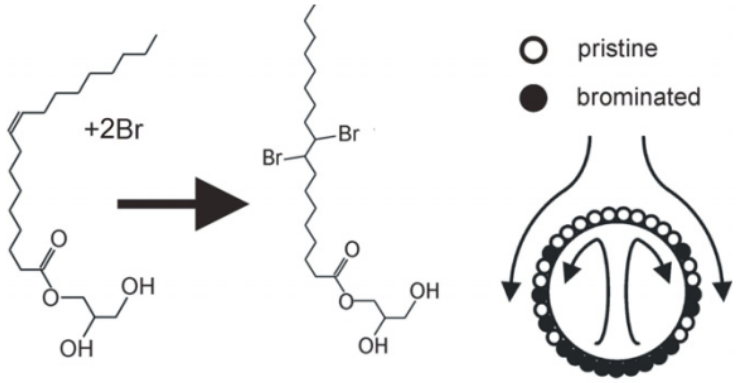


**Figure 1.5: A sketch of propulsion mechanism of bromine droplets [26].** Monoolein can be brominated and its surface activity is decreased (Copyright Institute of Physics and IOP Publishing Limited).

Another way of maintaining a surface tension gradient without chemical reaction was presented in [30]: liquid crystal droplet (5CB) starts to solubilize in Hexadecyltrimethylammonium bromide (TTAB) water solution by filling micelles. Micelles are filled with liquid crystal either when micelles impinge on the liquid crystal/water interface (micellar pathway, Fig. 1.6a) or freely diffusing liquid crystal molecules trapped in the suspended micelles (molecular pathway Fig. 1.6b). This solubilization reduce the local surfactant coverage on the droplet interface. When empty micellles approach the droplet by diffusion, they will disintegrate and increase the local surfactant coverage. This result in a Marangoni flow from the area with more empty micelles to the area with more filled micelles (Fig. 1.6c). This flow drives the droplet forward and maintain the surface tension gradient.

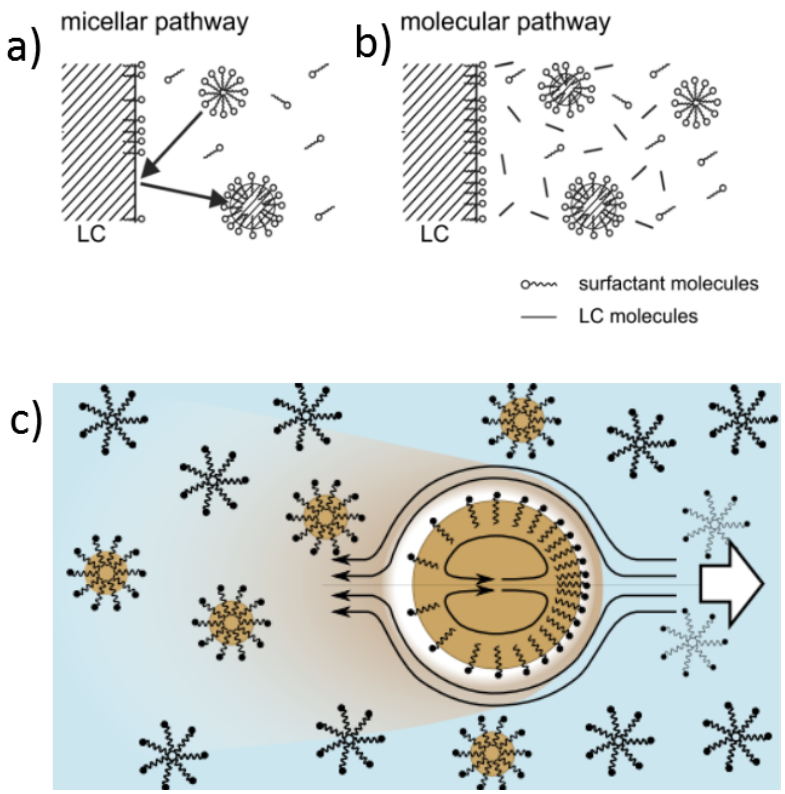


**Figure 1.6: A sketch of micellar and molecular path way and micelle transport by convection around a droplet (Reprinted with permission from [30]. Copyright (2012) American Chemical Society and [34], Copyright (2017) National Academy of Sciences).** a) Empty micelles uptake liquid crystal on the droplet interface. b) Liquid crystal is diffused into water and uptaken by empty micelles. c) Empty micelles are filled with liquid crystal (brown) and transported to the rear end of the droplet by convection flow.

## 1.4 Controlled directional motion

In general, artificial microswimmers show a random motion without the influence from chemical gradient or external field. On the other hand, chemical gradient and external field can be used to control the moving direction of artificial microswimmers [34] [35] [36] [37]. In [34], self-propelled droplets can solve the microfluidic maze by following the concentration gradient of surfactant, which is the 'fuel' of the self-propelled droplet (Fig. 1.7). In [37], Janus particles, which are driven by self-diffusiophoresis, move towards the gradient of fuel ($H_2O_2$) in microfluidic channels.

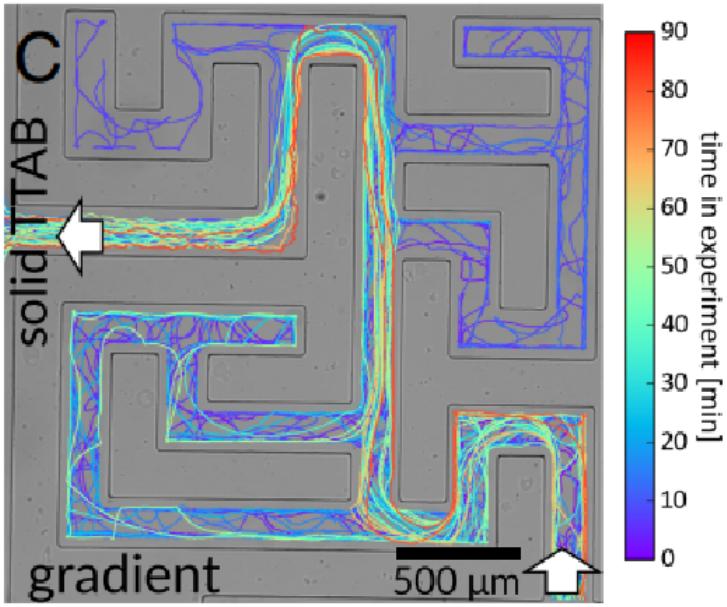


**Figure 1.7: Self-propelled droplets oriented by chemical gradient.** Trajectory frequency of the self-propelled droplets is higher along the path in the maze with high TTAB gradient [34] (Copyright (2017) National Academy of Sciences).

External magnetic field is widely used to guide microswimmers [38] [39] [40]. In [38], Janus particles are coated with a thin ferromagnetic or paramagnetic metal on one half of the surface. The Janus particles alone move by self-thermophoresis. Under an external magnetic field, the magnetic moments of Janus particles align along the symmetry axis (Fig. 1.8). Thus the direction of the movement can be controlled.

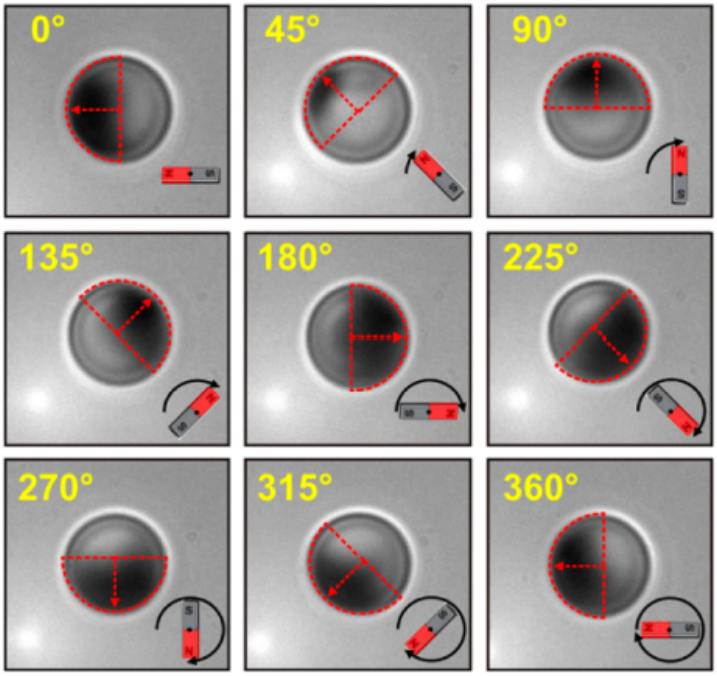


**Figure 1.8: An external magnetic field guides the orientation of the Janus particle (Reprinted with permission from [38]. Copyright (2013) American Chemical Society).**

Besides, a squirmer can induce a dimensionless attraction to the wall (or repulsion from the wall), which is dependent on the type of the squirmer (pusher, puller or neutral squirmer) and the orientation angles to the wall [41]. In the simulation from [42], when a single squirmer is oriented toward a infinite plane wall, the attraction toward the wall is stronger on a pusher than on a puller. In the simulation from [43], pushers are attracted by a round-shaped obstacle and can move around the obstacle while pullers are repelled by the obstacle. In [44], Janus particles, which are driven by self-diffisiophoresis, can move along straight and rounded obstacles (Fig. 1.9a,d). They can also move around a 90° corner (Fig. 1.9b) but not be able to follow a reflex angle of 270° (Fig. 1.9c).

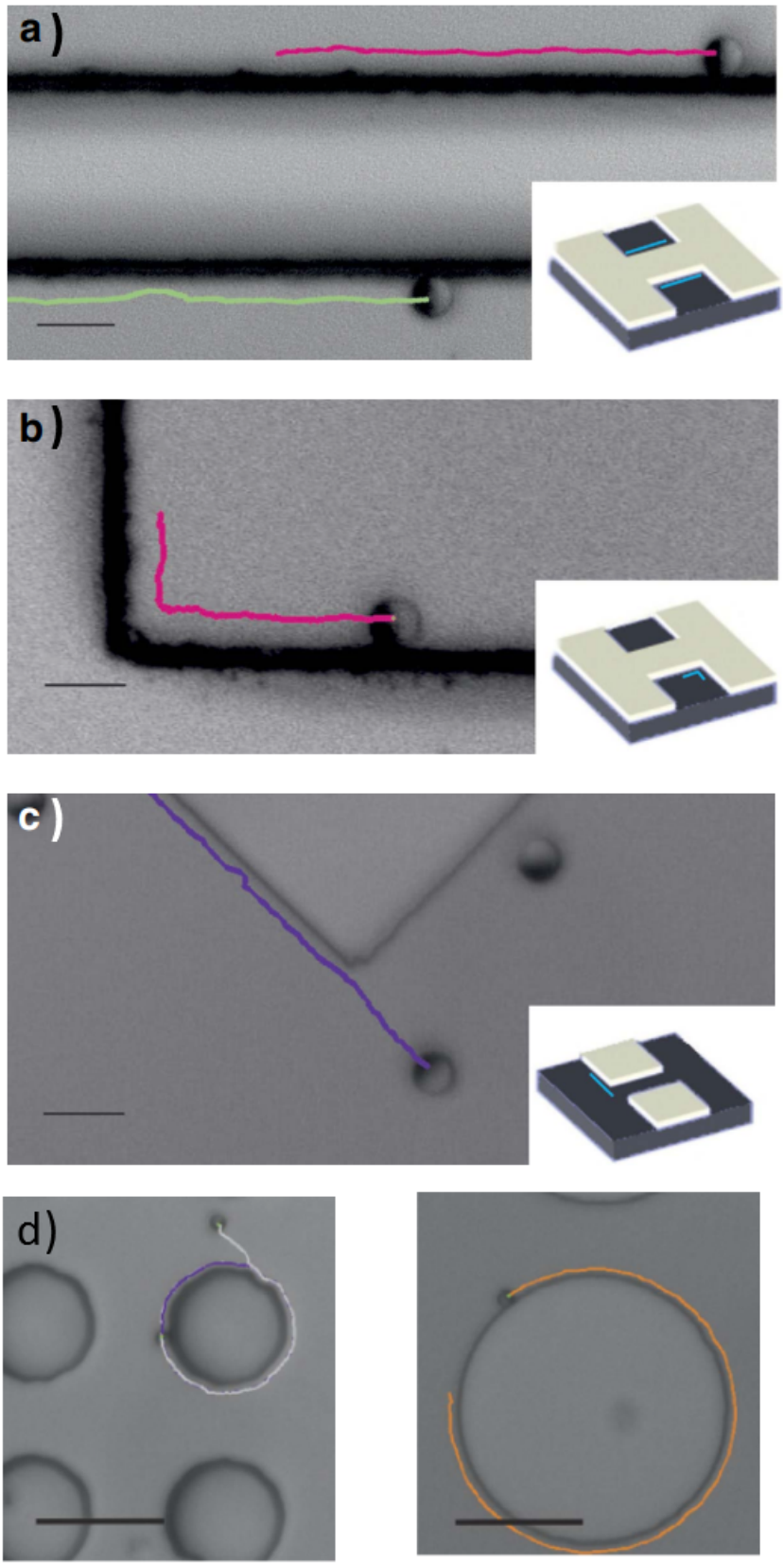


**Figure 1.9: Janus particles move along a) straight, b) 90°, c) 270° and d) rounded obstacles [44] (Copyright 2016, Springer Nature).** Scale bars are 10 $\mu$m in a-c) and 20 $\mu$m in d).

## 1.5 Collective behavior

By increasing the number density, the interactions between microswimmers become important and they show collective behaviors e.g. aggregation, orientation and formation of patterns. These collective behaviors are studied theoretically by simulations [45] [46] [47] [48] and by experiment [49] [50] [51] [52]. In the 2D simulation in [46], small rotational diffusion favors phase separation and the rotational diffusion is dependent from area fraction $\phi$ and squirmer mode. At low area fraction, no long-lived clusters exist. In contrast, swimmers can form a global cluster at high area fraction. The collective structures depend on the squirmer types. For neutral squirmers, the system separates in the gaslike and crystalline phase. Pushers develop a single cluster at area fraction $\phi$=0.64 while pullers form several hexagonal structures (Fig. 1.10).

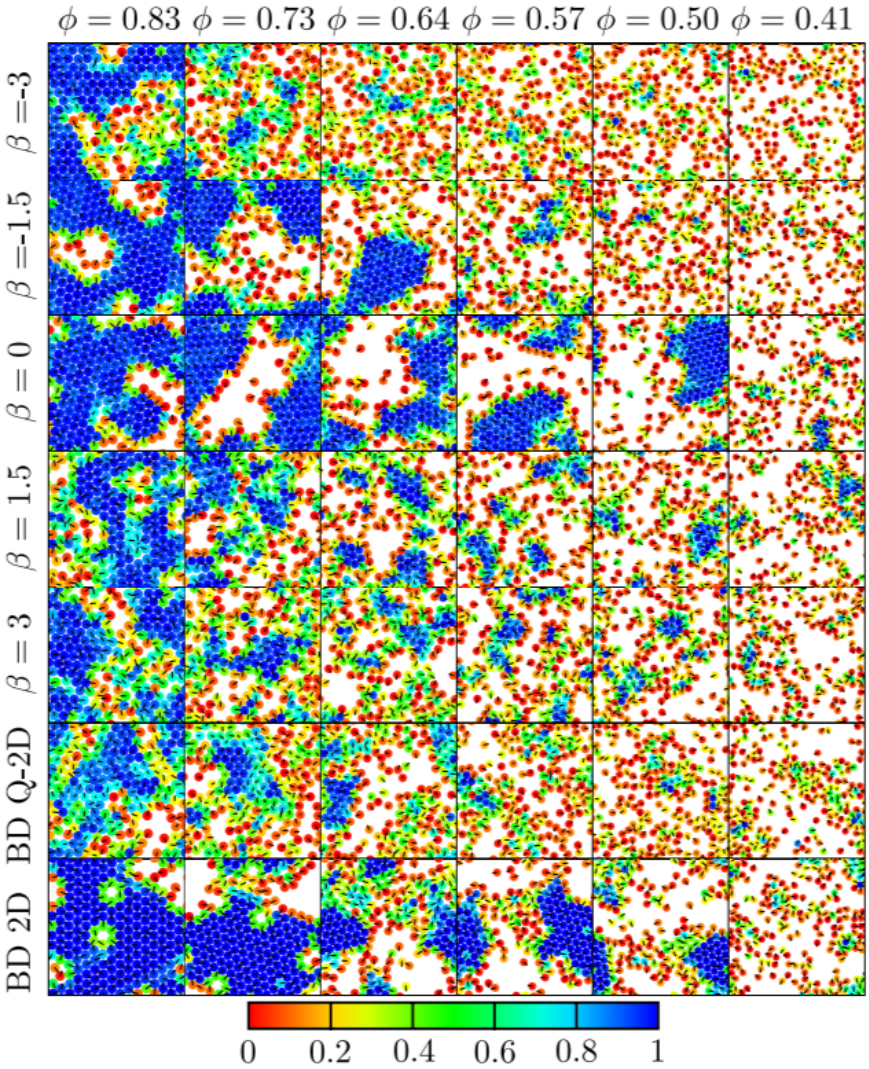


**Figure 1.10: Typical snapshots of the collective motion of squirmers in a quasi-2D geometry depending on the area fraction $\phi$ and the squirmer type ($\beta$).** (Reprinted figure with permission from [46]. Copyright (2014) by the American Physical Society) The colors indicate the local bond-orientational order.

In [50], Janus particles in $H_2O_2$ aggregate to living crystals when self-diffusiophoresis propulsion is turned on with a blue light. Living crystals melt by thermal diffusion when the light is off (Fig. 1.11a). In [49], active clusters made of liquid crystal droplets 'hover' in the continuous phase (Fig. 1.11b). The formation and the shape of these clusters can be controlled by the height of the reservoir. In quasi 2D confinement (reservoir height, H $\approx$ droplet diameter, d), there is no stable cluster. When H $\approx$ 4d, line-shaped clusters are formed. When H $\approx$ 10d, large and round-shaped clusters are formed (Fig. 1.11c).

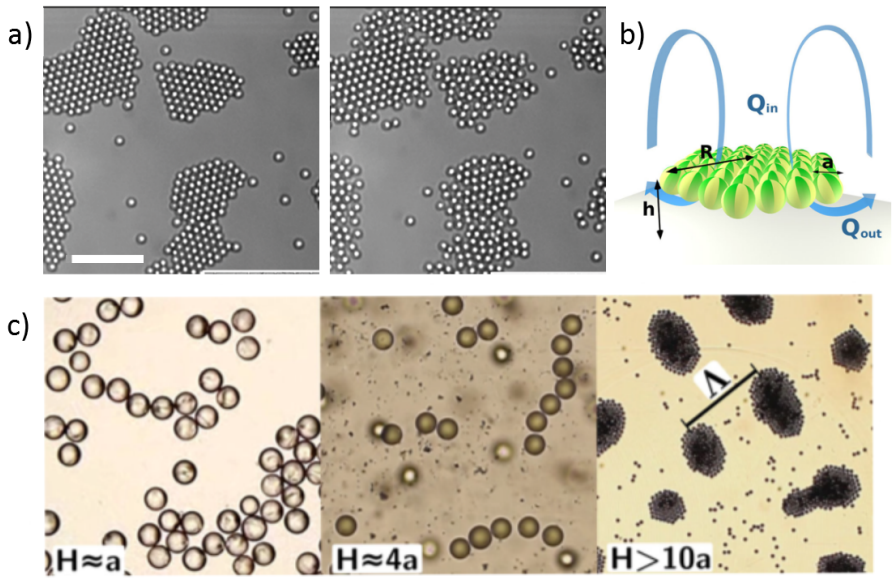


**Figure 1.11: Active clusters made of Janus particles and liquid crystal droplets [49].** a) Living clusters formation by propulsion (left) and deformation by thermal diffusion (Reprinted from [50] with permission from AAAS. The scale bar is 10 $\mu$m). b) A sketch of a living cluster 'hovered' by the convection flow (blue arrows). c) Collective behavior of liquid crystal droplets with different vertical confinements (The droplet diameter d $\approx$ 45 $\mu$m in all three images. The field of view are 0.5 $\times$ 0.5 $mm^2$ for the left and the middle and 2.5 $\times$ 2.5 $mm^2$ for the right image).

## 1.6 Application: cargo delivery

Drug delivery is an important application of microswimmers. Kagan et al. reported a type of nanomotors driven by catalysing $H_2O_2$ (self-diffusiophoresis) and oriented by magnetic forces. This nanomotor can pick up iron oxide-encapsulated polymer particles, transport and release the particles by fast reversal in the direction of the nanomotor [53] (Fig. 1.12).

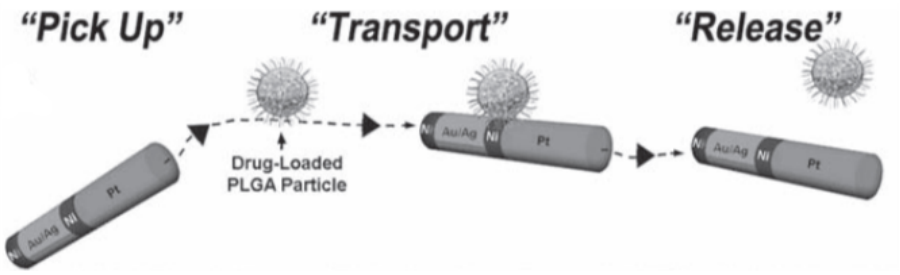


**Figure 1.12: A sketch of a nanomotor 'pick up', 'transport' and 'release' a cargo** [53] (Copyright Wiley Online Library).

# Chapter 2

# Theoretical background and experimental methods

Microfluidics is a useful tool controlling fluids on a micro scale. In our case, microfluidics is used to generate droplets that self propell and to study their movement. To understand the particular flow properties of these self-propelling droplets, the following concept of wetting and hydrodynamics are introduced.

## 2.1 Surface tension

It is an intrinsic property of a substance that molecules of the same kind attracting neighboring molecules. One molecular in the middle of the liquid is uniformly attracted by all neighbors, so the sum of the forces is zero. While the attraction force at the surface is only toward the liquid side (Fig. 2.1). This leads to a net force towards the liquid, surface tension.

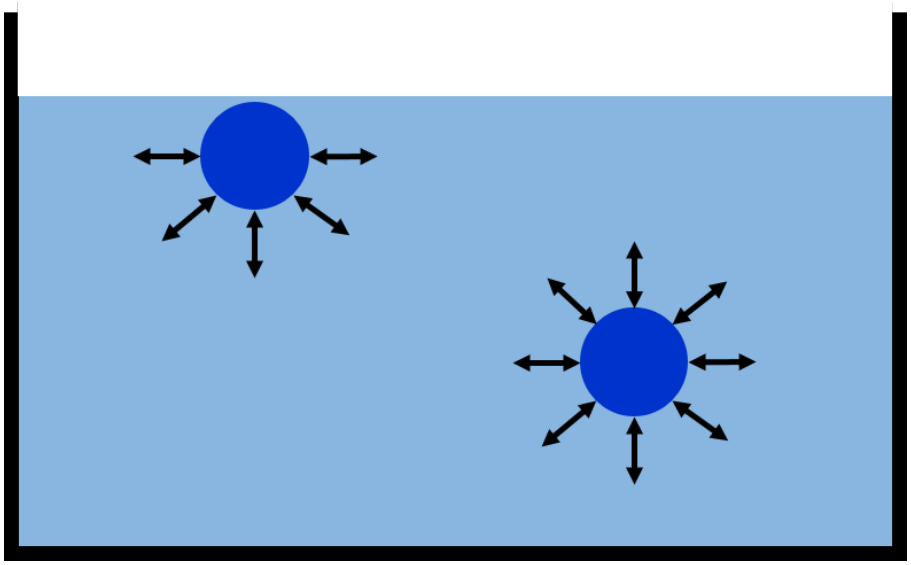

**Figure 2.1: An illustration of surface tension.** One molecule (dark blue disk) in the liquid is attracted by all neighbors. One molecule on the interface is only attracted from the liquid side. Black arrows indicate the attraction between liquid molecules.

The total surface energy is proportional to the area of the surface $A$:

$$E = \sigma * A \tag{2.1}$$

The free liquid-air interface tries to minimize its energy by reducing its surface area while keeping the pressure (Laplace pressure), which can be obtained from the local curvature constant:

$$\delta P = \sigma(\frac{1}{R_1} + \frac{1}{R_2}) \tag{2.2}$$

where $R_1$ and $R_2$ are the principal radii of curvature.

When the surface of the fluid is not to the air but in another fluid, it is referred to as interfacial tension.

One method measuring the interfacial tension is so-called 'pendant droplet'. A droplet is pushed out from a very thin needle (Fig 2.2) until reaching the maximum volume before the droplet is pinched off from the needle. It can increase the precision of the interfacial tension measurement by reaching the maximum volume of the droplet [54]. The shape of the pendant droplet is formed by both gravity and interfacial tension. The pendant droplet is recorded by a camera and the known diameter of the needle above is used as a length reference. A computer program (SCA 20 used in the experiments) calculates the interfacial tension $\sigma$ by analyzing the contour of the pendent droplet:

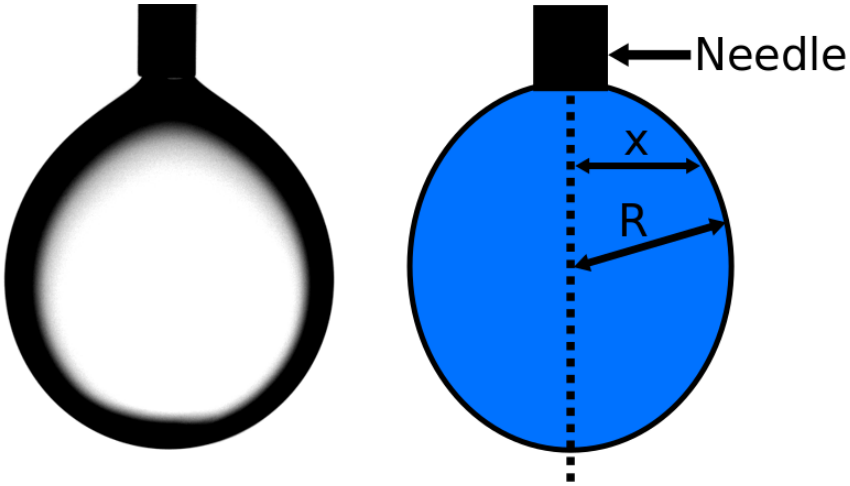


**Figure 2.2: A snap shot and a sketch of a pendant droplet hanging on a needle.** The contour of the droplet can be detected and redrawn by software. The outer diameter of the needle is 0.5 mm.

$$\sigma = \frac{gV\Delta\rho R}{\pi x^2} \tag{2.3}$$

where $\Delta\rho$ is the density difference between the droplet (normally heavier) and the surrounding liquid. $V$ is the volume of the droplet. $x$ is the horizontal distance between the surface and the middle axis of the droplet. $R$ is the principle curvature of the droplet (Fig 2.2).

### 2.1.1 Contact angle

When a liquid is brought to contact to a solid interface and surrounded by air, the three different phases will meet at the contact line.

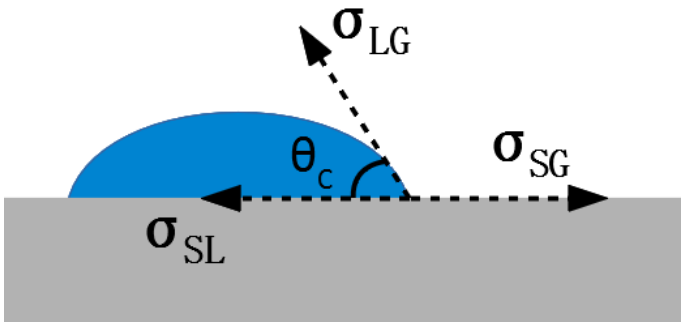


**Figure 2.3: An illustration of contact angle.** Contact angle is decided by the interfacial tensions between solid/gas, solid/liquid and liquid/gas.

The liquid reaches an equilibrium under three interfacial tensions, where the horizontal components of the interfacial tension are balanced. This defines the contact

angle as Young's equation:

$$\sigma SG - \sigma SL - \sigma LG \cos\theta_C = 0 \tag{2.4}$$

where $\sigma SG, \sigma SL$ and $\sigma LG$ stand for solid/gas, solid/liquid and liquid/gas interfacial tension respectively (Fig. 2.3). $\theta_C$ is the contact angle. The gas phase could be also another liquid. For $\theta_C = 0°$, the liquid forms a thin layer on the solid and the surface is completely wet by the liquid. For $\theta_C = 180°$, the liquid forms a sphere (when the volume of the liquid is small enough and gravitational forces can be neglected) and the solid surface is completely non-wetting for the liquid. For all the $\theta_C$ in between 0 and 180°, the surface is partially wet (Fig. 2.4).

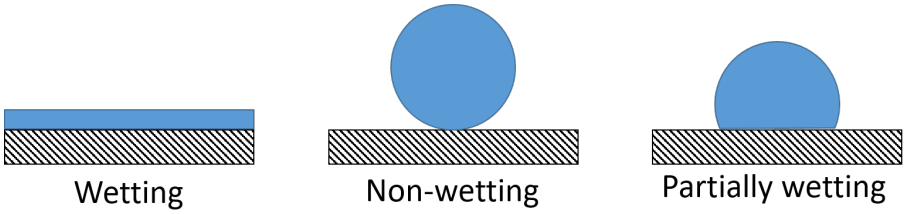


**Figure 2.4: An illustration of wetting property:** wetting, non-wetting and partially wetting. The blue indicates the liquid. The dashed rectangle indicates the substrate.

Our ethanol/water mixture droplet phase is typically forming a small contact angle with a glass substrate and becoming sessile droplets. To avoid this we apply octadecyl-trichlorosilane (OTS) and Teflon coating on the surface of the reservoir, so that ethanol/water mixture droplets have a high contact angle, therefore not likely to stick to the bottom.

### 2.1.2 Surfactants

Surfactant is short for surface active agent [55] [56] and it has a polar hydrophilic head and a non-polar hydrophobic tail (Fig. 2.5). With the amphiphilic structure, it is energetically favorable for surfactant molecules to stay at the interface with the head groups pointing towards the aqueous phase and the tails pointing towards the oily phase. In this way, surfactant effectively reduces the interfacial tension (Fig. 2.6a). By increasing surfactant concentration, the liquid-liquid interfacial tension decreases until the surfactant is saturated at the interface, respectively in equilibrium with the dissolved surfactant (Fig. 2.6b).

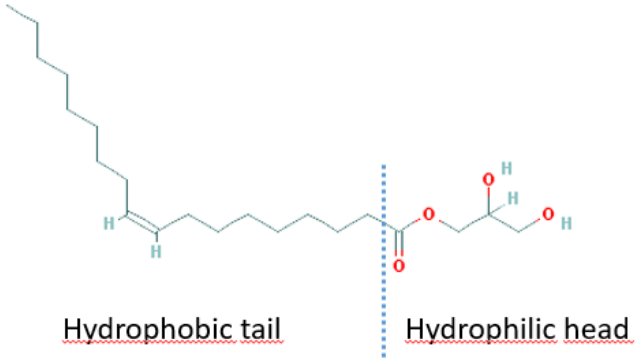


**Figure 2.5: Molecular structure of surfactants.** Surfactants have a hydrophilic head and a hydrophobic tail.

If surfactant concentration is further increased to a certain value, surfactant molecules start to aggregate to larger structures with hydropilic head pointing towards middle in an oily phase (or towards outside in an aqueous phase) to further decrease their energy (Fig. 2.6c). These large molecular structures are called micelles and the surfactant concentration when micelles start to form is called Critical Micellar Concentration (CMC). The process of micelle formation can be reversed when the surfactant concentration decreases and slow down the decreasing process below the CMC.

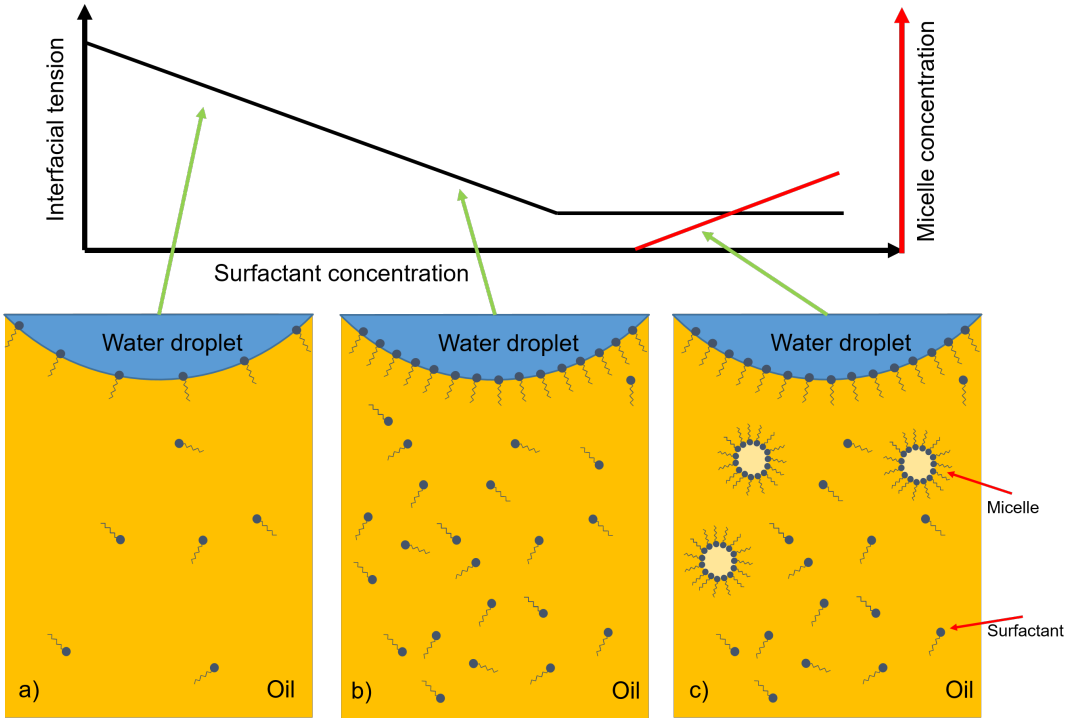


**Figure 2.6: A sketch of interfacial tension and micelle concentration as a function of surfactant concentration.** a,b) Surfactant prefer to go to an interface and stay there with hydrophilic head towards water phase and hydrophobic tail towards the oily phase. c) By increasing the surfactant concentration, some singular surfactant molecules form micelles with hydrophilic head towards middle and hydrophobic tail towards outside in the oily phase (or with hydrophilic head towards outside in an aqueous phase).

With sufficiently high surfactant concentration in the oily (continuous) phase, water droplets are almost immediately covered by surfactant once they are produced and the interfacial tension decreases. With low interfacial tension, it helps to stabilize the droplets. If the interfacial tension is high, droplets are unstable and they will merge with each other.

### 2.1.3 Marangoni effect

Marangoni effect is a flow along the interface between two liquids or liquid/air due to surface tension gradient [57]. The surface tension gradient could be caused by temperature gradient or (surfactant) concentration gradient. In Fig. 2.7, the liquid-air interface at the left side of the liquid surface has a lower surfactant coverage, therefore a higher surface tension than the right side. This generate a Marangoni flow from the right to the left.

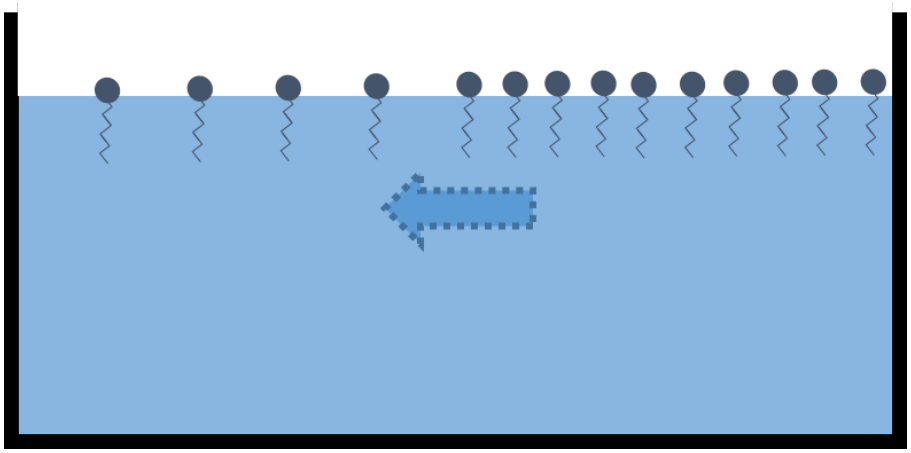

**Figure 2.7: An illustration of Marangoni effect.** The area with higher surface tension attracts surrounding stronger and causes Marangoni flow. The dark circle with a tail indicates surfactant molecules. The arrow indicates the flow direction.

In our experiment, we could create and maintain a surface tension gradient on the droplet. This surface tension gradient caused a Marangoni flow and propelled the droplet (Fig. 2.8).

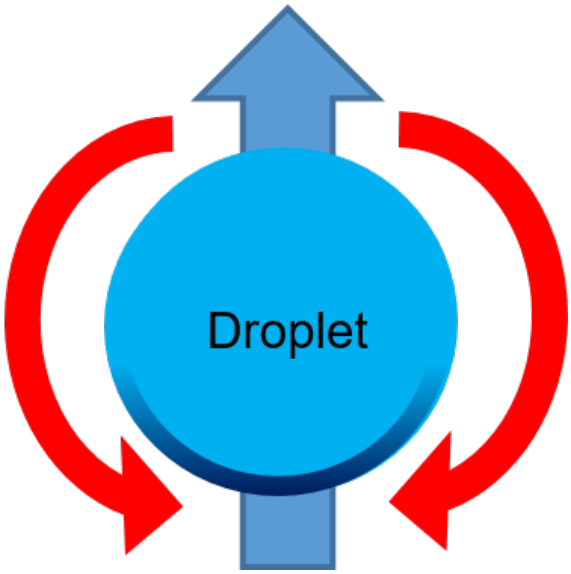


**Figure 2.8: A sketch of Marangoni flow on a droplet.** There is a Marangoni flow (red arrow) on the interface of a droplet from low surface tension area (light blue) to high surface tension area (dark blue). The grey arrow indicates the droplet moving direction.

## 2.2 Basic principles of microfluidics

In the last section, some capillary effects were introduced. In this section, Navier-Stokes equation will be introduced to describe hydrodynamics. The equation will

be simplified with several approximations.

To make it easier to understand these approximations, here is a brief description of the system in the experiment. Self-propelled droplets are produced by a T-junction-like device and later observed in a quasi 2D reservoir (the height of the reservoir is slightly larger than the diameter of the droplets). Self-propelled droplets swim at 10 $\mu$m/s.

### 2.2.1 Navier-Stokes equation

In general, all simple flows (incompressible and Newtonian fluid) can be described by the Navier-Stokes equation [58], which include gravity and friction.

$$\nabla \cdot v = 0 \tag{2.5}$$

$$\rho \frac{\delta \vec{v}}{\delta t} = -\nabla p + \rho \vec{g} + \mu \nabla^2 \vec{v} \tag{2.6}$$

Eqn. 2.5 indicates volume conservation (for incompressible fluid) and Eqn. 2.6 indicates impulse balance. $\rho \frac{\delta \vec{v}}{\delta t}$ is the inertial part, $-\nabla p$ is pressure gradient, $\rho \vec{g}$ are gravitational forces and $\mu \nabla^2 \vec{v}$ describes friction effects. Next, several dimensionless numbers will be introduced to simplify the equation.

### 2.2.2 Hele Shaw geometry

The reservoir in the experiment, where the movement of the droplets are observed, has a Hele-Shaw geometry [59], which means that the observed fluid is in between two parallel flat plates separated by an infinite small gap. In this case, we can consider that the shear along the vertical axis dominates.

### 2.2.3 Weber number

The relative importance between inertial forces and capillary forces is given by the Weber number:

$$We = \frac{\rho v^2 d}{\sigma} \tag{2.7}$$

where $d$ is the characteristic length ($\approx 10$ $\mu$m) and $v$ is the velocity of the flow (the propulsion velocity of the droplets in the experiment $v \approx 10$ $\mu$m/s typically). With the typical dimensions used in the experiment, the Weber number is about $10^{-8}$. Therefore the inertial force can be neglected comparing to the capillary forces.

### 2.2.4 Reynold number

Reynold number is a dimensionless number, which describes the ratio between inertial forces and viscous forces [4].

$$Re = \frac{\rho v d}{\mu} \tag{2.8}$$

where, $\mu$ is viscosity ($\mu_{squalane}$ = 36.1 mPa*s in the experiment). If $Re$ is much larger than a critical number $Re_{crit}$, the flow is turbulent. If $Re$ is much smaller than $Re_{crit}$, the flow is laminar. For rectangular channel $Re_{crit} \approx 2300$, while the Reynold number in the experiment is typically $1.5 * 10^{-4}$. Thus the flow is only laminar.

### 2.2.5 Stokes equation

Coming back to the Navier-Stokes equation. Considering the dimensionless numbers for our considered microfluidic system, gravity, inertia and turbulent flow in Eqn. 2.6 are neglected and it becomes

$$\mu \nabla^2 \vec{v} = \nabla p \tag{2.9}$$

This is so-called Stokes equation. This Stokes equation is linear and time independent, so time reversible. This is reflected by the 'scallop theorem': if the shape changes displayed by a swimmer are identical when viewed in reverse order, it will generate an oscillatory, but no directed motion [4].

### 2.2.6 Solution of Stokes equation

The Stokes equation 2.9 can be solved analytically for an unbounded system with an external force field. In our case, the velocity field around a (spherical) droplet is given by

$$\mathbf{v}(\mathbf{r}, t) = \int_t^0 \int \mathbf{H}(\mathbf{r} - \mathbf{r}', t - t') \cdot \mathbf{f}(\mathbf{r}', t') d^3 r' dt' \tag{2.10}$$

with the time and position dependent hydrodynamic tensor $\mathbf{H}(\mathbf{r}, t)$. With time independent $\mathbf{f}(\mathbf{r})$, integration over $t'$ in Eqn. 2.10 yields

$$\mathbf{v}(\mathbf{r}) = \int \mathbf{H}(\mathbf{r} - \mathbf{r}') \cdot \mathbf{f}(\mathbf{r}') d^3 r' \tag{2.11}$$

$\mathbf{H}(\mathbf{r})$ is the Oseen tensor with the Cartesian components [60] [61]

$$H_{\alpha\beta}(\mathbf{r}) = \frac{1}{8\pi\eta r}\left(\delta_{\alpha\beta} + \frac{r_\alpha r_\beta}{r^2}\right) \tag{2.12}$$

$\alpha, \beta \in \{x, y, z\}$ and $r = \mid \mathbf{r} \mid$. The Oseen tensor is the Green's function of the Stokes equation 2.6 when the point force $\mathbf{f}(\mathbf{r}) = \delta(\mathbf{r})\hat{\mathbf{e}}$ in the direction $\hat{\mathbf{e}}$ is employed. Then equation 2.11 yields

$$\mathbf{v}(\mathbf{r}) = \frac{1}{8\pi\eta r}\left(\hat{\mathbf{e}} + \frac{(\mathbf{r}\cdot\hat{\mathbf{e}})\mathbf{r}}{r^2}\right) \tag{2.13}$$

### 2.2.7 Stokes' drag

From the Stokes equation (Eqn. 2.9), we can also derive the viscous forces on a sphere moving through a viscous fluid, which is known as Stokes' drag [62]. We use a cylindrical coordinate system $(r, \phi, z)$. $z$-axis is aligned with the present flow direction. In this case, the flow can be described in $z$ and $r$ direction with a Stokes stream function $\psi$:

$$v_z = \frac{1}{r}\frac{\partial\psi}{\partial r},\ v_r = -\frac{1}{r}\frac{\partial\psi}{\partial z} \tag{2.14}$$

where $v_r$ and $v_z$ are the flow velocities in $r$ and $z$ direction respectively. Because the system is rotational symmetric, the velocity perpendicular to the flow in direction of $\phi$, the vorticity vector $\omega$ becomes

$$\omega_\phi = \frac{\partial v_r}{\partial z} - \frac{\partial v_z}{\partial r} = -\frac{\partial}{\partial r}\left(\frac{1}{r}\frac{\partial\psi}{\partial r}\right) - \frac{1}{r}\frac{\partial^2\psi}{\partial z^2} \tag{2.15}$$

The solution of the equation in the far field is

$$\psi = -\frac{1}{2}vr^2\left[1 - \frac{3}{2}\frac{R}{\sqrt{r^2+z^2}} + \frac{1}{2}\left(\frac{R}{\sqrt{r^2+z^2}}\right)^3\right] \tag{2.16}$$

with flow velocity $u$. The viscous force per unit area $\sigma$ on the sphere surface is $z$ direction and has the same value everywhere:

$$\sigma = \frac{3\mu v}{2R} \tag{2.17}$$

where $\mu$ is the dynamic viscosity of the liquid. The total viscous force acting on a sphere is

$$F_d = 6\pi\mu R v \tag{2.18}$$

### 2.2.8 Diffusion coefficient

Diffusion is a net flux of substances (e.g. molecules, particles) from higher concentration region to lower concentration region [63]. Diffusion coefficient, $D$ is a proportionality constant between the flux and the concentration gradient and determined by Einstein-Smoluchowski equation:

$$D = \frac{\langle x^2 \rangle}{t} \tag{2.19}$$

where $x$ is the average moving path of the transported substances and $t$ is the time. In a given liquid medium, the diffusion coefficent can be described by the Stokes-Einstein equation:

$$D = \frac{k_B T}{6\pi\eta R_0} \tag{2.20}$$

where $k_B$ is the Bolzmann constant ($1.38 * 10^{-23}$ J/K), $T$ is the temperature, $\eta$ is the dynamic viscosity of the solvent. $R_0$ is the hydrodynamic radius of the diffusive substance.

### 2.2.9 Peclet number

The Peclet number is defined as advective transport rate divided by diffusive transport rate [64]. For mass transfer, it is defined as:

$$Pe = \frac{Lv}{D} \tag{2.21}$$

where $L$ is the characteristic length of the droplet. In the experiment, the typical radius of the used droplets is 50 $\mu$m. The typical propulsion velocity is $v = 10$ $\mu$m/s. $D$ is the diffusion coefficient. In our system, self-propelling droplets absorb monoolein molecules (surfactant) and the absorption is essential for the propulsion of the droplets. The diffusion constant of the monoolein molecules in the squalane is around ($2.6 * 10^{-12}$ $m^2/s$) [26]. With these typical numbers used in the experiment, the Peclet number is about 200. Therefore mass transfer of monoolein molecules is dominated by advective flow.

## 2.3 Dipole and squirmer model

### 2.3.1 Dipole swimmer

Microswimmers move by themselves, with no external force applied. Therefore the total interaction force of the swimmer on the fluid vanishes. The far field hydrodynamics of many microswimmers can be well described by a force dipole [65] [66].

Two types of such dipole swimmers can be distinguished. If the 'motor' of the swimmer is in the back and the passive body drags along the surrounding fluid in front, the swimmer is a 'pusher' and the characteristic flow is shown in Fig. 2.9a. Similarly, if the 'motor' is in the front, and the passive body is behind, the swimmer is a 'puller' and the flow field is in Fig. 2.9b. Notice that the flow fields of a pusher and a puller look similar, but with opposite flow directions.

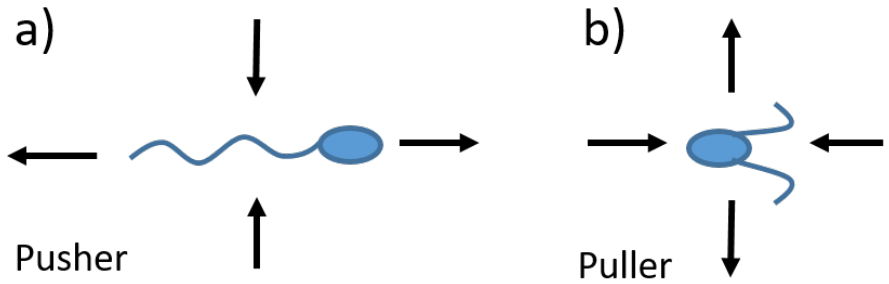


**Figure 2.9: A sketch of flow field around a pusher and a puller.** The arrows indicate the flow directions.

Mathematically, the flow field of a hydrodynamic force dipole located at $\mathbf{r}_0$ can be obtained from the Oseen tensor e.g. 2.12 by considering two opposite forces $\mathbf{f}_0 = \mathbf{f}_0\hat{\mathbf{e}}$ of equal magnitude at $\mathbf{r} = \mathbf{r}_0 \pm \mathbf{d}/2$ with $\mathbf{d} = d\hat{\mathbf{e}}$.

$$\mathbf{v}_d(\mathbf{r}) = \frac{P}{8\pi\eta r^3}\left(-1 + 3\frac{(\mathbf{r}\cdot\hat{\mathbf{e}})^2}{r^2}\right) \tag{2.22}$$

where $P = f_0 d$ is the dipole strength. Notice that the flow field of a force dipole decays as $1/r^2$ from the center of the dipole, faster than that of a force monopole.

The flow field of a hydrodynamic dipole in front of a surface can be obtained by the image method known from electrostatics [67]. Considering a planar wall with slip boundary conditions the flow field is then given by

$$\mathbf{v}_w(\mathbf{r} - \mathbf{r}_0) = \mathbf{v}_d(\mathbf{r} - \mathbf{r}_0; \hat{\mathbf{e}}) + \mathbf{v}_d(\mathbf{r} - \mathbf{r}_0; \hat{\mathbf{e}}') \tag{2.23}$$

for a wall at $z = 0$, with $\mathbf{r}_0 = (x_0, y_0, z_0)$, $\mathbf{r}_1 = (x_0, y_0, -z_0)$. There is a force on

the dipole near the surface, which is determined by the hydrodynamic interactions between the dipole and its image (Fig. 2.10).

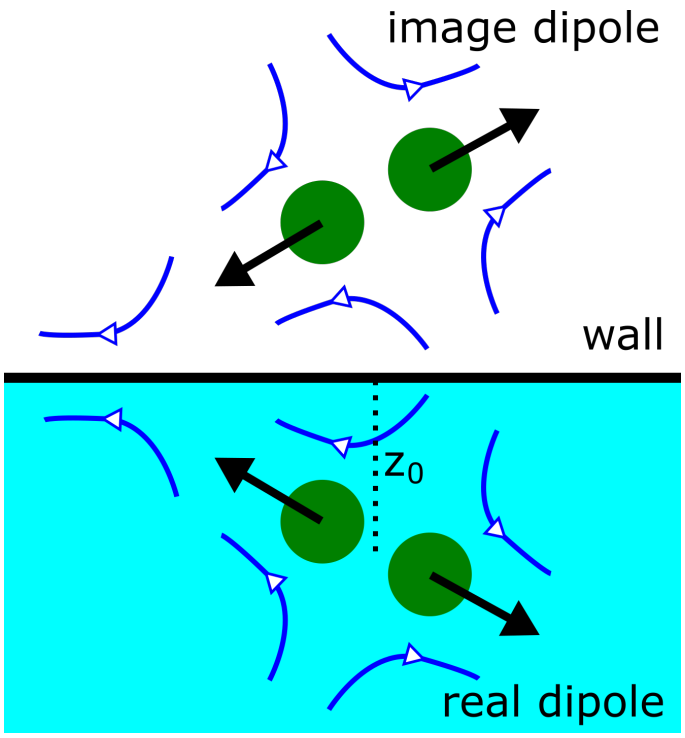


**Figure 2.10: A sketch of the flow field around a pusher near a wall.** The arrows indicate the flow directions.

It is given by the z-component of the flow field of the image at the location of the real dipole.

$$v_{w,z}(z_0) = -\frac{P}{32\pi\eta z_0^2}[1 - 3(\hat{\mathbf{e}} \cdot \hat{\mathbf{e}}_z)^2] \tag{2.24}$$

This result shows that the hydrodynamic force is attractive to the wall.

### 2.3.2 Squirmer model

The model was first introduced by James Lighthill [68] and used to study the dynamics of Paramecium, which is a unicellular organism and swim by stroking cilia [14]. Today the model is generally used to characterize artificial microswimmers, like Janus particles.

In the model, it is assumed that the flow field around a microswimmer can be described by Stokes flow (Eqn. 2.9), the assumed microswimmer is spherical and the surface of the microswimmer move purely tangentially and the flows are axisymmetric. With these assumptions, the microswimmer is also called squirmer and the tangential surface velocity $v_s$ is given by:

$$v_s = \sum_{n=1}^{\infty} \frac{2}{n(n+1)} B_n \left( \frac{\mathbf{e} * \mathbf{r}}{r} \frac{\mathbf{r}}{r} - e \right) P_n(\mathbf{e} * \mathbf{r}/r) \tag{2.25}$$

where $\mathbf{e}$ is the orientation vector of the squirmer, $B_n$ are coefficients, $P_n$ are Legendre polynomials, $\mathbf{r}$ is the position vector and r=$|\mathbf{r}|$.

Considering far field, r >> R (where R is the radius of the squirmer), the terms with n $\geq$ 3 can be neglected. The squirmer parameter is defined as: $\beta = B_2/|B_1|$. When $\beta = 0$, it means the flow on the surface of the squirmer is homogeneously distributed from the leading end to the rearing end and the squirmer is a neutral squirmer. When $\beta > 0$, it means the flow on the rearing part of the squirmer is stronger than the leading end and the squirmer is a pusher. With $\beta < 0$ in contrast, the flow on the leading end of the squirmer is stronger than the rearing end and the squirmer is a puller. Fig. 2.11 displays the numerically computed flow fields around different squirmer types.

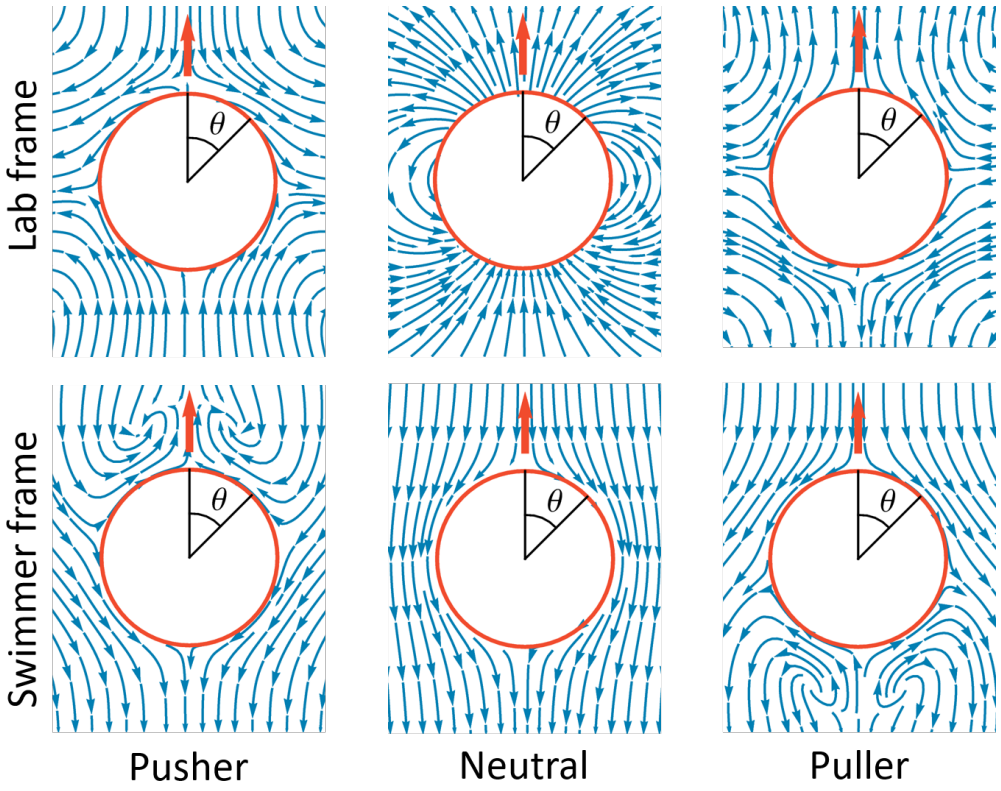


**Figure 2.11: Flow field around pusher, neutral and puller squirmers from simulation.** Top row: lab frame. Bottom row: swimmer frame.

## 2.4 Fabrication of microfluidic chamber

In the experiment, droplets swim in a reservoir and are observed under an optical microscope. Two types of reservoirs are used in the experiment. The first type is

made of glass slides, which are cut into squares with the size of about (2.5 * 2.5) $cm^2$ and coated with octadecyl-trichlorosilane (OTS) [69]. OTS coated glass slides were stagged with a cover slide in the middle as a spacer (thickness, 150 $\mu$m) and glued together from three sides using epoxy glue (Fig. 2.12). After the glue is cured, the cover slide spacer is removed. The open side of the reservoir will be used to fill the device with the continuous phase and inject droplets.

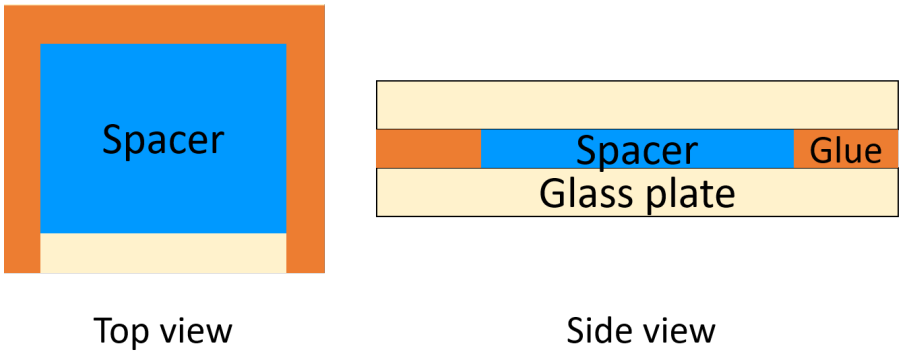


**Figure 2.12: A sketch of reservoir type 1.**

The hydrophobic OTS coating avoids ethanol/water droplet attaching to the surface. The height of the reservoir is slightly larger than the diameter of the droplets, so the droplets move in a quasi-2D geometry. The area of the reservoir is sufficiently large to neglect the in-plane boundaries to the reservoir during the movement of the droplets.

The advantage of this (first) type of reservoir (OTS coating) is that, the reservoir can be reused after cleaning by sonication in ethanol. But there are also two limitations. First, in cases of very high ethanol concentration in the droplets and in cases of large number density of droplets in the reservoir (collective behavior), the OTS coating does not avoid droplet attachment. In addition, it is difficult to fabricate structures on a glass plate. Because of these disadvantages of the first type of reservoir, it is later replaced by the second type of reservoir with better features and allows using droplets with even very high ethanol concentration and large number density.

The second type of reservoir consists of a glass bottom and the top part is Polydimethylsiloxan (PDMS, as the cover, Sylgard 184 Dow Corning). The mold for PDMS is made of PMMA by computerized numerical control (CNC) micro-machining. To generate pillar structures, there are some holes are drilled in the mold (Fig. 2.14). The round shaped reservoir is 12 mm in diameter and 150, 300, 450, 600, 750, 1500 $\mu$m in height. The round-shaped holes are 600 $\mu$m in radius and the square-shaped holes are 600 $\mu$m in side length (Fig. 2.13). The holes have the same height as the reservoir.

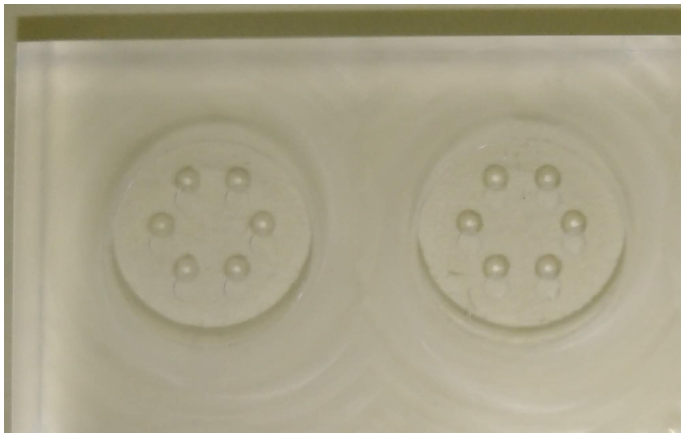

**Figure 2.13: A photo of a PMMA mold with round holes** (300 $\mu m$ in height). The reservoir is 12 mm and the holes are 600 $\mu$m in diameter.

PDMS (Sylgard 184) and curing agent are thoroughly mixed with weight ratio 10:1. The PDMS mixture is put into a vacuum chamber for about 20 minutes to remove bubbles that were generated during mixing. Then the PDMS mixture is poured onto the mold and put on a hot plate at 70 °C (Fig. 2.14a). Both of glass plates and PDMS covers are coated with Poly[4,5-difluoro-2,2-bis(trifluoromethyl)-1,3-dioxole-co-tetrafluoroethylene] (AF2400, Sigma-Aldrich) by dip coating. To close up the chamber, the PDMS cover is simply put on top of the AF2400 coated glass plate gently, without any bonding or glue (Fig. 2.14b). A small opening ($\sim$ 1 mm) is cut from one side of the PDMS cover for the injection of continuous phase and droplets.

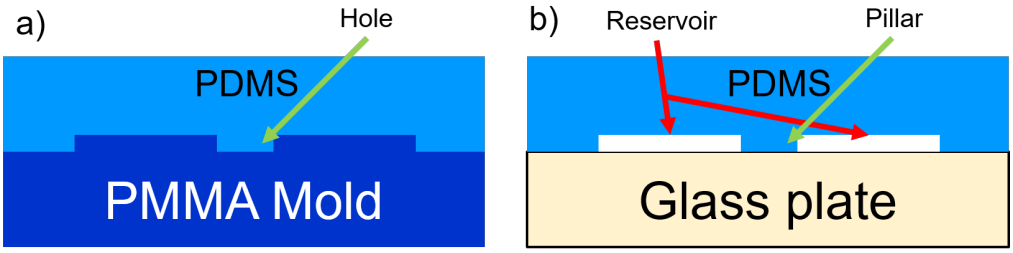


**Figure 2.14: An illustration of a PDMS-glass reservoir fabrication.**

## 2.5 Droplet production

Cross-flow [70] and co-flow [71] are two types of microfluidic devices producing droplets. In a cross-flow device, the finger of dispersed phase is pushed into the channel with continuous phase and then sheared off by the cross-direction flow (Fig. 2.15a). In a co-flow device, not considering jetting with high flow rate of dispersed phase, drops detach from the inlet when the stream shear stress exceeds interfacial tension (Fig. 2.15b).

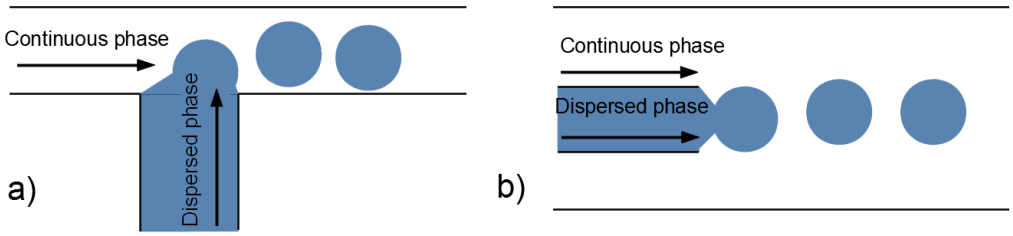


**Figure 2.15: A sketch of droplets production by a) cross-flow and b) co-flow**.

The advantages of generating droplets on microfluidic devices are that, the production of droplets is fast and the size of the thus produced droplets is uniform. But these techniques could not be used in our system because of the wetting of ethanol/water droplets on the wall of the channel. Although we used AF2400 coated reservoir to avoid attachment of droplets, it is difficult to deploy such a coating on the surface of a closed microfluidic channel. So we used two customized methods producing droplets that can be considered as variants of cross-flow and co-flow.

In the first method, small emulsion droplets are generated by a very thin glass capillary (10 $\mu$m in inner diameter). One end of the glass capillary is connected via tubing to a syringe that is filled with ethanol/water mixture. The other end of the capillary is injected into the reservoir filled with oil and surfactant (squalane and monoolein, Fig. 2.16). The syringe is pushed by hand very slowly and the capillary is moved from side to side perpendicular to the capillary. This leads to a relative shear flow on the dispersed phase and droplets are produced.

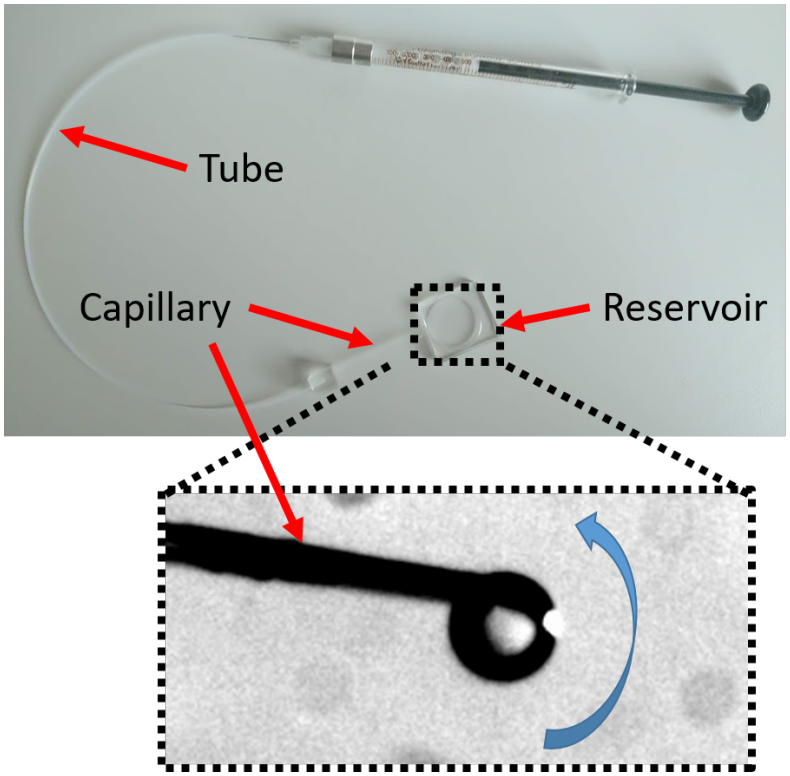


**Figure 2.16: A photo of a capillary connected to a syringe producing droplets.**

This method is inspired by the cross-flow method and the advantage of this method is that, the production of droplets is controlled simply by hand, so that droplets with a very small number density can be produced to study single droplet movement, without interaction with each other. The disadvantage of this method is that, it is difficult to produced a large number of monodispersed droplets to explore the collective behavior. So we used the concept of co-flow in a Teflon tube to produce large quantities of droplets.

In the second method, a glass capillary is injected into the middle of a Teflon tube (300 $\mu$m inner diameter) and connected to a syringe containing ethanol/water. The Teflon tube is connected to a syringe containing squalane/monoolein. The two syringes are controlled by a syringe pump. During the experiment, ethanol/water mixture is injected through the glass capillary into the Teflon tube with sqalane/monoolein mixture co-flowing in the tubing (Fig. 2.17). When certain amount of ethanol/water mixture is pushed out through the tip of the glass capillary, it will be pinched off and form droplets. The other end of the tube is connected to a reservoir and droplets are guided directly into it.

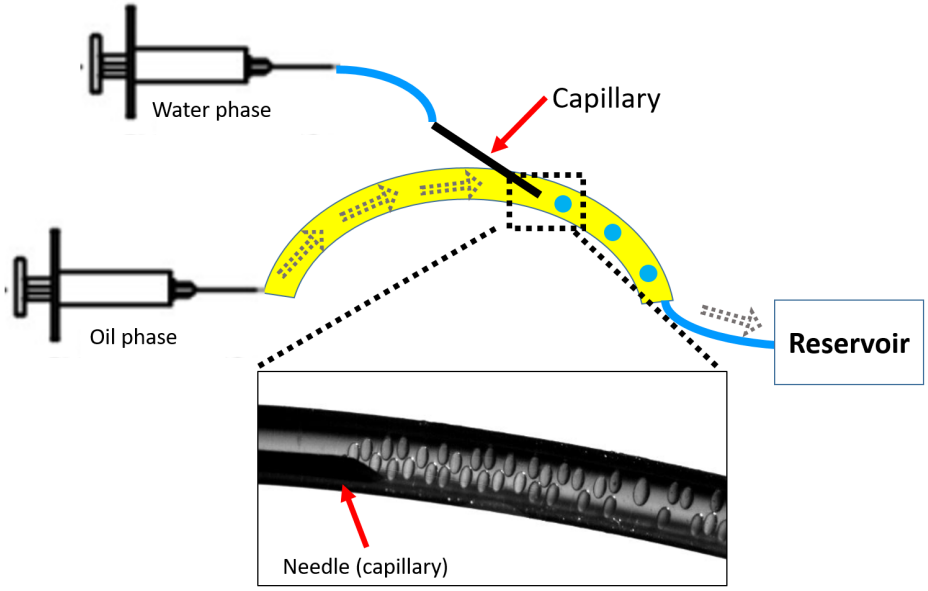


**Figure 2.17: A sketch and a snap shot of drop production for collective motion.** (The elongated droplets on the photo is because of lens effect of the round Teflon rube.)

The motion of the self-propelled droplets are observed under a microscope (Leica z16 apo) and recorded by a camera (PCO HS1200, Fig. 2.18). The typical magnifications are 2 times to track the movement of the droplets and 20 times to observe the inner-structure of the droplet. The typical frame rate is 1 frame per second.

**Figure 2.18: A photo of the optical microscope setup.**

## 2.6 Droplet tracking

Two commercial software packages were used to track droplets: Image-Pro Plus [72] and Matlab. Image-Pro Plus first binarizes an image and then detects dark or bright objects. The threshold of binary is usually set slightly darker than the background (peak on the histogram), so that as many as possible droplets (dark) can be detected and as few as possible false objects are detected (Fig. 2.19).

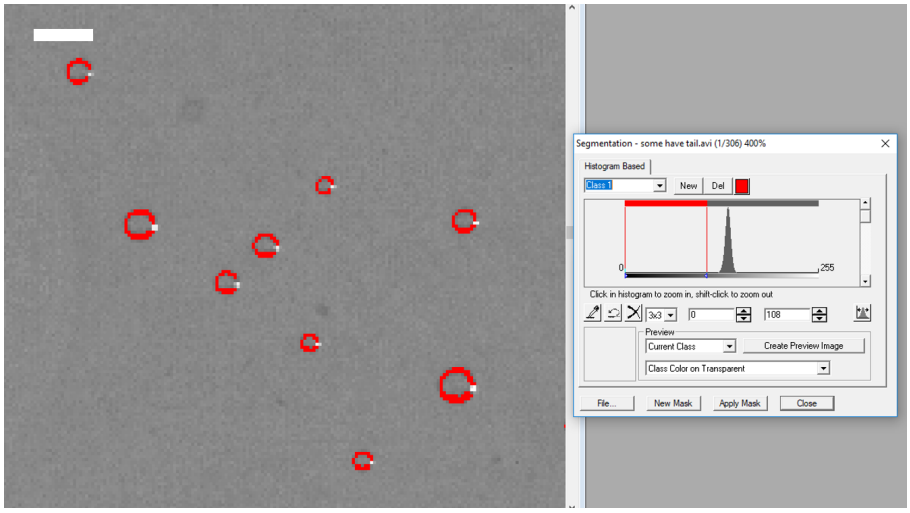


**Figure 2.19: The user interface of Image-Pro Plus for binary threshold setting.** The binary threshold is set slightly darker than the peak to detect dark droplets. The scale bar is 100 $\mu$m.

There are options that can fill up holes on objects and combine several objects next to each other to one (Fig. 2.20). These options avoid detecting only the (dark) border of the droplets or splitting one droplet into several objects. The areas of the detected objects are used to calculate the radius of the droplets.

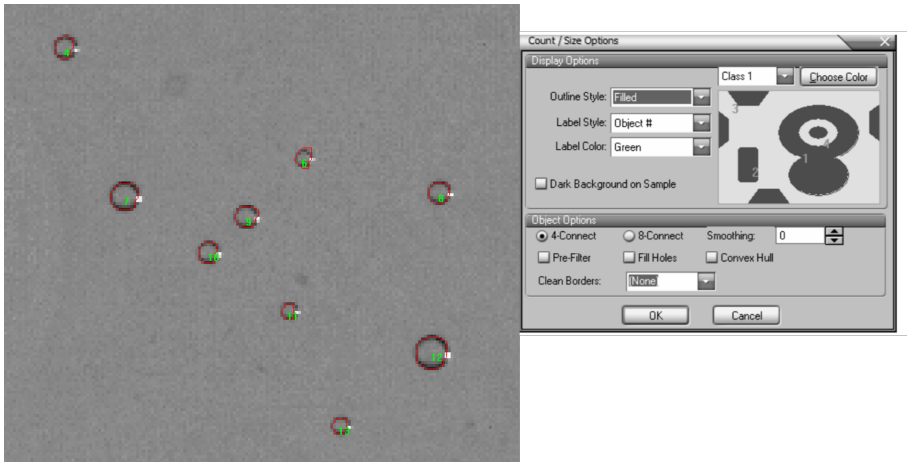


**Figure 2.20: The user interface of Image-Pro Plus for detecting objects.** The detected objects are marked by red contours and labeled by green numbers.

The 'Tracking' toolbox compares objects on two consecutive frames. The 'two' objects that are roughly on the same position of the two frames are considered as one moving object. By comparing each two consecutive frames for the whole image sequence, the moving objects are detected. The coordinates of these moving objects on each frame become the trajectories (Fig. 2.21).

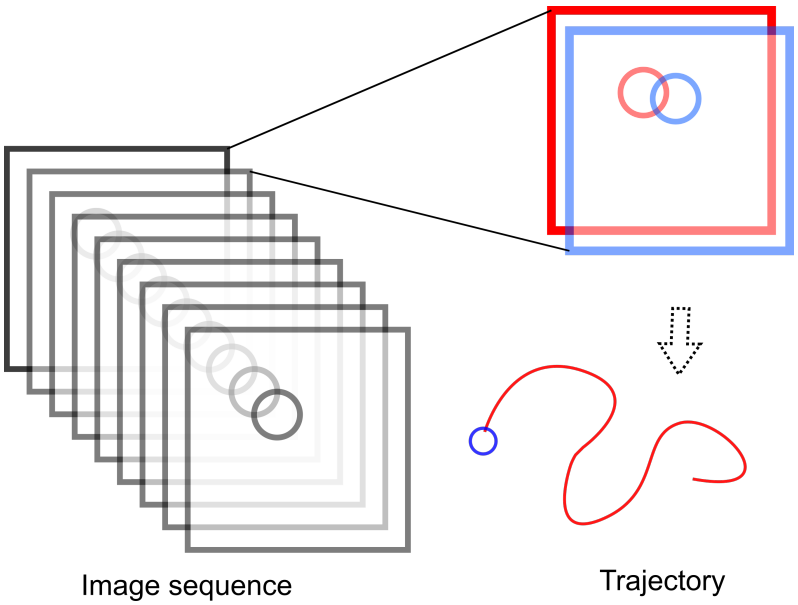


**Figure 2.21: An illustration of the 'tracking' toolbox principle.**

In Matlab, circle-shaped objects in the image are detected by the function 'imfindcircles' [73]. Pixels on the high gradient areas are designated as candidate pixels (edge pixel, Fig. 2.23a). A circle is draw around the center of each edge pixel with a radius, which is in the user defined range. Each point on the circle is a vote pixel. If edge pixels belong to a circle, the vote pixels tend to accumulate at the center of the circle (Fig. 2.23b). Therefore, the centers of circles are estimated by the peaks of vote pixels and the radius, which is used to draw the vote pixel circle, is the radius of the detected object.

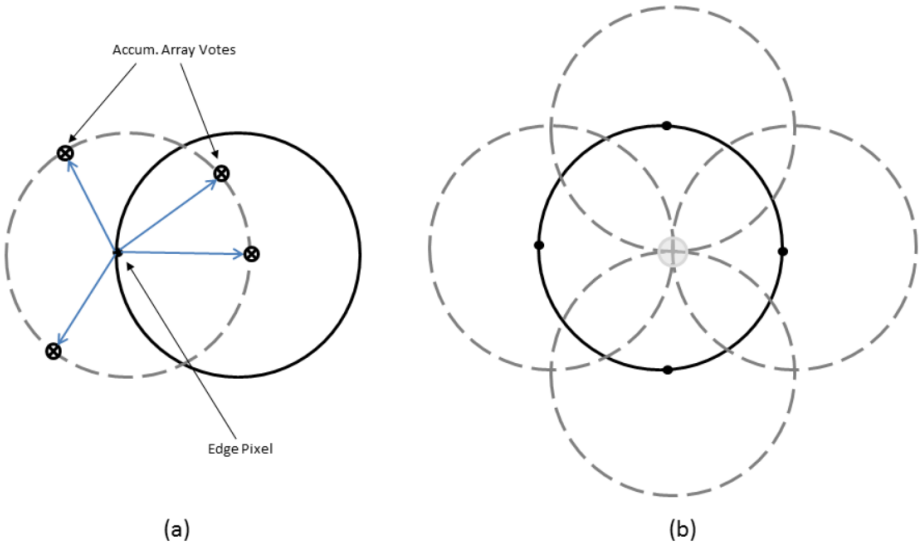


**Figure 2.22: Illustration of the algorithm of the function 'imfindcircle'.**

Besides the radius range, the optional parameters 'Sensitivity' and 'EdgeThreshold' can be used to change the threshold of circle detection. With higher 'Sensitivity'

and lower 'EdgeThreshold' values, more obscured circle objects can be detected. But meanwhile, it increases the risk of false detection.

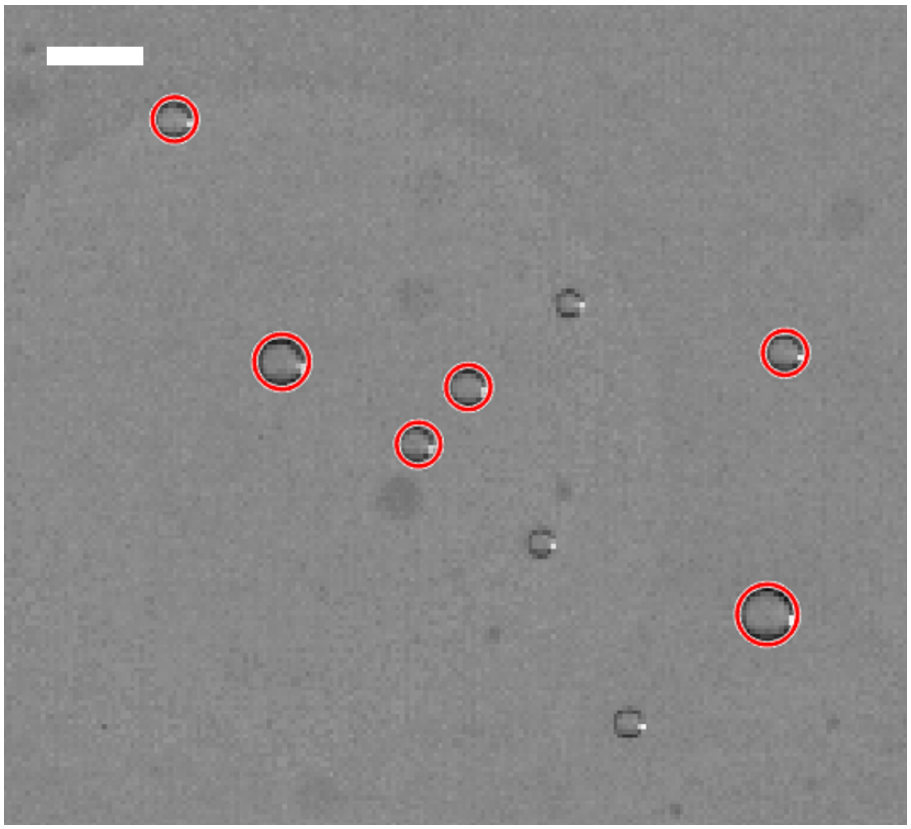

**Figure 2.23: Examples of droplets/circles detection by 'imfindcircle' on Matlab.**

As next step, detected objects (the center of the circle) from each two consecutive frames are assigned as the same object on the two frames with the function 'detectionToTrackAssignment' [74]. In this function, a 'cost' matrix is calculated, which is a matrix containing the distance between each object in the first frame and each object in the second frame. By inserting the cost matrix to the function 'detectionToTrackAssignment', 'assignments', 'unassignedTracks' and 'unassignedDetections' come out. 'Assignments' describes how objects are assigned to a track between two frames. Unassigned tracks will be closed up after several frames. Unassigned detections will be the start of a new track. By the end droplets detection, the unit of the data are converted to real spacial and temporal units using the pixel resolution and the frame rate.

The advantage of Image-Pro Plus is easy to learn and to use. Besides, it can reliably detect droplets with small radius ($< 5$ pixels). Matlab, which detect circle-shaped objects, gives more precise circle center coordinates and radius estimation (Fig. 2.23). In our case, Matlab are mostly used except when the droplets are too small.

## 2.7 $\mu$PIV and fluorescent imaging

Micro-particle imaging velocimetry ($\mu$PIV) is an optical method to visualize flow field and quantify direction and velocity of the flow. Tracer particles, which are small enough to follow the flow, are added to the continuous phase. Particles in the fluid are illuminated and become visible. The motion of the tracer particles represent the flow of the fluid being studied.

$\mu$PIV is used to measure microscopic flows. Fluorescent tracing particles used in $\mu$PIV can be excite at a shorter wavelength and emit at a longer wavelength. On an epifluorescence microscopy (Fig. 2.24), laser light goes through an excitation filter, is reflected by a dichroic mirror, goes through an objective lens and illuminates a region of interest (with particles). The emission light from the particles goes through the objective lens, the dichroic mirror and an emission filter and detected by a camera.

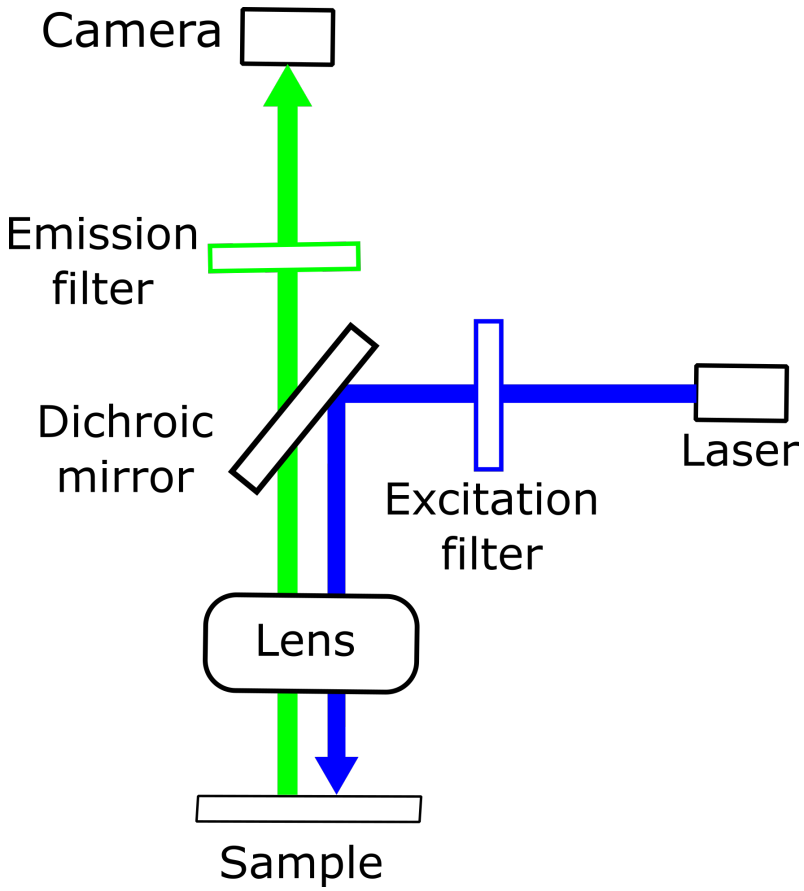


**Figure 2.24: A schematic of an epifluorescence microscope for $\mu$PIV.**

Two fluorescent images are taken by a camera with a certain interval in between. Normally the minimal interval between the two fluorescent images are limited by the frame readout time. With double frame mode, a pair fluorescent images with a very short interval (<10 ms) can be taken [75]. After taking the first frame, the image is transfered to a high-speed memory. The camera start taking the second

frame immediately. Meanwhile the first frame is read out. Then the second frame is read out (Fig. 2.25).

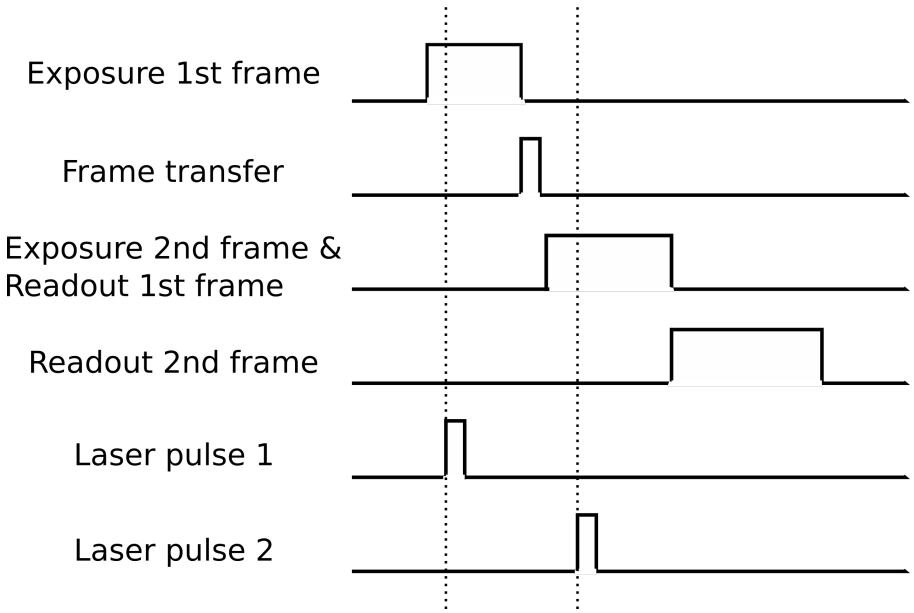


**Figure 2.25: PIV double frame mode time lines.**

In our case, two normal frames are taken with large interval (typically one second) according to the low flow rate ($\approx 10\ \mu m$). For the double frame mode, the exposure time of the second frame is longer than the first one, therefore the second frame is sensitive to the background light. In our case, this disadvantage can be eliminated.

To obtain/analyze the flow field, the two frames are split into a large numbers of interrogation windows. By calculating the cross-correlation between the corresponding interrogation windows of the two frames, a displacement vector for the correspond window can be acquired (Fig. 2.26). By choosing smaller windows, the spacial resolution of displacement vector map (flow field) is higher. But there should be at least four particles on average in each window to reliably calculate the cross-correlation between two windows.

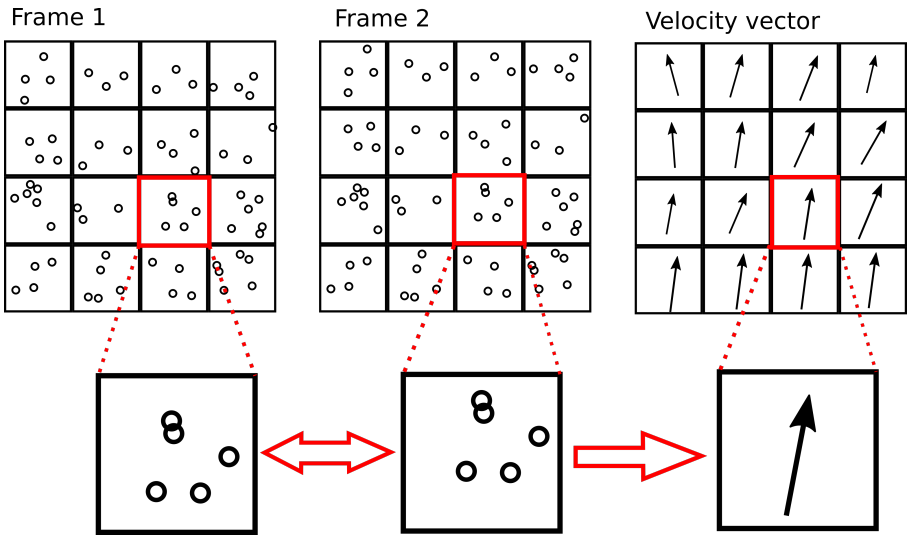


**Figure 2.26: An illustration of the concept of $\mu$PIV**

In the experiment, fluorescent beads (Fluoro-Max Red Aqueous Fluorescent Particles R0100, 1 $\mu$m in diameter) are added to the continuous phase. The number density of the beads is around $3 * 10^9$ per ml. Two frames are recorded with one second interval. The field of view is around 600 * 800 $\mu$m and it is divided to 64 * 64 interrogation windows.

The fluorescent beads are excited by a green laser (DPSSL, 532 nm) and observed under a microscope (Zeiss, Observer Z1) with 20X lens. During the measurement, the microscope is focused on the middle of the horizontal layer of the droplet. The fluorescent images are recorded by a CCD camera (Imager proX, Fig. 2.27). The data analysis is done by the Davis software.

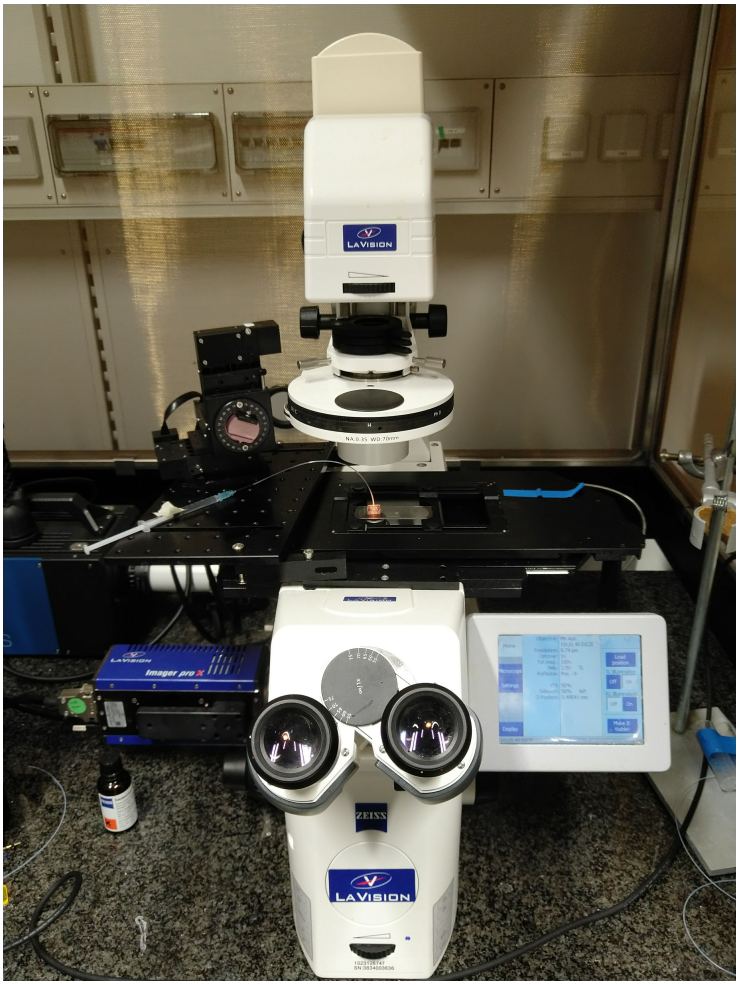


**Figure 2.27: A photo of the fluorescent microscope setup.**

To keep track of monoolein, a fluorescent lipid (1-palmitoyl-2-12-[(7-nitro-2-1,3-benzoxadiazol-4-yl)amino]dodecanoyl-sn-glycero-3-phosphocholine, NBD) which has the similar chemical affinity as monoolein is added to squalane (7 $\mu$g/ml). In this way, the fluorescent signal can indicate monoolein. In addition, monoolein (NBD) has a higher affinity to ethanol than to squalane or water, the fluorescent signal can indicate ethanol-rich phase after the demixing of ethanol and water. NBD is excited by a blue laser (DPSSL, 473 nm), observed and recorded by the same microscope and camera as in $\mu$PIV. The intensity of the both lasers are not allowed to change by the software. Instead, the excitation time can be set to adjust the fluorescent signal. This excitation time is set to 1000 $\mu$s if it is not extra mentioned.

## 2.8 Ethanol/water/monoolein phase diagram

Although the phase separation between water and ethanol is contradicted to the instinct, this can be simply demonstrated in bulk. By adding monoolein, ethanol/water mixture spontaneously separate to two phases (Fig. 2.28).

**Figure 2.28: Demixing of ethanol and water in bulk.** 8 mg monoolein is added to 1 ml 40% ethanol/water mixture (volume percent, for all ethanol/water mixture if not specified).

In [76] and [77], different phases of ternary monoolein/ethanol/water mixtures are studied. A sketch the of ternary phase diagram of water, ethanol and monoolein is redrawn according to [76]. The curve on the ternary phase diagram is the coexist line. Under the coexist line (in the darker area), ethanol and water become two phases (Fig. 2.29).

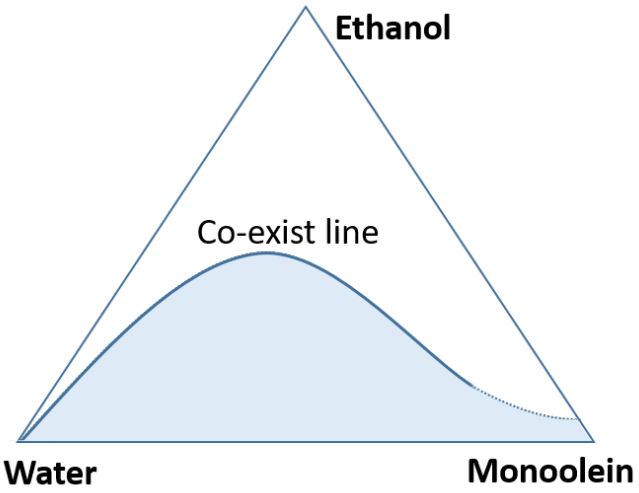


**Figure 2.29: A sketch of the ternary phase diagram of water, ethanol and monoolein.**

## 2.9 Cargo delivery preparation

In chapter 5, we demonstrate DNA/RNA precipitation and transportation conducted by self-propelled droplets. DNA (Deoxyribonucleic acid from herring sperm),

RNA(Ribonucleic acid from torula yeast Type *iv*), fluorescent dye Hoechst 33342 (2'-(4-Ethoxyphenyl)-6-(4-methyl-1-piperazinyl)-1H,3'H-2,5'-bibenzimidazole) and Acridine Orange and salt (Lithium Chloride and Sodium Acetate) are purchased from Sigma-Aldrich.

Hoechst 33342 is a specific fluorescent DNA stain that prefers to bind with adenine and thymine rich regions and form compounds (Fig. 2.30). The binding between DNA and Hoechst 33342 changes the excitation maximum from 340 nm to 355 nm and enhances the fluorescence considerably [78] [79].

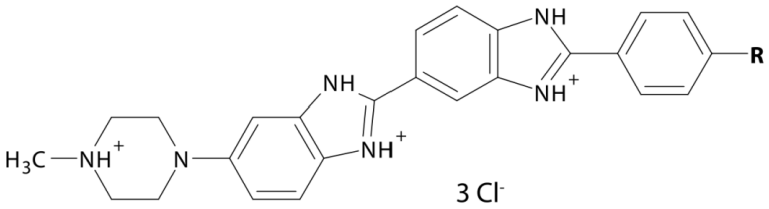


**Figure 2.30: Chemical structure of Hoechst 33342.**

Before the experiment, DNA/RNA, Hoechst 33342 and salt (if required in the experiment) are added to the droplet phase and thoroughly mixed by stirring. Droplets are produced the same way as presented above (first method) and illuminated by a UV lamp (wave length, 366 nm).

The solubility of DNA or RNA can be changed by adding salt. The backbone of DNA and RNA is negatively charged due to the phosphate groups. Thus DNA and RNA are soluble in water. With salt, positively charged ions neutralize DNA or RNA molecule and decrease the solubility of DNA or RNA in water [79] [80] (Fig. 2.31).

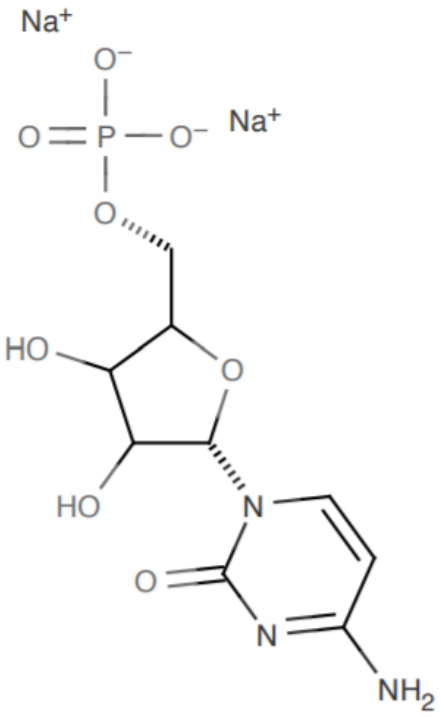


**Figure 2.31: Chemical structure of nucleotide neutralized by sodium ions.**

Another fluorescent dye, Acridine Orange (AO, Fig. 2.32) has different interactions with DNA and RNA. When AO is bounded with DNA, it is fluorescent with an excitation maximum at 502 nm and an emission maximum at 525 nm. When it is bounded with RNA, the excitation maximum shifts to 460 nm and the emission maximum shifts to 650 nm [81]. Samples are prepared the same way as for Hoechst 33342, with 10 $\mu$g/ml AO in the droplet.

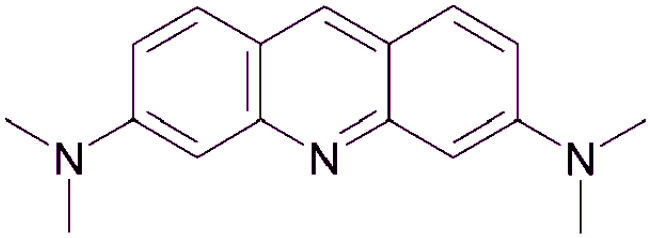


**Figure 2.32: Chemical structure of Acridine Orange.**

## 2.10 Chemotaxis preparation

In chapter 6, we demonstrate the chemotaxis effect between droplets in ethanol-saturated squalane. The preparation of ethanol-saturated squalane is described as following: Ethanol and squalane are filled into a vial and mixed thoroughly by

shaking. The solution becomes obscure with emulsion (Fig. 2.33a). Let it stand for at least three days, ethanol and squalane separate to two phases (squalane with higher density is at the bottom, Fig. 2.33b). We consider the squalane is saturated with ethanol. Squalane is taken out with a pipette carefully to avoid taking extra ethanol with it. This ethanol-saturated squalane can be mixed with pure squalane with a certain ratio to get under-saturated squalane with well defined saturation factor. For example, 60%-saturated squalane is made of 60% saturated squalane with 40% pure squalane. Then monoolein is added to ethanol-(under)saturated squalane and mixed by magnetic stirrer.

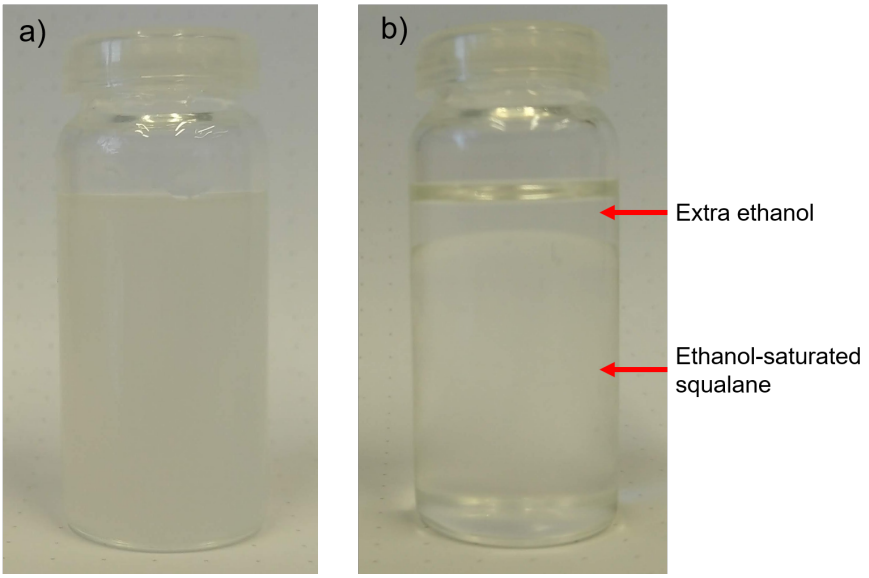


**Figure 2.33: Two photos of squalane/ethanol mixture (a) right after shaking and b) stand for three days).**

# Chapter 3

# General behavior of self-propelling droplets

The behavior of the droplet is quite complex and to avoid too many repetitions we explain here the basic droplet behavior to make the subsequent sub-chapters explaining the finding in detail easier to understand. Once ethanol/water droplets are injected into the continuous phase (squalane/monoolein), droplets start to propel randomly (Fig. 3.1a). During the propulsion, droplets release ethanol into the continuous phase and take up monoolein from the continuous phase. After a certain time, the monoolein concentration in the droplet reaches a threshold and the droplet spontaneously separate to water-rich phase and ethanol-rich phase (Fig. 3.1b). With specific ethanol concentration, a Janus droplet is formed and continues to propel (Fig. 3.1c). At the end of the propulsion, the water-rich phase and the ethanol-rich phase pinch off and the droplet gradually stops (Fig. 3.1d). The duration of the evolution stages can be controlled by droplet size, ethanol concentration and monoolein concentration. Droplets have a different hydrodynamic flow field and a different velocity profile during each evolution stage. In the following it will be explained in detail how the knowledge of the propulsion behavior was obtained and the driving mechanisms behind.

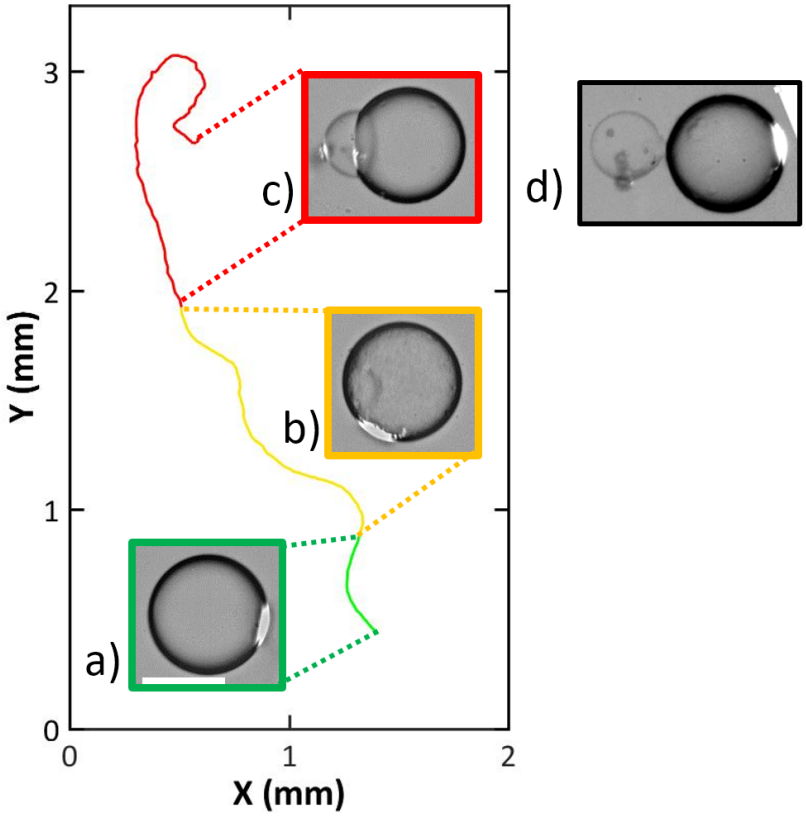


**Figure 3.1: A typical trajectory of a 50% ethanol droplet with three snapshots of a droplet (50%) before (green), during (yellow) and after the phase separation (red).** The trajectory and the three snapshots are not from the same data set. The droplet for the trajectory is about 50 $\mu$m in radius. The scale bar is 100 $\mu$m.

## 3.1 Evolution stages

For the intermediate ethanol concentration (40-60%), the droplets start to propel right after their production (stage 1, Fig. 3.2a). After 20-300 second depending on the ethanol concentration, small droplets ($\sim$1-3 $\mu$m in diameter) appear in the bulk of the self-propelled droplet (stage 2, Fig. 3.2b). Due to the internal flow field, these small droplets are transferred to the rear end of the self-propelled droplet and merge with each other, forming a new single droplet. This stage 2 lasts for about 1-2 minutes. This new-formed droplet is gradually pushed out of the self-propelled droplet, trails behind and a Janus droplet is formed (stage 3, Fig. 3.2c). This Janus droplet continues to move for about 5 minutes until the Janus droplet separate (Fig. 3.2d). After separation, the trailing droplet typically spreads on the bottom of the reservoir and the leading droplet stops gradually within a few droplet radii.

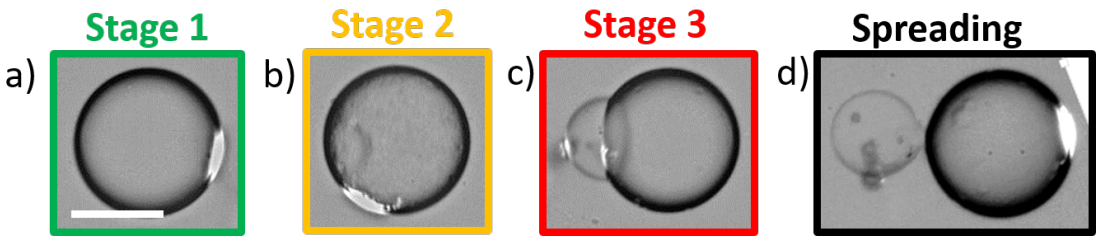


**Figure 3.2: A 50 % droplet in a) stage 1, b) stage 2, c) stage 3 and d) separation (spreading).** The scale bar is 100 $\mu$m.

For the low ethanol concentration (30%), the de-mixing starts almost immediately after the droplet production. The self-propulsion can effectively be observed only in stage 3 for about 5 minutes. For the ethanol concentration below 30%, de-mixing or self-propelled motion is not occurring reliably.

For the high ethanol concentration (70-80%), the duration of stage 1 (Fig. 3.3a) is extended to 7-15 minutes until de-mixing starts (stage 2, Fig. 3.3a). In contrast to intermediate and low ethanol concentrations, the small droplets, which emerge inside the self-propelled droplet, separate from the large droplet while the large droplet spreads on the reservoir bottom and stop moving (Fig. 3.3c). For the ethanol concentration higher than 80%, droplets spread easily on the reservoir bottom and are hard to reliably observed.

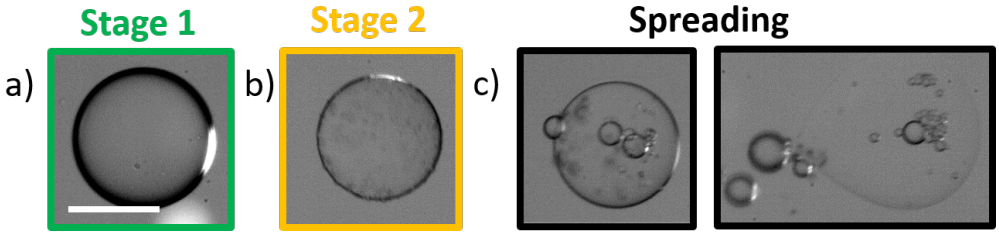


**Figure 3.3: A 70 % droplet in a) stage 1, b) stage 2 and c) spreading.** The scale bar is 100 $\mu$m.

### 3.1.1 Velocity fingerprint in three stages

The velocity character of a droplet changes consistently with the stage transitions. For intermediate ethanol concentration (Fig. 3.4b), the velocity stays constant with certain fluctuation and sinks to a lower point short before the end of stage 1. In stage 2, the velocity increases linearly as a function of time until reaching a maximum. In stage 3, the velocity decreases about exponentially as a function of time.

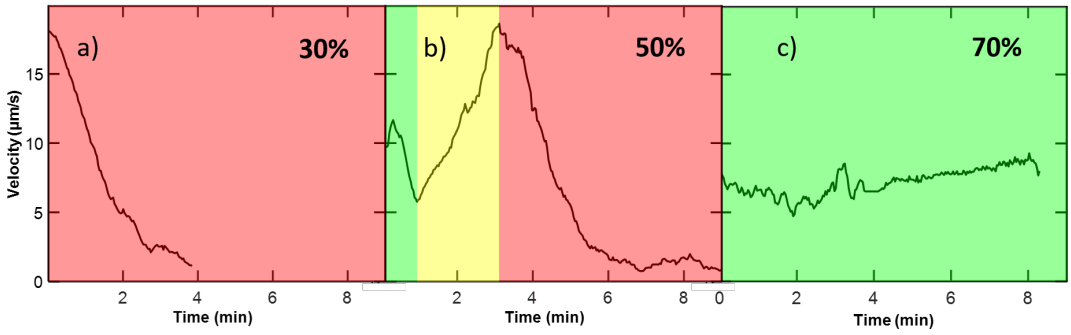


**Figure 3.4: Velocity-time diagrams of a) a 30%, b) a 50% and c) a 70% ethanol droplet.**

For the low ethanol concentration, the droplets can be only observed in stage 3 (Fig. 3.4a). The velocity decreases about exponentially as a function of time, which is similar to the intermediate ethanol droplets.

For the high ethanol concentration, the velocity stays constant with certain fluctuation (Fig. 3.4c). There is no significant difference between stage 1 and stage 2.

### 3.1.2 Flow field measured by $\mu$PIV in three stages

This evolving nature reflected by phase separation and moving velocity is also reflected in different flow regimes. The flow field around the droplet (in the middle of the horizontal layer of the droplet) is measured by $\mu$PIV and then compared with the flow field of model squirmers (pusher, puller and neutral squirmer).

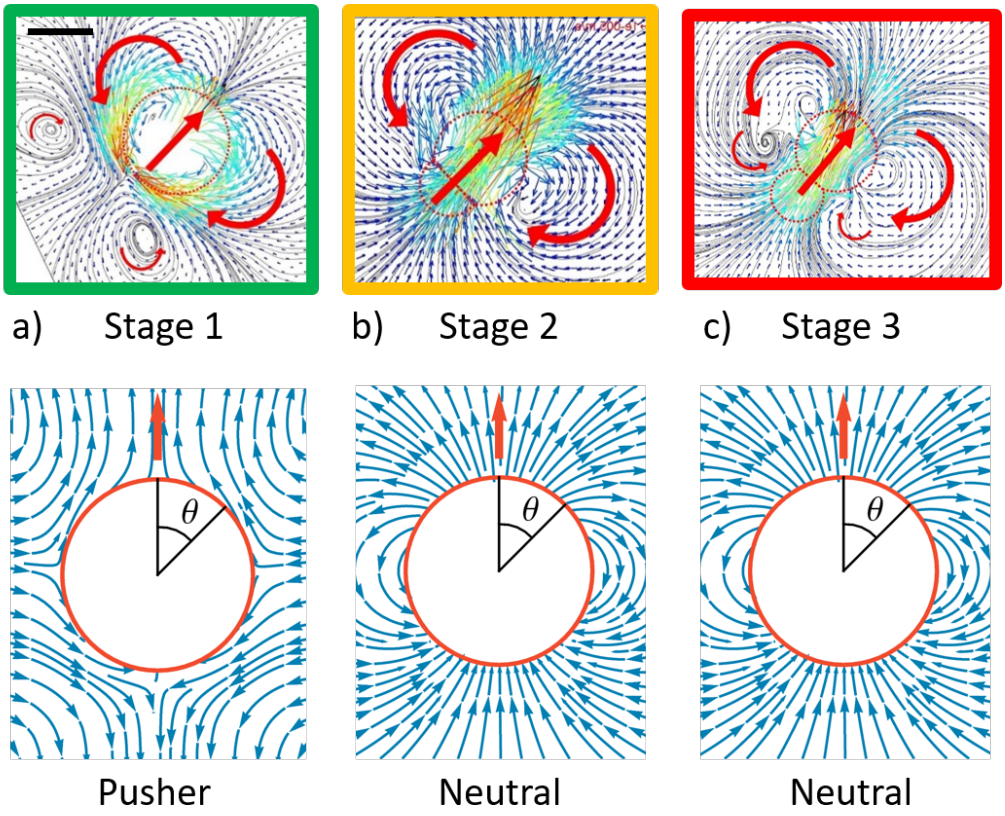


**Figure 3.5: Flow fields measured by $\mu$PIV in comparison with simulations.** In stage 1, the flow field around the droplet (with four vortexes) indicates that the droplet is a pusher. In stage 2, the droplet is a neutral squirmer. In stage 3, the droplet is a chain of neutral squirmer. The scale bar is 100 $\mu$m.

In stage 1, there are four vortexes around the droplet. The two bigger ones are beside the droplet and the two smaller ones at the rearing end have different directions to the bigger ones (Fig. 3.5a). The droplet is characterized as a weak pusher. The symmetry of the flow field would lead to a long-range hydrodynamic interaction and can be attracted to an obstacle as introduced in the chapter 3.

In stage 2, there are only two vortexes beside the droplet (Fig. 3.5b). It is characterized as a neutral squirmer, which will not be attracted to an obstacle any more.

In stage 3, there are four vortexes around the droplet. Different from stage 1, the two vortex beside the main droplet and the two behind have the same direction (Fig. 3.5c). In this stage, it is characterized as a dimer of neutral squirmer.

## 3.2 Phase separation in the droplet

The phase separation in the droplet, which is made of two fully miscible liquids (ethanol and water), is contradicted to instinct. But this can be explained by the

ethanol/water/monoolein phase diagram. With low ethanol concentration and certain monoolein concentration (under the co-exist line), the ethanol/water/monoolein mixture will have a spontaneous phase separation (Fig. 3.6). In fact this is what happened in the droplet during the movement.

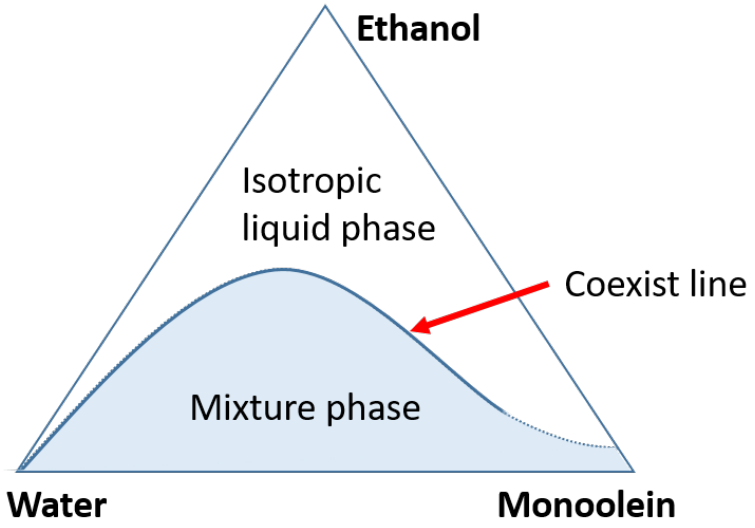


**Figure 3.6: A sketch of ethanol/water/monoolein phase diagram based on [76].**

Droplets loose volume during the movement in stage 1. This phenomenon is not so obvious for droplets with medium ethanol concentration with the short time in stage 1, but more remarkable for droplets with high initial ethanol concentration. A 80% ethanol droplet can e.g. loose up to 40% of the volume before phase separation (Fig. 3.7). Because the solubility of water in squalane is very limited, we assume that all the volume loose is caused by the ethanol solubilization in squalane. Pure water droplet does not loose volume (or move).

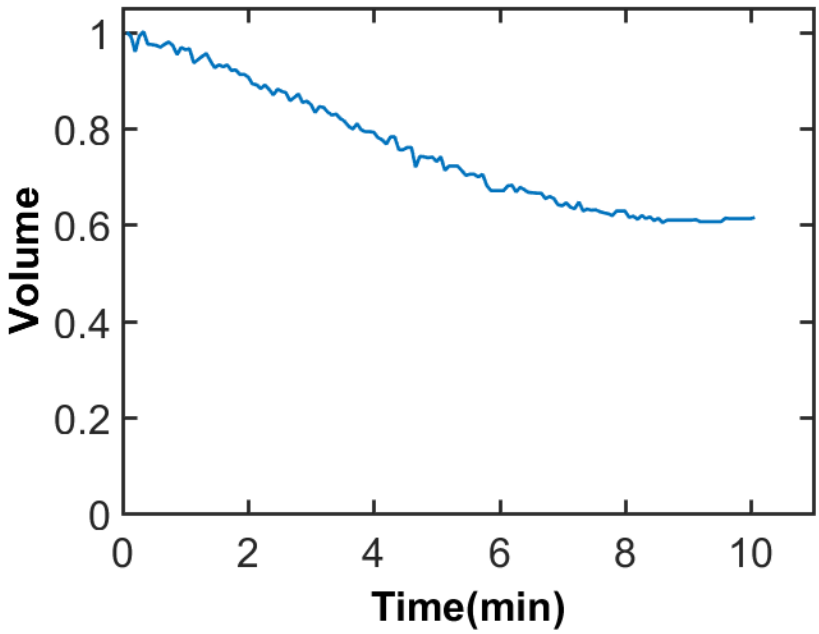


**Figure 3.7: One droplet with 80% ethanol loose 40% volume before phase separation.**

The release of ethanol is still not sufficient to explain a phase separation. Thus monoolein is traced by using NBD, which has the similar chemical affinity as monoolein. In stage 1, the droplet becomes bright by absorbing NBD/monoolein from squalane. A dark trace is left behind the droplet, which is the NBD/monoolein depleted area after the droplet passed by (Fig. 3.8). This dark trace is visible for all different ethanol concentration droplets.

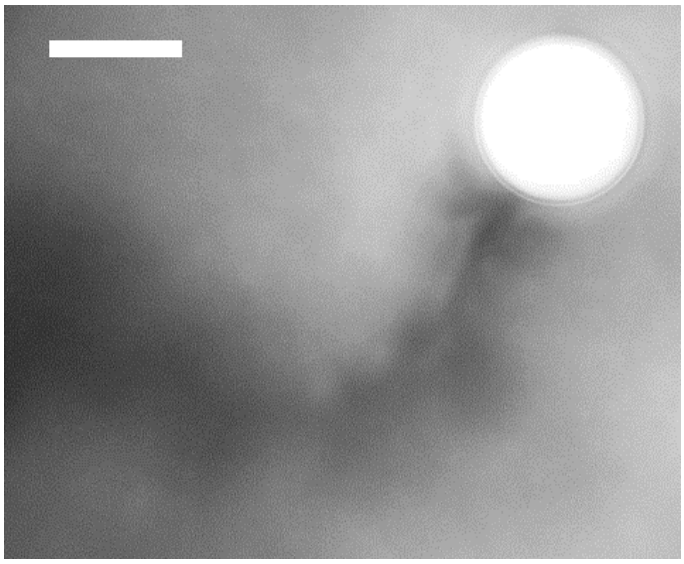

**Figure 3.8: A 60% ethanol droplet becomes bright right after it is produced (in ∼1 minute) and leaves a dark trace behind.** The scale bar is 100 $\mu$m.

Knowing that the composition of the droplet phase is changed by a release of ethanol and an uptake of monoolein, we can use the phase diagram to understand the phase separation. By loosing ethanol and absorbing monoolein, the point will move roughly along the green lines on the sketch (away from ethanol and closer to monoolein) until reaching the coexist line when phase separation starts (Fig. 3.9).

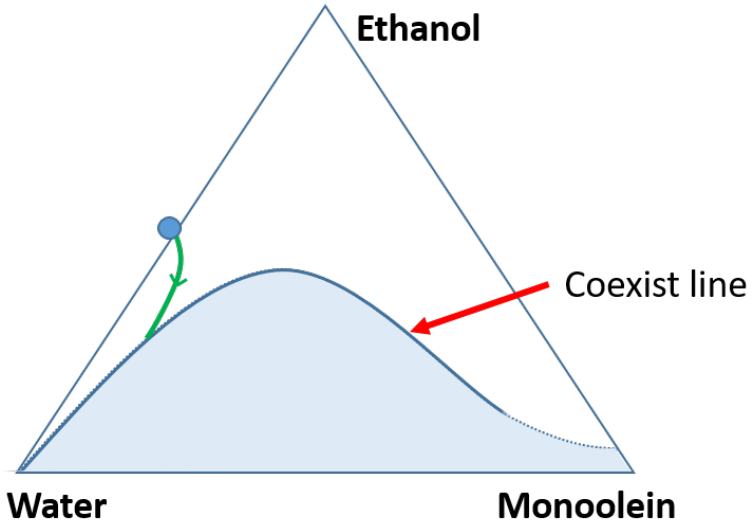


**Figure 3.9: A sketch of ternary phase diagram of water, ethanol and monoolein based on [76].**

Since the phase separation is triggered by monoolein uptake and ethanol release, the duration time before phase separation (duration time in stage 1, $t_1$) is dependent on the monoolein concentration in squalane and the ethanol concentration in the droplet.

By increasing monoolein concentration in squalane, it takes shorter time for the droplet to absorb enough monoolein to trigger phase separation, so $t_1$ becomes shorter (Fig. 3.10). The moving velocity increases by increasing monoolein concentration until reaching a plateau at 18 mM. Due to the opposite trend of $t_1$ and average velocity, the cruising range in stage 1 is hardly affected by the monoolein concentration. With lower monoolein concentration ($< 6$ mM), droplets become unstable and typically stick to the bottom of the reservoir before phase separation.

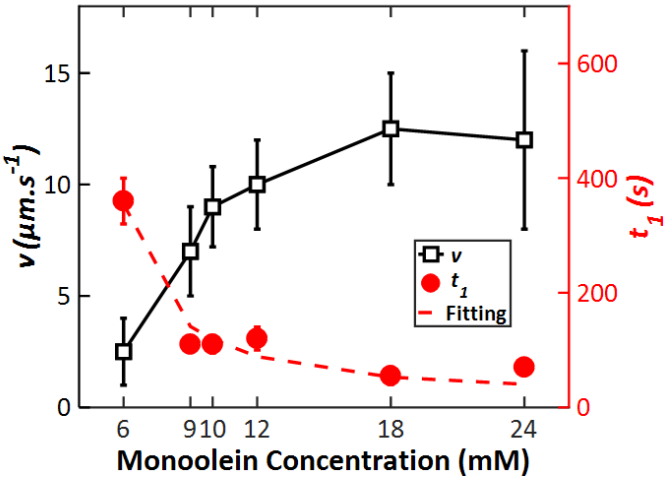


**Figure 3.10:** $t_1$ **and average velocity as a function of monoolein concentration.**

On the other hand, the higher the initial ethanol concentration is in the droplet, the farther the starting point is away from the coexist line, the longer the $t_1$ (Fig. 3.11a). For 30 % ethanol, it is very close to the coexist line, the phase separation happened fast and cannot be observed. For intermediate and high ethanol concentration, $t_1$ increases as a function of ethanol concentration (Fig. 3.11b). Average velocities stay constant.

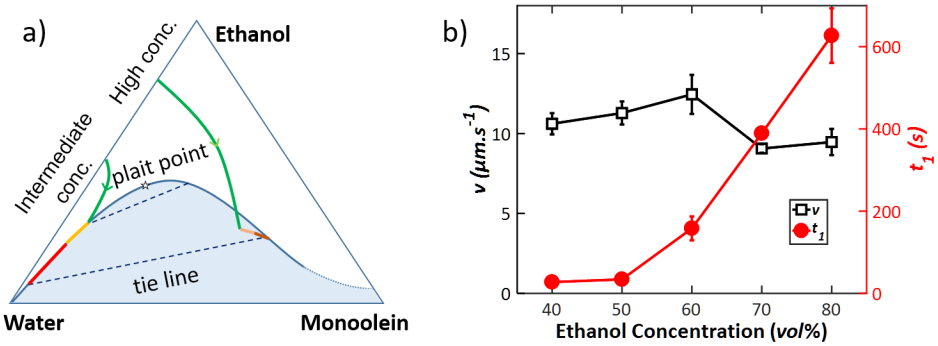


**Figure 3.11: a) Water/ethanol/monoolein phase diagram based on [76]. b) The duration time in stage 1,** $t_1$ **and average velocity as a function of ethanol concentration in the droplet.**

Although the phase separation of all droplets is triggered by monoolein absorption and ethanol release, the types of phase separation can be distinguished between droplets with intermediate (Fig. 3.2) and high ethanol concentration (Fig. 3.3). With intermediate ethanol concentration, nucleated small droplets stay inside the main droplet, merge with each other and later form trailing droplet. With high ethanol concentration, nucleated small droplets extrude and finally separate from the main droplet.

With NBD, which has a higher affinity to ethanol, ethanol-rich phase and water-rich phase can be distinguished in fluorescent images. In stage 2, for intermediate ethanol concentration, the ethanol-rich phase (bright spot) nucleate from the majority water-rich phase (Fig. 3.12a). While for high ethanol concentration, water-rich phase nucleate from the majority ethanol-rich phase (Fig. 3.12b).

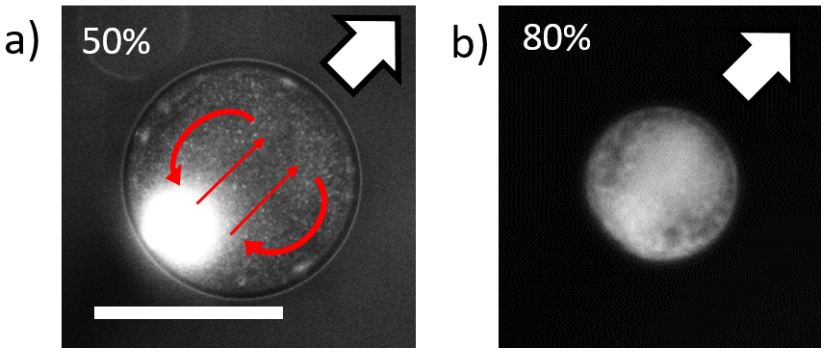


**Figure 3.12: Fluorescent images of droplets with initially 50% and 80% ethanol in stage 2.** a) With medium ethanol concentration, ethanol-rich phase (bright spots) nucleates from the water-rich phase. b) With high ethanol concentration, water (dark spots) nucleates from the ethanol-rich phase. The scale bar is 100 $\mu$m.

These different types of phase separation can be explained on the phase diagram. With medium ethanol concentration (40-60%), the droplet will reach the coexist line on the left side of the plait point, so the ethanol-rich phase is the minority phase and nucleates from the water-rich phase. In contrast, with higher initial ethanol concentration in the droplet ($70 - 80\%$), it takes longer until the phase separation starts. The droplet will reach the coexist line on the right side of the plait point, therefore it is the water-rich phase, which nucleates from the ethanol-rich phase (Fig. 3.9).

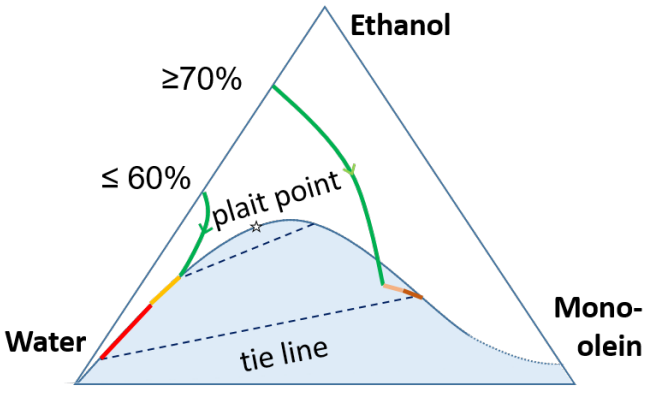


**Figure 3.13: A sketch of ternary phase diagram of water, ethanol and monoolein based on [76].**

## 3.3 Quantification of $t_1$

As introduced in section 3.2, the phase separation is triggered by monoolein absorption and ethanol release. Because the size of ethanol molecules is much smaller than monoolein micelle ($\sim$ 0.4 nm and $\sim$ 4 nm in diameter), the diffusion constant of monoolein micelle is much smaller than ethanol, the phase separation is limited by the slower material transport, namely the monoolein diffusion. In addition, it is difficult to find the exact ethanol concentration on the co-exist line on the water/ethanol/monoolein phase diagram (Fig. 3.6) when the phase separation starts. Therefore, the quantification of $t_1$ is done by considering the monoolein absorption.

In chapter 2, we calculate the Peclet number of the moving droplet $Pe = Rv/D$ by considering the radius of the droplet ($R \approx 50\ \mu m$), propulsion velocity ($v \approx 10\ \mu m$) and the diffusion constant of monoolein in squalane ($D = 2.6 * 10^{-12}\ m^2/s$). We get an estimation of $Pe \approx 200$, which means the transfer of monoolein is dominated by advective flow instead of diffusion. So there is a monoolein depleted region around the droplet (Fig. 3.14).

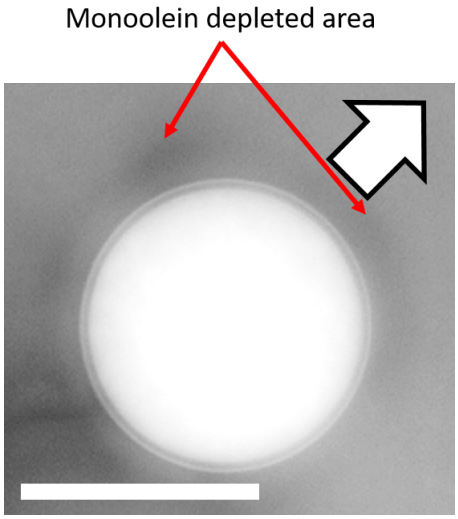


**Figure 3.14: A snapshot of a moving droplet in stage 1 with monoolein depletion area.** The droplet is made of 80% ethanol. The scale bar is 100 $\mu$m.

We assume that the thickness of the monoolein depleted region $\delta = 0$ at time $t = 0$ and it will grow as $\delta \approx \sqrt{Dt}$. When the droplet move with a constant velocity $v$, the average value $\langle\delta\rangle$ will scale with the convective time scale $t_c = R/v$ as $\langle\delta\rangle \approx \sqrt{Dt_c}$. Hence the total influx of monoolein during a time $t$ will be:

$$N = 4\pi R^2 j \approx 4\pi\sqrt{DvR^3}c_\infty t \tag{3.1}$$

We consider $c^*$ as the critical monoolein concentration in the droplet when the phase separation starts. Then the total absorbed monoolein will be $N = c^* 4\pi R^3/3$ and we can calculate the duration time of stage 1:

$$t^* \approx \frac{1}{3}\sqrt{\frac{R^3}{Dv}}\frac{c^*}{c_\infty} \tag{3.2}$$

where $c_\infty$ is the monoolein concentration in squalane (10 mM). Using the influx of molecules to the moving droplet derived from a more rigorous consideration by Levich [82] yields a prefactor $\sqrt{\pi(1+\lambda)/6}$ of Eq. 3.2 with the viscosity ratio $\lambda = \mu_{sq}/\mu_w \approx 36$.

On the ethanol/water/monoolein phase diagram (Fig. 3.11), the higher the initial ethanol concentration is in the droplet, the more monoolein is required to trigger phase separation, meaning larger $c^*$ value.

From equation 3.2, $t_1 \propto R^{3/2}$, which is consistent with the experimental data. In Fig. 3.15, it shows $t_1$ as a function of droplet radius with different ethanol concentrations. The dashed lines are fits to the data by fitting a prefactor $a$ in $t_1 = a * R^{3/2}$. By plugging in the numbers from experiment ($c_\infty$, $R$, $v$ and $D$), we get fitting parameter $c^* = 8 \pm 3$ mM for 50% ethanol droplets.

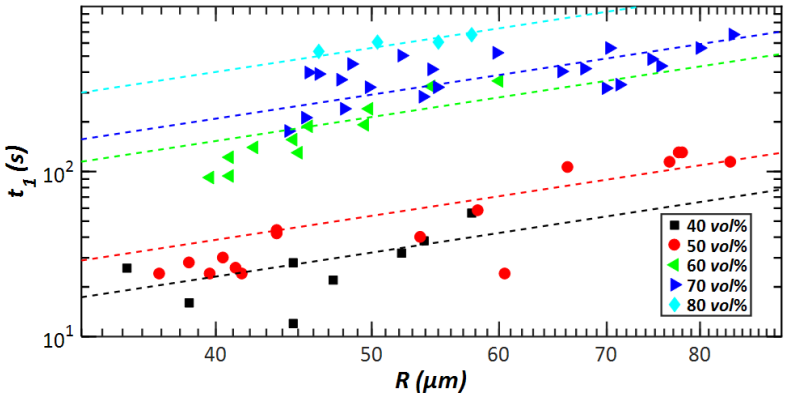


**Figure 3.15: $t_1$ as a function of droplet radius $R$ for different initial ethanol concentration.** The dashed lines are the fittings of Eqn. 3.2 with $t_1 = a * R^{3/2}$. The monoolein concentration in the continuous phase $c_\infty = 10mM$. The average moving velocity of the droplet $v = 10\ \mu m/s$.

By changing the initial monoolein concentration in squalane ($c_\infty$), keeping other parameters constant (50% ethanol in droplets, $R \approx 75\ \mu$m) and plugging in the numbers from experiment ($c_\infty$, $R$, $v$ and $D$), we get the fitting parameter $c^* = 13 \pm 4mM$ (Fig. 3.16).

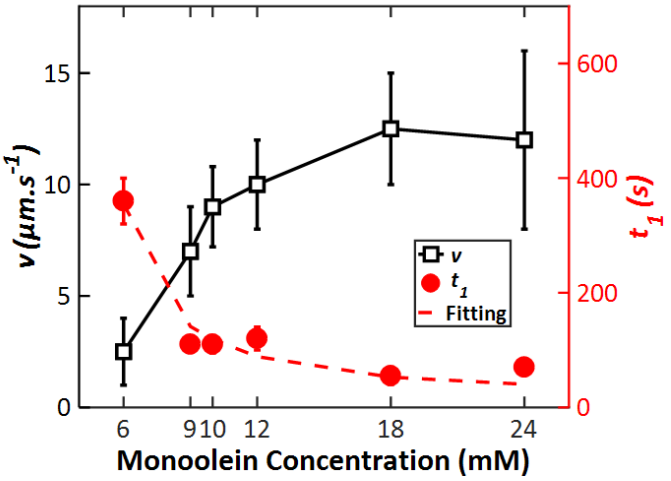


**Figure 3.16: $t_1$ and velocity as a function of initial monoolein concentration $c_\infty$.** The dashed lines are the fittings of Eqn. 3.2. The initial ethanol concentration in the droplets is 50%. The average radius of the droplets $R \approx 75\mu m$.

The critical monoolein concentration $c^*$ from the droplet tests match with the number we get from the bulk test. We assume that the droplet with the initial ethanol concentration of 50% is reduced to 40-45% at $t_1$. The fitted values of $c^*$ are 8 $\pm$ 3 mM and 13 $\pm$ 4 mM and the monoolein concentration required to trigger phase separation in a 40% ethanol/water mixture in bulk is 20 mM (Fig. 2.28).

The transition between stage 1 and stage 2 leads to phase separation and swimming mode change. The estimation of of $t_1$ provides us a handle for controlling the droplet behavior and furthermore temporal-controlled cargo delivery in chapter 5.

## 3.4 Driving mechanism in stage 1

There are two possible driving mechanisms in stage 1: release of ethanol and absorption of monoolein. These two driving mechanisms are not contradicted to each other and both of them are able to propel the droplet by Marangoni flow.

As mentioned above (Fig. 3.7), droplets loose volume in stage 1 during their movement. By exclusion, ethanol is solubilised into squalane. When the monoolein concentration is above the CMC in squalane, the solubilised ethanol molecules will fill or swell micelles or form compound with monoolein and deplete free monoolein in squalane. The monoolein depletion results in an increase of interfacial tension of the droplet, which is confirmed by interfacial tension measurement: the interfacial tension of a 50% ethanol droplet is 3.5 $\pm$ 0.5 mN/m in squalane with 10 mM monoolein and 4.5 $\pm$ 0.5 mN/m in ethanol saturated squalane with 10 mM monoolein.

On the other hand, droplets absorb monoolein from squalane in stage 1 during

the movement (Fig. 3.8). The depletion of monoolein will increase the interfacial tension of the droplet: the interfacial tension of a 50% ethanol droplet is 3.5 ± 0.5 mN/m in squalane with 10 mM monoolein and 11.5 ± 0.1 mN/m in squalane without monoolein. In addition, droplets have a tendency to avoid to cross the 'old' path, which is the monoolein depleted area (Fig. 3.17).

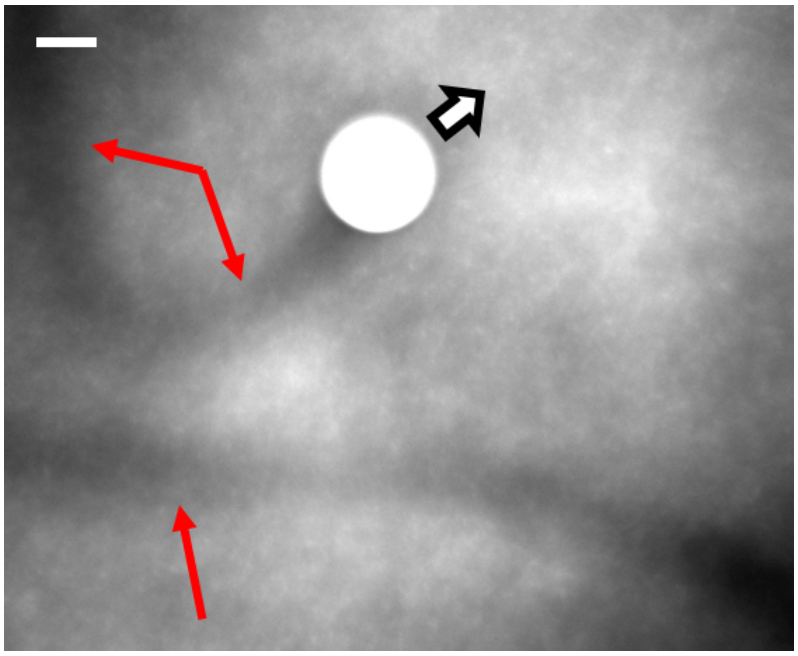

**Figure 3.17: A fluorescent image of a droplet avoiding to cross the path left by another droplet.** The droplets are made of 60% ethanol. The fluorescent dye NBD is initially added to the continuous phase to keep track of monoolein. The white arrow with black border indicates the moving direction of the droplet. The red arrows indicate the path of the droplet. The scale bar is 100 $\mu$m.

Either releasing ethanol or absorbing monoolein, the droplet will increase the interfacial tension. Once the droplet is displaced from the center by disturbance, it will be in contact with fresh monoolein micelles, which will decrease the interfacial tension at the leading end of the droplet. This leads to a Marangoni flow from the leading end to the rearing end of the droplet (Fig. 3.18). This flow drives the droplet forward toward more fresh monoolein micelles and maintain the surface tension gradient and the flow on the droplet interface.

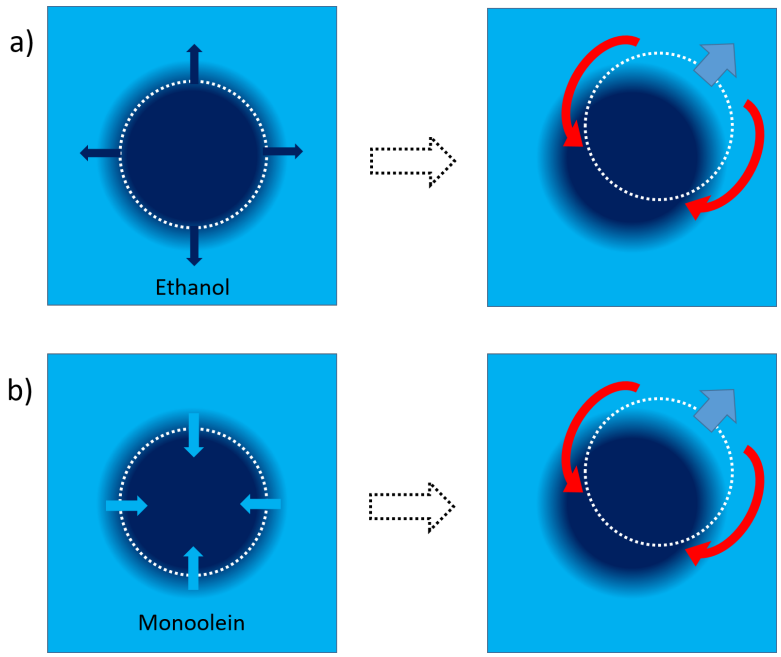


**Figure 3.18: A sketch of driving mechanism by a) release of ethanol and b) absorption of monoolein.** Dark blue indicates higher interfacial tension areas. The blue arrows indicates ethanol is solubilised into squalane in a) and monoolein is solubilised into the droplet in b). The red arrows indicate Marangoni flow. The grey arrow indicate the droplet moving direction.

For comparison, in a stable droplet without material transport between the droplet and the continuous phase, surfactant molecules are evenly distributed on the interface. The displacement of the droplet will lead to the surfactant accumulation on point A and decrease on point B due to the flow on the interface. The correspond Marangoni flow will be from point A to B and push the droplet back to the original center (Fig. 3.19).

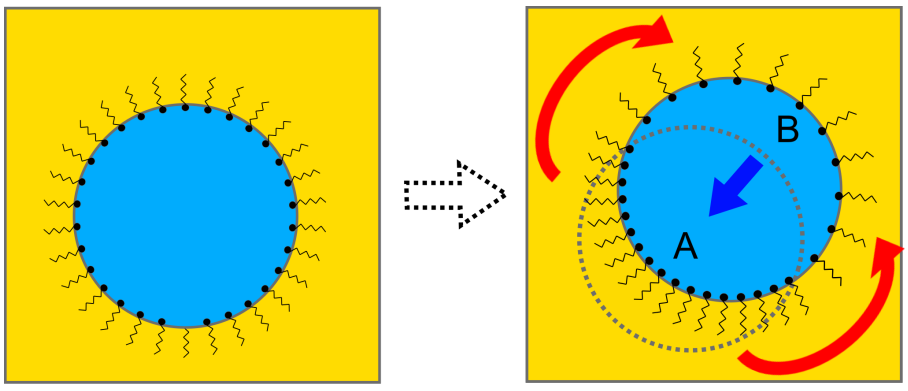


**Figure 3.19: A sketch of a stable droplet.** When a stable droplet is displaced from the original position (dotted circle), it leads to an uneven distribution of surfactant. Marangoni flow, which is drawn by red arrows, will push the droplet back. The blue arrow shows the moving direction of the droplet.

To distinguish whether ethanol release or monoolein absorption plays a bigger role by propulsion, we observe the flow on the interface of a 100% ethanol droplet without the influence of monoolein on the interfacial tension measurement device (droplets become unstable in squalane without monoolein and typically stick to the bottom in the reservoir therefore only pendent droplets can be observed). Extra µPIV tracing particles are added to the droplet to help to visualize the flow on the interface, which is about 10 $\mu$m/s. On the other hand, the flow on the interface of a 100% ethanol droplet in squalane with 10 mM monoolein is about 50 $\mu$m/s.

Although we cannot exclude the driving mechanism of ethanol release, the experiment results show that monoolein absorption is the dominating driving mechanism: the interfacial tension difference caused by monoolein absorption is larger (8 mN/m) than ethanol release ($\sim$ 1 mN/m) and the Marangoni flow caused by monoolein absorption is faster (50 $\mu$m/s) than ethanol solubilization (10 $\mu$m/s). In addition, this would also agree with the finding that the moving velocity increases with monoolein concentration (Fig. 3.11) while it is unchanged with ethanol concentration (Fig. 3.11b). However, both effect are not completely independent from each other.

## 3.5 Movement in stage 2

In stage 2, during the phase separation, the system is complex and the driving mechanism could be a combination of the driving mechanism in stage 1 and stage 3. The velocity increase linearly (Fig. 3.4). The duration time in stage 2 increases and the acceleration in stage 2 decreases by increasing the droplet size (Fig. 3.20). The acceleration in stage 2 is determined by the slope of the linear fit of velocity-time function in stage 2.

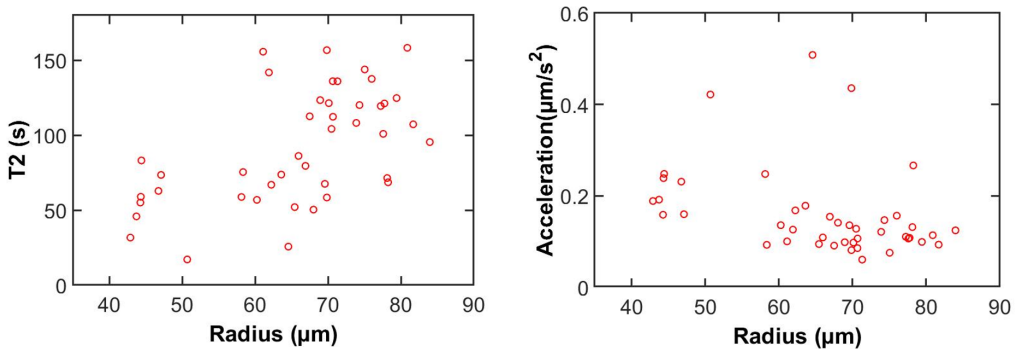


**Figure 3.20: The duration time and the acceleration in stage 2 as a function of droplet radius.**

## 3.6 Janus droplet in stage 3

For intermediate ethanol concentration, ethanol-rich phase nucleated in the droplet are transported to the rear end of the droplet and accumulated in stage 2. By the end of stage 2, a Janus droplet with the water-rich phase in the front and the ethanol-rich phase at the end.

In stage 3, the main droplet is dark and the trailing droplet is bright under fluorescent microscope by adding NBD into squalane/monoolein at the beginning. This proves that the main droplet is water-rich phase and the trailing droplet is ethanol-rich phase (high affinity with NBD/monoolein, Fig. 3.21).

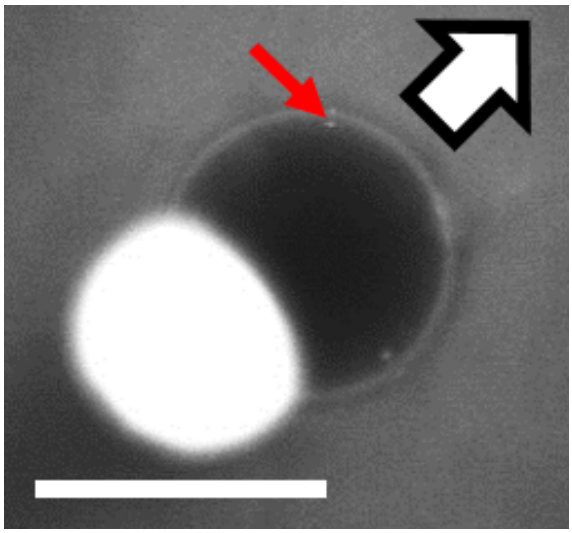

**Figure 3.21: Fluorescent images of droplets in stage 3.** The main droplet is dark (water-rich phase) and the trailing droplet is bright (ethanol-rich phase). The scale bar is 100 $\mu$m.

The volume of the main droplet decreases and the volume of the trailing droplet increases. Because of the complex geometric shape of the trailing droplet and overlapped by the main droplet, only the volume of the main droplet, which is reasonably close to a sphere, is measured and plotted. In this case, the main droplet loose more than 20% volume in stage 3 (red line in Fig. 3.22). The moving velocity decreases about exponentially (black line). When calculating the volume, the main droplet is considered as a sphere and the interfacial part between the two droplets (red dashed line) are ignored.

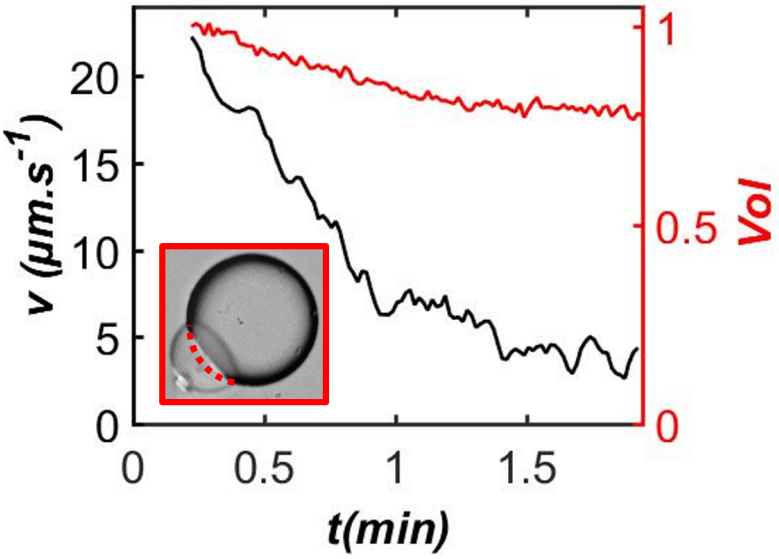


**Figure 3.22: Velocity and volume of the main droplet as a function of time in stage 3.** The initial radius of the main droplet is 42 $\mu$m.

There appear 'tiny' droplets on the surface of the main droplet. These 'tiny' droplets are transferred to the rear end by the flow on the surface and merge with the trailing droplet (Fig. 3.23). Since these 'tiny' droplets can be seen under optical microscope (20X lens), these 'tiny' droplets must be larger than 1 $\mu$m. These 'tiny' droplets can better observed under fluorescent microscope (Fig. 3.21).

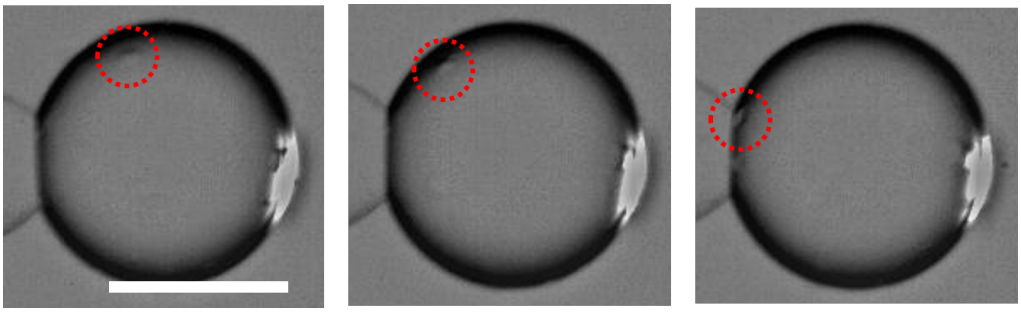

**Figure 3.23: One 'tiny' droplet is transferred to the rear end** The scale bar is 100 $\mu m$, the interval between each two frames is one second

Combining the volume change between the main droplet and the trailing droplet and 'tiny' droplets appearance, it indicates that a phase separation continues on the surface of the main droplet in stage 3, although it is weaker than in stage 2.

## 3.7 Driving mechanism in stage 3

In stage 3, nucleated ethanol-rich phase start to accumulated at the rear end of the droplet and form a trailing droplet. Because of the high affinity of monoolein to

ethanol, the new-formed trailing droplet will absorb monoolein from the interface of the droplet and create a surface tension gradient. This leads to a Marangoni flow on the surface and propel the droplet move (Fig. 3.24). The interfacial tension of a 70% ethanol droplet, which indicates ethanol-rich phase, is 4.9 ± 0.6 mN/m in squalane with 10 mM monoolein and the interfacial tension of a 30% ethanol droplet, which indicates water-rich phase, is $< 1$ mN/m. Droplets with higher ethanol proportion than 70% become unstable and therefore it is difficult to do interfacial tension measurement.

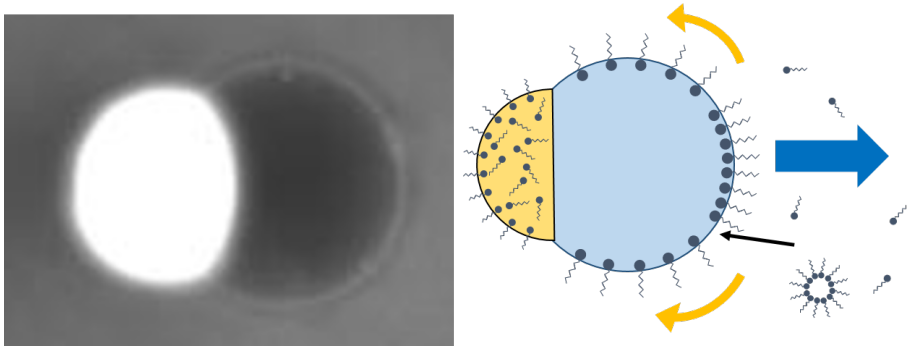

**Figure 3.24: A sketch of a droplet in stage 3 with surfactant to illustrate driving mechanism.** The black arrow indicates the droplet absorb monoolein from the continuous phase. The yellow arrows indicate the Marangoni flow on the droplet interface. The blue arrow indicates the droplet moving direction.

### 3.7.1 Moving direction affected by 'tiny' droplets

The 'tiny' droplets on the surface of the main droplet are in fact like the big trailing droplet, which is made of ethanol-rich phase with high affinity to surfactant. 'Tiny' droplets will absorb surfactant around them and create higher interfacial tension areas. 'Tiny' droplets are therefore not only attracted by the trailing droplet but they will also attract each other (Fig. 3.25).

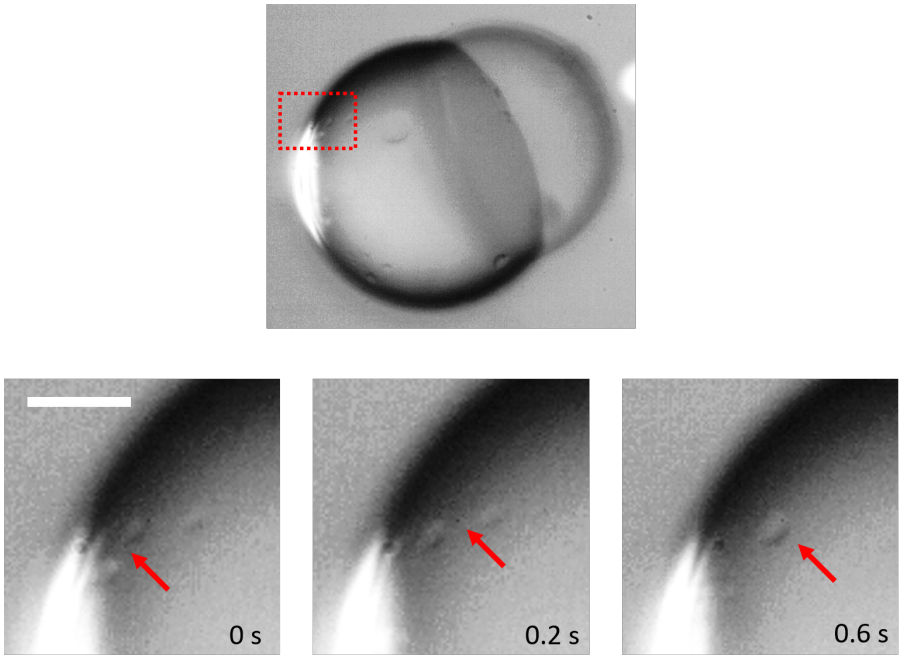


**Figure 3.25: Snap shots of 'tiny' droplets attracting and merging to each other.** The scale bar is 30 $\mu$m.

More over, these 'tiny' droplets can also influence the moving direction of the main droplet. If the left and right sides of the main droplet have similar numbers of 'tiny' droplets, the main droplet will go straightly forward (Fig. 3.26a). If one side has more 'tiny' droplets, which reduce the surfactant coverage on this side, it creates a larger surface tension gradient on this side of the main droplet, respectively a stronger Marangoni flow (Fig. 3.26b). The main droplet turns to the opposite direction. Thus the (random) moving direction of the main droplet can be 'predicted' by the distribution of these 'tiny' droplets.

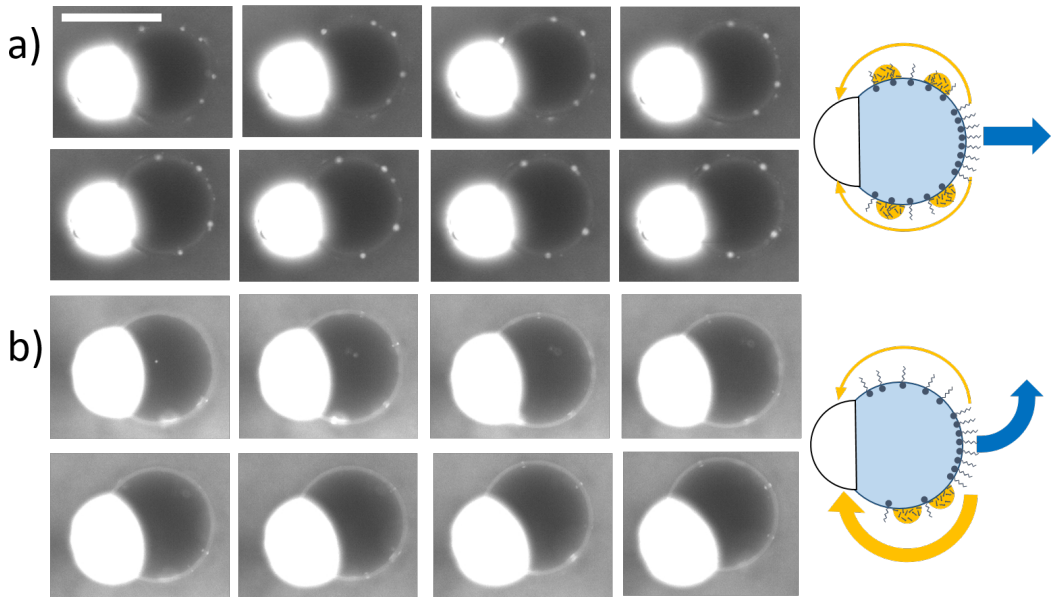


**Figure 3.26: Moving direction of the main droplet 'predicted' by 'tiny' droplets distribution.** The main droplet moves straight forward when 'tiny' droplets are evenly distributed on the left and right sides. The main droplet turns to the opposite side where there are more 'tiny' droplets on one side. The yellow dots indicate 'tiny' ethanol-rich droplet. The thicker yellow arrows indicate stronger Marangoni flow. The blue arrows indicate droplet moving directions. The scale bar is 100 $\mu$m.

### 3.7.2 Mathematical model for stage 3

Here is a model with calculation that describe the motion of the droplet in stage 3. First we consider the monoolein concentration in the trailing droplet, $n = N/V$, where $N$ is the number of monoolein molecules and $V$ is the volume of the trailing droplet. The rate of change of the monoolein concentration can be written as:

$$\dot{n} = \frac{\dot{N}}{V} - \frac{N\dot{V}}{V^2} \ . \tag{3.3}$$

where the dot is an abbreviation for a time derivative. The flux $\dot{N}$ of monoolein molecules into the trailing droplet is controlled by two processes. First, the freshly nucleated ethanol-rich phase that also contains a certain amount of monoolein molecules coalesce with the trailing droplet $\dot{N}_d$. Second, monoolein molecules are absorbed from the continuous phase to the interface of the water-rich droplet. They are then transported towards ethanol-rich phase through the three phase contact line at a rate $\dot{N}_c$.

In the following model for the droplet motion in stage 3, we will neglect the influx of small droplets and the volume change of both the trailing and the leading droplet and concentrate only on the adsorption via the surface of the water-rich droplet. Hence, we have $\dot{N}_c = 0$ and $\dot{V} = 0$ and the change of monoolein concentration in

the trailing droplet can be simply written as:

$$\dot{n} = \frac{2\pi\, R\, \Gamma\, v}{V}\ , \tag{3.4}$$

where $R$ is the radius of the main droplet and $\Gamma$ the surface coverage of monoolein molecules on the interface between the water-rich phase and squalane and $v$ the velocity of the droplet.

We define the dimensionless undersaturation of monoolein molecules in the trailing droplet:

$$x \equiv \frac{n_\infty - n}{n_\infty - n_0} \tag{3.5}$$

where $n_0$ and $n_\infty$ are the concentration at $t = 0$ and for $t \to \infty$. which is equivalent to the rate of change of the non-dimensionalized monoolein undersaturation.

Using the definition Eqn. 3.5 we can express the rate of change Eqn. 3.4 as

$$\dot{x} = -\frac{2\pi\, R\, \Gamma\, v}{(n_\infty - n_0)\, V} \tag{3.6}$$

The velocity $v$ of droplet can be determined by a balance between injected power released by the monoolein molecules and the power dissipated in viscous flows. The power of dissipated work in viscous flows is given by

$$\mathcal{P}_{diss} = 6\pi\, C\, \eta\, R\, v^2 \tag{3.7}$$

where $\eta$ is the dynamic viscosity of the droplet phase. The numerical prefactor $C$ depends on the geometry and the ratio of the viscosities of the droplet phase to the continuous phase.

The power injected to the Janus droplet through the uptake of monoolein collected from the interface can be written as

$$\mathcal{P}_{inj} = (\mu_\infty - \mu)\, \dot{N}_c = 2\pi\, (\mu_\infty - \mu)\ R\, \Gamma\, v \tag{3.8}$$

where $\mu$ is the chemical potential. From the balance $\mathcal{P}_{diss} = \mathcal{P}_{inj}$, we obtain the droplet propulsion velocity

$$v = \frac{(\mu_\infty - \mu)\, \Gamma}{3C\, \eta} \tag{3.9}$$

The same maximum propulsion velocity can be obtained from a balance of the Marangoni stress $f_\parallel^{(\mathrm{Ma})}$ acting on the interface of the leading droplet and dissipation in viscous flows. Employing the Gibbs adsorption isotherm $d\gamma/d\mu = -\Gamma$ and the estimate $\partial\mu/\partial s \approx (\mu_\infty - \mu_t)$, the Marangoni stress on the surface of the leading droplets can be recast in the form:

$$f_\parallel^{(\mathrm{Ma})} = \frac{\partial\gamma}{\partial s} = \left.\frac{\partial\gamma}{\partial\mu}\right|_{\mu=\mu(s)} \frac{\partial\mu}{\partial s} \approx \frac{\pi\Gamma(\mu - \mu_\infty)}{R} \tag{3.10}$$

The Maragoni stress is balanced by viscous stress

$$f_\parallel^{(\mathrm{visc})} \approx \frac{\eta v}{R} \tag{3.11}$$

which yields, besides a dimensionless prefactor, the same dependence as Eq. (3.9).

To describe the velocity relaxation in stage 3, we employing a linear expansion

$$\mu_\infty - \mu = \left.\frac{\partial \mu}{\partial n}\right|_{n=n_\infty} (n_\infty - n) + \mathcal{O}\left((n_\infty - n)^2\right) \tag{3.12}$$

we can rewrite Eqn. (3.6) in the form as following

$$\dot{x} = -\frac{2\pi\, R\, \Gamma^2}{3\, C\, \eta\, V} \left.\frac{\partial \mu}{\partial n}\right|_{n=n_\infty} x \ . \tag{3.13}$$

According to the linear approximation in our model, the propulsion velocity $v(t)$ of the droplet is strictly proportional to the non–dimensional monoolein undersaturation in the trailing droplet:

$$v(t) = v_{max}\, X(t) \tag{3.14}$$

Hence, the maximum velocity $v_{max}$ is attained for the maximum possible difference of chemical potential on the droplet surface:

$$v_{max} = \frac{(n_\infty - n_0)\Gamma}{3C\,\eta} \left.\frac{\partial \mu}{\partial n}\right|_{n=n_\infty} \ . \tag{3.15}$$

The solution of Eqn. (3.13) is an exponential decay

$$v(t) = v_{max} exp\Big(-\frac{t}{\tau}\Big) \tag{3.16}$$

with a time constant

$$\tau^{-1} = \frac{2\pi\, R\, \Gamma^2}{3\, C\, \eta\, V} \left.\frac{\partial \mu}{\partial n}\right|_{n=n_\infty} \tag{3.17}$$

Given the same ethanol-water composition at the beginning of stage 1, the volume of the trailing droplet in stage stage 3 scales as $V \sim R^3$ with the radius $R$ of the initial mother droplet. Hence, we conclude that the relaxation time in stage 3 as given by Eqn. (3.17) scales as $\tau \sim R^2$ (Fig. 3.27a).

According to the experimental results, $v_{max}$ is a constant value of around 20 $\mu$m/s and independent from the size of droplets (Fig. 3.27b). The values of $\tau$ are obtained from fits of the experimentally measured decay of the self-propulsion velocity from equation

$$v = a * e^{\frac{t-t_0}{\tau}} + v_0 \tag{3.18}$$

where $a$ is a prefactor, $t_0$ is the time delay, $v_0$ is the final velocity after decay before stop moving. Fig. 3.27c shows the variation of $\tau$ between droplets with different radii. The blue line in Fig. 3.27c indicates the fit of equation $a * (r)^c$, where $a$ is the prefactor. $c = 1.6 \pm 0.3$.

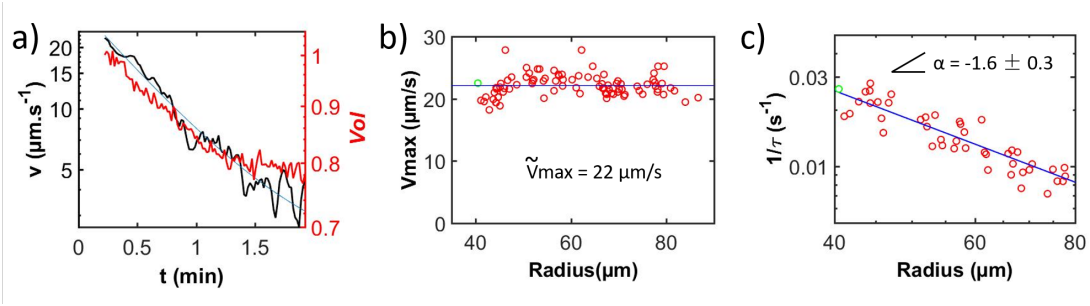


**Figure 3.27: a) One example of fitting of $\tau$. b) Vmax is independent from size of the droplets. c) $\tau$ as a function of droplet radii.** The green data point in b) and c) is from the data in a)

This model predicts a maximum velocity at the end of stage 2, which is correspond to a maximum chemical potential difference between the two droplets interface. It also predicts an exponential decay in stage 3, where the time constant presents a geometrical dependence. The variation between the model and the experimental result can be caused by the assumption of constant volume of the droplet and the nucleation on the main droplet interface.

## 3.8 Robustness of self-propelled droplet

The self-propelled droplet system introduced in the thesis is very robust. Not only droplets with different ethanol concentration could move (although the behavior in stages are different), but self-propelled droplet could be build by different system or with very complex extra components in droplet phase, as long as the following conditions are met: the droplet is made of water and a water-miscible solvent. The solvent should be less polar than water and partially soluble in oil. The continuous phase is made of oil and an oil-soluble surfactant. The surfactant should be more soluble in the solvent.

In the demonstration, squalane (the oily phase) is replaced by squalene, monoolein (the surfactant) is replaced by span 80, DOPC (1,2-dioleoyl-sn-glycero-3-phosphocholine) and DPHPC (1,2-diphytanoyl-sn-glycero-3-phosphocholine) respectively, ethanol by isopropanol and methanol respectively. For easy comparison, there is only one component is replaced in each test. Droplets in all of these chemical combinations propel in stage 1. In some specific cases (E.g. 50% isopropanol/water mixture in squalane/monoolein), droplets can phase separation, evolve to Janus droplets and move in stage 2 and stage 3 as described above in section 3.1 (Fig. 3.28).

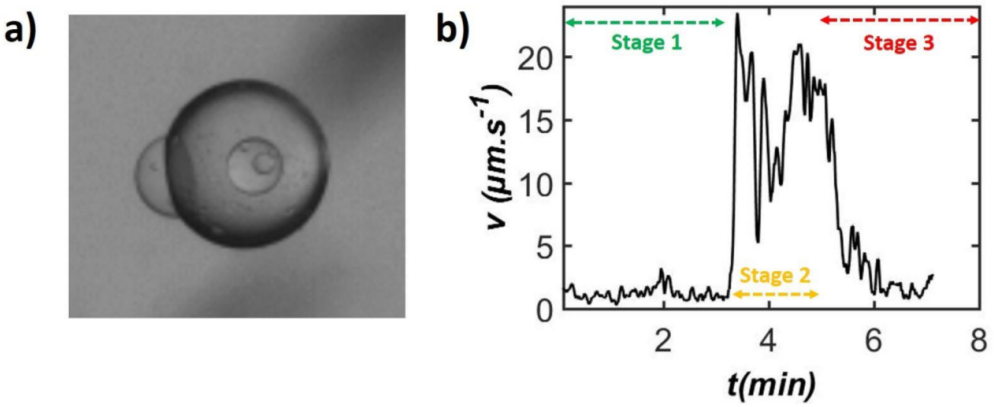


**Figure 3.28: a) A snap shot of a Janus droplet with a radius of $\sim$ 100 $\mu$m, made of 50% isopropanol/water. b) Velocity-Time diagram of the droplet presented in panel a).**

More over, the whole droplet phase can be replaced by commercial alcohol (Calvados $^{TM}$, Ouzo $^{TM}$, Cachasa $^{TM}$, Boukha $^{TM}$, Grand Marnier $^{TM}$, Rhum (Stroh $^{TM}$), Ricard $^{TM}$, Gin (Colonex Foxtrot $^{TM}$), Digestif (Mett $^{TM}$), Whisky (asahi $^{TM}$), Ricard $^{TM}$, Vodka (absolute vodka $^{TM}$) and Jagermeister $^{TM}$). Droplets are produced with method 1 in Fig. 2.16.

| Name | Eth % | CR | PS | V | T |
|---|---|---|---|---|---|
| Stroh | 80 | 100-115 | Y | 20 | 12 |
| Cucaracha | 40 | 40-100 | Y | 25 | 8 |
| Gin Foxtrot | 40 | 140-180 | N | 30 | 8 |
| Cachasa | 40 | 40-100 | N | 20 | 7 |
| Calvados | 40 | 30-65 | N | 23 | 4.5 |
| Gin London N1 | 47 | 27-31 | N | 17 | 4.5 |
| Boukha | 40 | 30-40 | N | 17 | 4.5 |
| Gin Gibson | 37 | 49-57 | N | 19 | 4 |
| Ouzo | 40 | 10-22 | N | 8 | 3.5 |
| Vodka | 37.5 | 25-60 | Y | 25 | 3 |
| Whisky | 51 | 10-18 | Y | 10 | 3 |
| Grand manier | 40 | 20-35 | Y | 14 | 3 |
| Jagermeister | 35 | 30 | N | 6 | 2.5 |
| Ricard | 40 | 20-70 | Y | 40 | 2.5 |
| Digestif | 40 | 10-17 | Y | 10 | 2 |

**Table 3.1: A list self-propelled droplets made of commercial alcohol.** Note: CR: cruising range in droplet diameter, PS: phase separation, V: maximum velocity ($\mu$m/s), T: Cruising Time (min).

All these tested liquors could be employed to produce self-propelled droplets with some size restrictions. For example: Calvados $^{TM}$, Cachasa $^{TM}$, Boukha $^{TM}$ and Jagermeister $^{TM}$ propel only if their radii smaller than 20 $\mu$m.

For some tested liquors (Grand Marnier $^{TM}$, Rhum (Stroh $^{TM}$), Ricard $^{TM}$, Digestif

(Mett $^{TM}$), Whisky (Asahi $^{TM}$), Vodka (Absolute Vodka $^{TM}$)), droplets can phase separation and form Janus droplets, i.e. as described for the standard system (Fig. 3.21). Moreover during the phase separation and after the Janus droplet formation, their velocity dependence presents the same characteristics in stage 2 (linear increase) and stage 3 (exponential decay), which is very similar to the droplets made of pure ethanol/water (Fig. 3.29).


**Figure 3.29: Velocity-time diagram of a self-propelled droplet made of Vodka.**

As demonstrated, the self-propelled droplets made of ethanol/water mixture are not strongly affected by the extra chemical composition in the droplets.

# Chapter 4

# Cargo delivery

As introduced in chapter 4, the self-propelled droplet phase separate during the movement. This inspired us that the droplet could be a carrier, which can spontaneously accumulate a chemical reagent to one of the phase and deliver it. Besides, the droplets have different hydrodynamic swimming modes and wetting properties, which result in different interaction with the geometry and the coating of obstacles, in different stages. These different interactions inspired us that the droplet can perform cargo delivery to a target with a specific geometry and coating. The robustness of the droplet with different/extra chemical component (Sec. 3.8) and controlled stage transition timing (Sec. 3.3) guaranty the desired movement of droplet.

In this chapter, we will first present that DNA can be adjusted to accumulate either into the water-rich phase or into the ethanol-rich phase during the phase separation (Fig. 4.1a,b). Then we will demonstrate that the ethanol-rich phase (with accumulated DNA) can be selectively delivered as a cargo to a certain target (Fig. 4.1c). The initial ethanol concentration in the droplet is fixed to 50%.

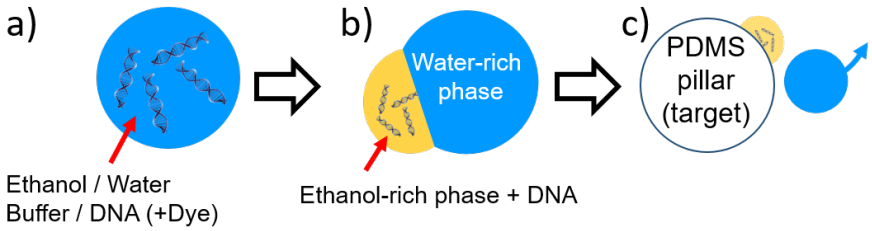


**Figure 4.1: A sketch of DNA precipitation and delivery done by self-propelled droplet.**

## 4.1 Cargo preparation: DNA precipitation

When DNA is added to the self-propelled droplet without salt, DNA is more soluble in water and stays in the main water-rich droplet after phase separation (Fig. 4.2a).

The solubility of DNA in water is decreased by adding salt (Sec. 2.9). So with salt, DNA is more soluble in ethanol and precipitated in the trailing ethanol-rich droplet (Fig. 4.2b).

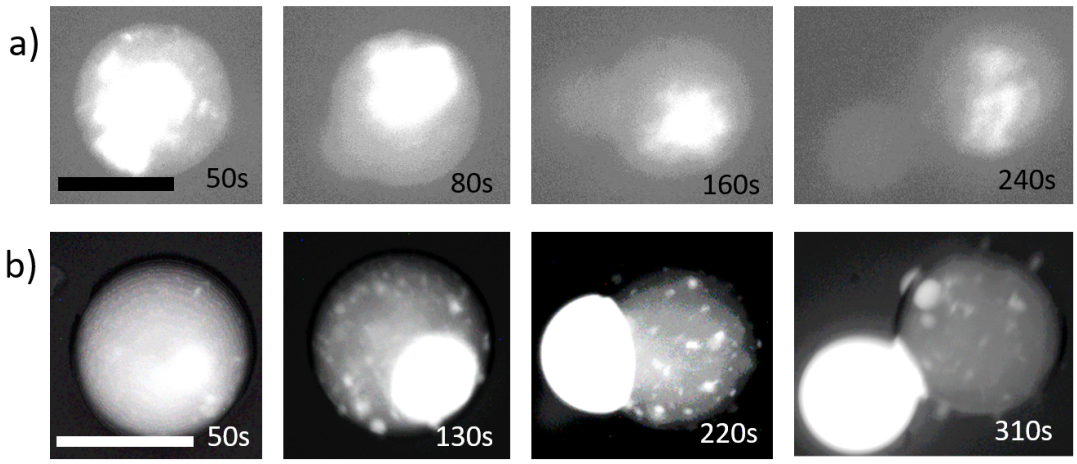


**Figure 4.2: Snap shots of DNA precipitation visualized by UV light.** Both droplets are made of 50% ethanol/water with 0.2 mg/ml DNA, 0.25 mg/ml Hoechst 33342. a) without any salt in the droplet, the DNA remains in the water-rich phase. In b), extra 25 mg/ml sodium acetate is added. As a result, the DNA is precipitated to the ethanol-rich phase. Both scale bars are 100 $\mu$m.

As demonstrated above, we can control DNA to either stay in the water-rich phase or to the ethanol-rich phase by adding salt. Ideally we could also separate DNA and RNA having different precipitation character. We tried to distinguish DNA and RNA with the fluorescent dye Acridine Orange (AO), which has different excitation and emission maximum, depending on whether it is bounded to DNA or RNA (Sec. 2.9 [80]). However, in our experiment, no matter bounded to DNA or RNA, the fluorescent signal is much stronger under blue laser (Fig. 4.3a,c) than the signal under green laser, which was always close to the background (Fig. 4.3b,d). Therefore, we cannot use AO to distinguish DNA and RNA and the rest of the fluorescent images in this chapter are exclusively excited by blue laser.

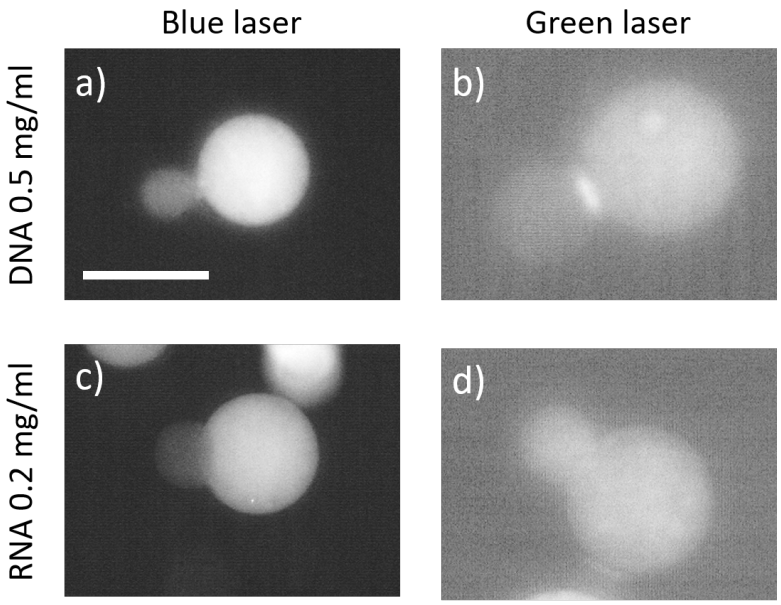


**Figure 4.3: Fluorescent images of DNA and RNA bounded to Acridine Orange and excited by blue laser (a,c) and green laser (b,d).** The droplets are made of 50% ethanol/water with 0.5 mg/ml DNA plus 10 $\mu$g/ml AO (a,b) and with 0.2 mg/ml RNA plus 10 $\mu$g/ml AO (c,d). The scale bar is 100 $\mu$m.

We also tried to look for a salt with a certain concentration, with which the (most) DNA stays in the water-rich phase and the (most) RNA is precipitated to the ethanol-rich phase. We used lithium chloride (LiCl), which supposed to precipitate RNA more efficient than DNA by binding with ribosome [83] [84]. We added DNA/RNA (both 0.5 mg/ml), AO (10 $\mu$g/ml) and LiCl (until to 0.25 mg/ml) to the droplet phase (50% ethanol). Without LiCl, both DNA and RNA remain preferentially in the water rich phase, i.e. the main droplet (Fig. 4.4a, d). By adding 0.25 mg/ml (0.6 M) LiCl to the droplet phase, both DNA and RNA precipitate to the ethanol-rich phase during phase separation, whereas the rate of precipitating for RNA and DNA is very similar (Fig. 4.4b, e). For comparison, by adding Sodium Acetate, both DNA and RNA can be precipitated but also no preference, DNA/RNA is more precipitated (Fig. 4.4c, f).

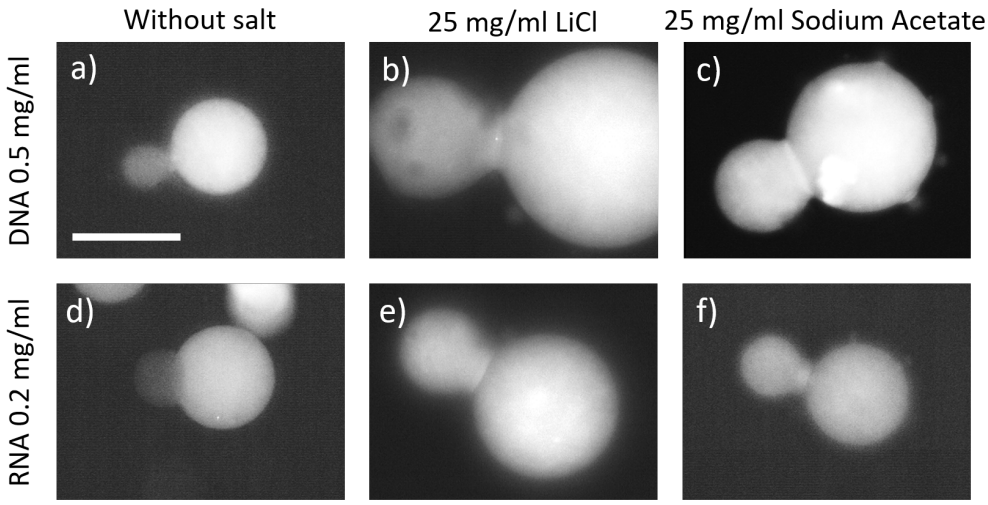


**Figure 4.4: DNA and RNA precipitation by LiCl and Sodium Acetate.** In a) and d), no DNA or RNA is precipitated without any salt. In b) and e), both DNA and RNA are precipitated by LiCl but significant difference. In c) and f), both DNA and RNA are precipitated by Sodium Acetate. The scale bar is 100 $\mu$m.

Although we could not separate DNA from RNA, we can control DNA or RNA individually to stay in the water-rich phase or precipitate to the ethanol-rich phase by (not) adding salt.

## 4.2 Selective cargo delivery

As demonstrated above, DNA can be accumulated to the trailing droplet in a controlled way. Next, the trailing droplet will be delivered as a cargo to a certain target. This cargo delivery can be divided to two steps: First, the droplets approach to the target guided by long-range hydrodynamic interaction. Second, the droplets attache to the target, which is dominated by wettability.

The long-range hydrodynamic interaction depends on the interaction of the droplets in their particular swimmer modes with the geometry shape of the obstacles. It is shown in [42] [44], that a pusher, i.e. our self-propelled droplets in stage 1 (Fig. 3.5a), will be attracted to circular pillars by virtue of their flow fields and move around the pillar. For a similar mechanism, a pusher will be attracted to square pillars but it will leave the pillar corner. On the other hand, after the phase separation in stage 3, a self-propelled droplet becomes a neutral squirmer (Fig. 3.5c). It will be attracted when it approaches to a straight interface, i.e. one side of a square pillar, like a pusher. But it will be repelled by a circular interface of a circular pillar, which is a few times larger than the droplet in radius.

After the droplet approach the pillar, the short range interaction, which is dominated by the wettability of the droplet on the pillar, determines if the droplet is attached to the pillar or sliding on and later escaping from the pillar. The wettability is decided by the ethanol fraction in the droplet and the coating of the pillar.

A 50% droplet has a low contact angle on PDMS, so it will be stick to a PDMS pillar once touching it. In contrast, a droplet with the same ethanol concentration has a high contact angle on Teflon, so it can slide on a Teflon coated pillar. After phase separation, the ethanol rich phase will be attached to both PDMS pillars and Teflon coated pillars.

Next, four different delivery scenarios are presented. a) When a pusher droplet approach to a circular pillar in stage 1, it will be attracted by hydrodynamic interaction to the pillar and either attach to the PDMS pillar directly (Fig. 4.5a,b) or move around the Teflon coated pillar until phase separation. For both cases, by the end of stage 3, ethanol-rich phase stays on the pillar and water-rich phase moves away (Fig. 4.5c,d).

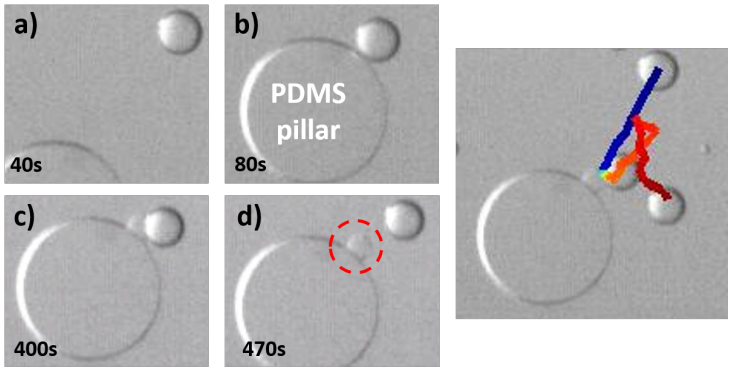


**Figure 4.5: Time series of a drop being attracted hydrodynamically to a round PDMS pillar in stage 1 and delivering cargo in stage 3.** The diameter of the pillar is 600 $\mu$m. The droplet moves from blue to red on the color coded trajectory.

b) When a pusher droplet approach to a square pillar in stage 1, it will be attracted by hydrodynamic interaction to the pillar (Fig. 4.6a,b). If there is no coating on the pillar, the droplet will attach to it directly by wetting. If the pillar is coated with Teflon, the droplet will slide along the wall and detach at the corner (Fig. 4.6c,d).

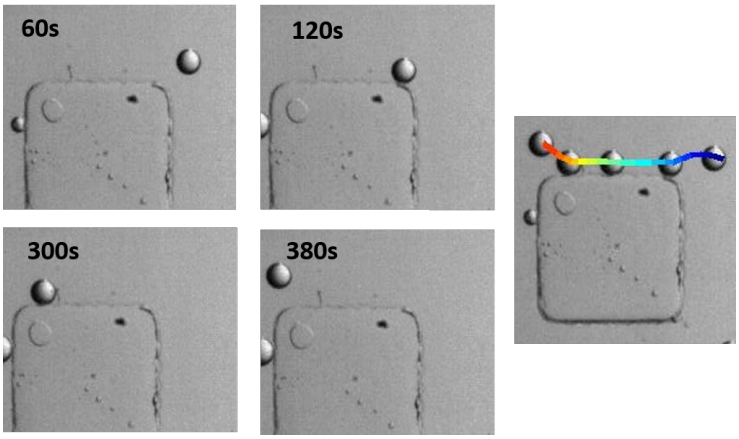


**Figure 4.6: Time series of a drop being attracted to a square Teflon coated pillar in stage 1, but escaping at the corner with no cargo delivery.** The side length of the pillar is 600 $\mu$m. The droplet moves from blue to red on the color coded trajectory.

c) When a neutral squirmer droplet approach to a circular pillar in stage 3, it will be repelled by hydrodynamic interaction and no cargo delivery (Fig. 4.7).

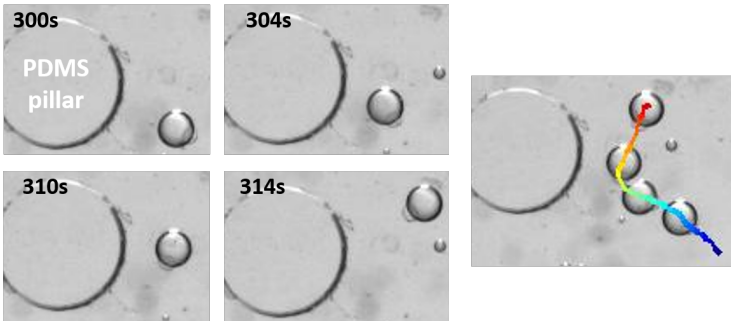


**Figure 4.7: Time series of a drop being repelled by a round pillar in stage 3.** The diameter of the pillar is 600 $\mu$m. The droplet moves from blue to red on the color coded trajectory.

d) When a neutral squirmer droplet approach to a square pillar in stage 3, it will be attracted by hydrodynamic interaction to the pillar. No matter with Teflon coating or not, the ethanol-rich phase will wet the surface, attach to it and deliver the cargo (Fig. 4.8).

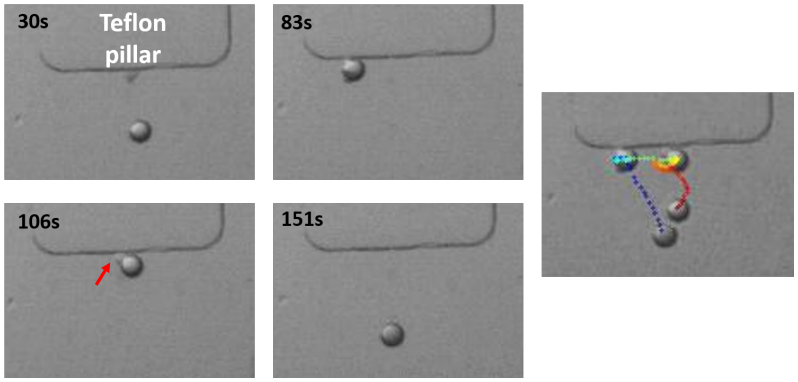


**Figure 4.8: Time series of a drop being attracted to a square Teflon coated pillar in stage 3 and ethanol-rich phase attached to the pillar.** The side length of the pillar is 600 $\mu$m. The droplet moves from blue to red on the color coded trajectory.

Fig. 4.9 summarizes all the delivery scenario (from left to right on the graph):

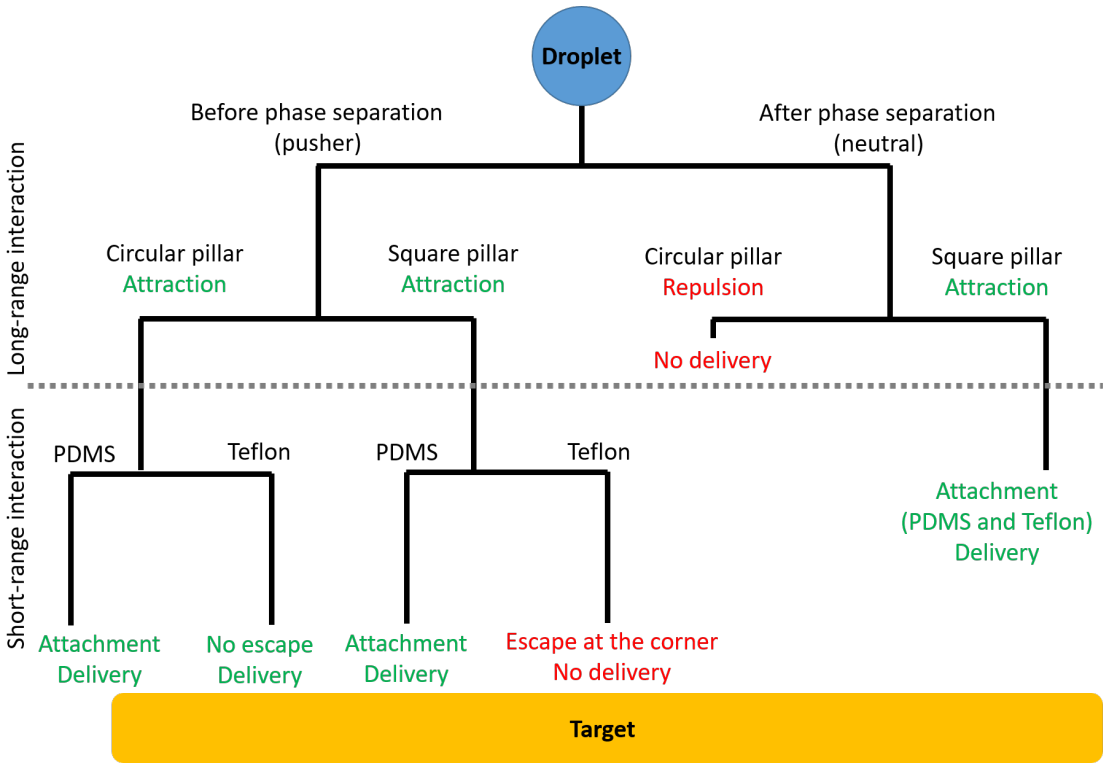


**Figure 4.9: A sketch of full delivery scenario.**

In conclusion, we demonstrate that the self-propelled droplet can delivery cargo in two steps. First, the self-propelled droplet can 'produce' the 'cargo' in a controlled way, by precipitating DNA or RNA to the ethanol-rich phase during phase separation. Second, the self-propelled droplet can make a controlled 'cargo' delivery, taking advantage of long-range hydrodynamic interactions, which is dominated by the swimming modes in stage 1 and 3 and target shape and short-range interac-

tions, which is dominated by the wetting properties of droplets in stage 1 and 3 and target surface coating.

# Chapter 5

# Chemotaxis effect

Once an ethanol/water droplet injected into ethanol-saturated squalane with monoolein, the droplet will absorb ethanol from the continuous phase and increase volume. The propulsion velocity of such a droplet is lower than it in squalane/monoolein without ethanol ($\sim$ 3 and $\sim$ 10 $\mu$m/s respectively). In some cases, there are some monoolein-rich 'tiny' ethanol droplets appear around the main droplet, which becomes a shaker and does not swim efficiently. When two droplets are produced with the same condition, they will attract each other in a certain range (Fig. 5.1). This attraction is potentially caused by the ethanol-poor region between the two droplets, which is created by themselves. The distance between the two droplets are plotted as a function of time, which shows that the attraction is stronger when the two droplets are closer. We studied this system as a model of chemotaxis effect.

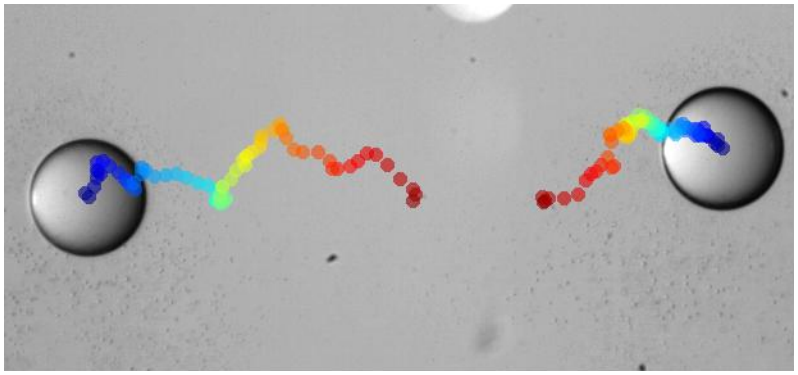

**Figure 5.1: Two droplets swim to each other due to chemotaxis effect.** The droplet moves from blue to red on the color coded trajectory. The radius of the two droplets is about 45 $\mu$m.

## 5.1 Droplets in ethanol-saturated squalane

### 5.1.1 'Tiny' droplet

Once the droplet is produced in a certain parameter range, a large number of micrometer-sized 'tiny' droplets start to appear around the main droplet (Fig. 5.2).

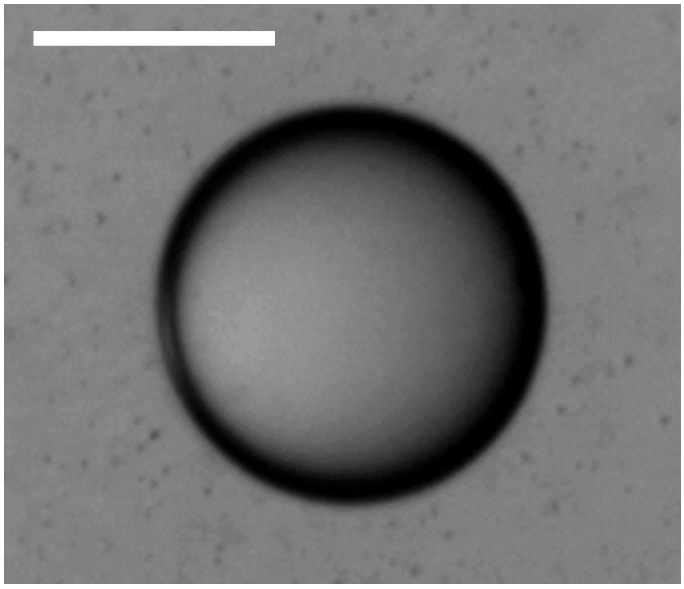

**Figure 5.2: A snap shot of a main droplet surrounded by 'tiny' droplets.** The droplet is made of 70% ethanol and the continuous phase is 100% ethanol saturated squalane. Scale bar is 100 $\mu$m.

Extra NBD is added to the continuous phase to keep track of monoolein/ethanol. As mentioned in 3.2, NBD prefers to go to the ethanol-rich phase, same as monoolein. In the experiment, both the main droplet and these 'tiny' droplets become bright (Fig. 5.3). This means, the main droplet absorb monoolein from squalane and these 'tiny' droplets are ethanol or at least ethanol-rich droplets with monoolein.

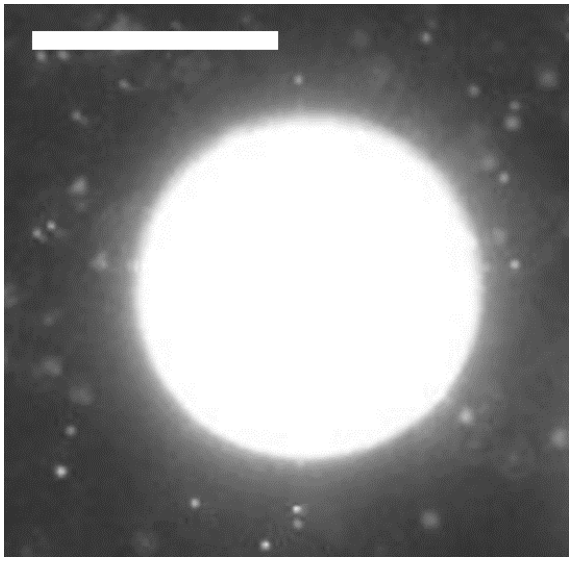

**Figure 5.3: A fluorescent image of a main droplet surrounded by 'tiny' droplets.** 'Tiny' droplets are bright, considered as ethanol droplets with monoolein. The droplet is made of 70% ethanol and the continuous phase is 100% ethanol saturated squalane. Scale bar is 100 $\mu$m.

With the main droplet, the emergence and the amount of 'tiny' droplets is depend on the degree of saturation of squalane. The higher degree of saturation of squalane is, the more 'tiny' droplets emerge. The 'tiny' droplets emergency is barely affected by changing monoolein concentration in squalane from two to seven times CMC (Fig. 5.4).

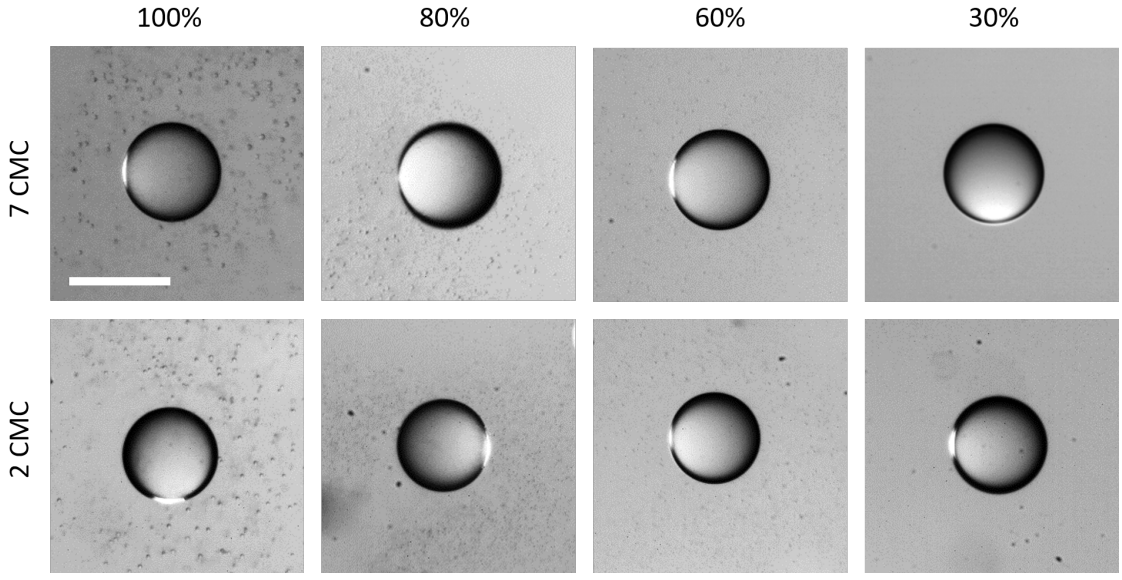


**Figure 5.4: 'Tiny' droplets emergency depends on the ethanol-saturation of squalane.** With 100% saturated oil, 'tiny' droplets are easily visible. With 80% saturated oil, 'tiny' droplets are smaller. With 60 and 30% saturated oil, no 'tiny' droplets are visible. The ethanol concentration in the main droplet is fixed to 50%. All images are taken about 2 minutes after droplet production.

In addition, the higher ethanol concentration in the main droplet, the more 'tiny' droplets emerge. 'Tiny' droplets can be observed with ethanol concentration equal or larger than 50% in the main droplet. There are no 'tiny' droplets around the main droplet with 30% ethanol. For pure water droplet, there is no 'tiny' droplet around, but there is a track made of 'tiny' droplets left behind (Fig. 5.5). Pure water droplets do not show chemotaxis effect and this exceptional case is not further studied.

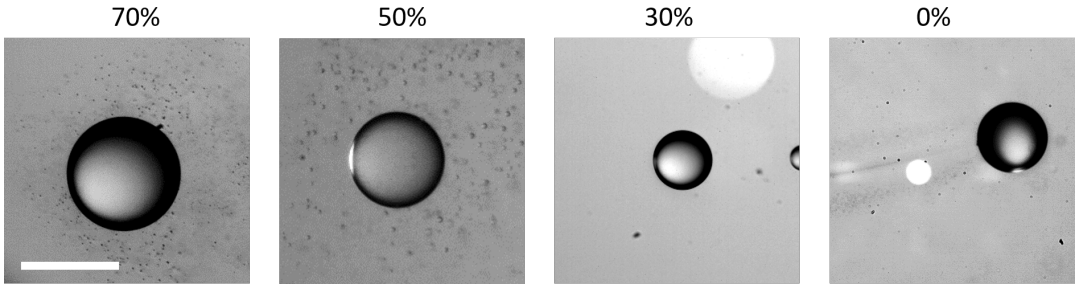


**Figure 5.5: 'Tiny' droplets emergency depends on the ethanol concentration in the main droplet.** Ethanol concentration in the main droplet range from 70% to 0%. The continuous phase is (100%) ethanol saturated squalane. Scale bar is 100 $\mu$m. All images are taken about 2 minutes after droplet production.

### 5.1.2 Volume increase

When the droplet is produced in ethanol-saturated squalane, the droplet volume increases during movement in contrast to chapter 4. Because the radius of the droplet increase about linearly as a function of cruising range (Fig. 5.6), the size increase is presented by the slope of the radius of the droplet as a function of cruising range, which is defined as moving distance divided by initial diameter of the droplet.

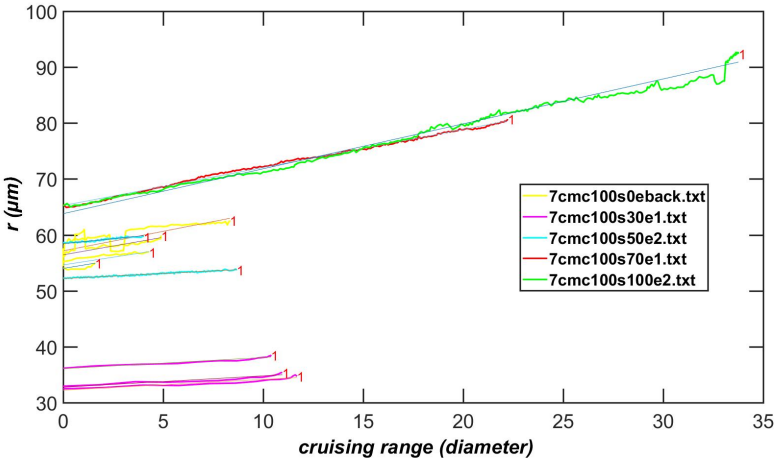


**Figure 5.6: The radius of the main droplets increase linearly as a function of cruising range.** Color coding indicates different ethanol concentration in the droplets. Continuous phase is fixed to 100% ethanol saturated squalane, i.e. 4% ethanol in squalane.

With the volume increase against cruising range, we can not only calculate how much ethanol is absorbed from the continuous phase, but also the width of the path, where the ethanol is depleted (Fig. 5.7). Here we assume that the droplet gain volume by only absorbing ethanol in squalane and the droplet collects all the ethanol (4%) in the trajectory with the width $w$ and the height of the reservoir. In another word, the trajectory become ethanol-depleted area.

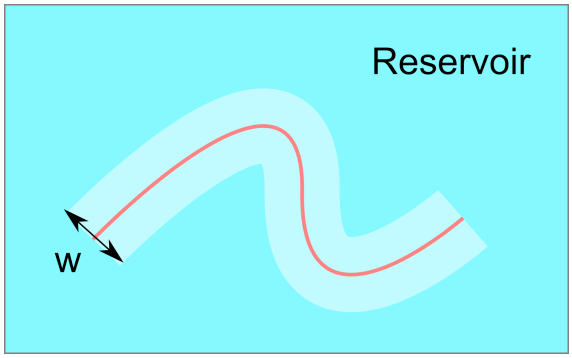


**Figure 5.7: An illustration of a trajectory with a certain width (ethanol depleted area).** The red line indicates the droplet trajectory. The white area indicates the ethanol depleted area.

We notice that the size change of the droplet is correlated to the saturation of squalane and ethanol concentration in the droplet. The higher the ethanol saturation of squalane, the faster the radius of the main droplet increases (Fig. 5.8).

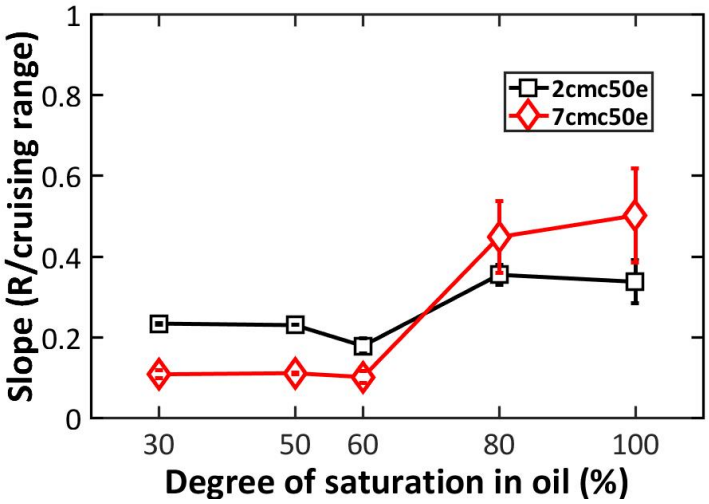


**Figure 5.8: Slopes of radius of the main droplets / cruising range as a function of degree of saturation of squalane.** The ethanol concentration in the main droplet is fixed to 50%. Continuous phases are ethanol saturated squalane with different ethanol saturation and with two times CMC (black) or seven times CMC (red) monoolein.

When the ethanol saturation of squalane is lower or equal to 60%, where there is no 'tiny' droplet, the radius of the main droplet increases slower, with a slope that can be considered as independent from ethanol saturation. When the saturation of squalane is higher or equal to 80%, where 'tiny' droplets appear, the radius of the main droplet increases significantly faster. Comparing the black and red points, which stand for two time and seven times CMC of monoolein in squalane, the monoolein concentration does not affect the radius increase of the main droplet so much. The main droplet is made of 50% ethanol.

On the other hand, the higher ethanol concentration in the droplet, the faster the radius of the droplet increases (Fig. 5.9).

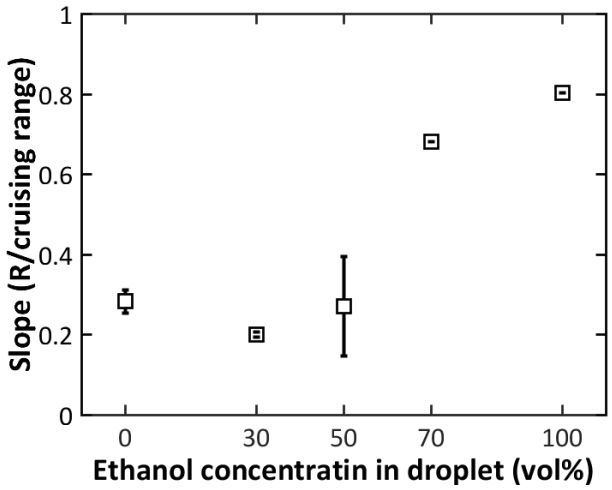


**Figure 5.9: Slope of radius of the droplet / cruising range as a function of ethanol concentration in the droplet.** The continuous phase is fixed to (100%) ethanol saturated squalane with seven times CMC monoolein.

When the ethanol concentration in the droplet is lower or equal to 30%, where there is no 'tiny' droplet around, the radius of the droplet increases slower. When the ethanol concentration in the droplet is higher or equal to 50%, where 'tiny' droplets appear, the radius of the droplet increases significantly faster.

Here we calculate the width of ethanol-depletion track (Fig. 5.7). For the case that the volume of the droplet increases the fastest, the radius a 100% ethanol droplet increases from 65 $\mu$m to 90 $\mu$m after moving 35 times of the initial diameter (cruising range, 4550 $\mu$m) (Fig. 5.6, green line). The height of the reservoir is 200 $\mu$m. We get the width of the trajectory $w = 63$ $\mu$m. This means, a droplet pair will 'feel' and potentially attract each other when the distance is shorter than the trajectory width. If we assume the droplet only absorb part of the 4% ethanol in squalane, the interaction range of the droplet pair will be even larger.

The generation of 'tiny' droplets is a sign of ethanol over saturation in squalane. But meanwhile, the main droplet gain volume by absorbing ethanol in squalane. This seems contradicting but can be explained as following: because ethanol and monoolein have high affinity, they can aggregate in squalane. For the same reason, the main ethanol/water droplet absorb monoolein molecules in squalane fairly quickly (Fig. 5.3). Some of the monoolein molecules in ethanol/monoolein aggregate will go to squalane in equilibrium. The ethanol/monoolein aggregate become unstable and nucleate to 'tiny' droplets.

This fits to the experimental results: the more saturated the squalane is, the more 'tiny' droplets are formed (Fig. 5.4). With higher ratio of ethanol in the main droplet, it has higher affinity to monoolein and absorb it faster, therefore also more 'tiny' droplets are formed (Fig. 5.5).

### 5.1.3 Flow field measured by $\mu$PIV

$\mu$PIV is used to visualize the flow field around the main droplet when 'tiny' droplets appear. In general, the main droplet shakes and the flow field changes completely in a short time. From time to time, the flow field shows the pattern that is comparable to the squirmer model 'shaker': there are four convection rolls around the main droplet. The flow field first goes towards the droplet and then turns away from the droplet with a sharp angle. In Fig. 5.10a, b, the flow fields do not look like the 'shaker'. This could be because the uneven distribution of the 'tiny' droplets.

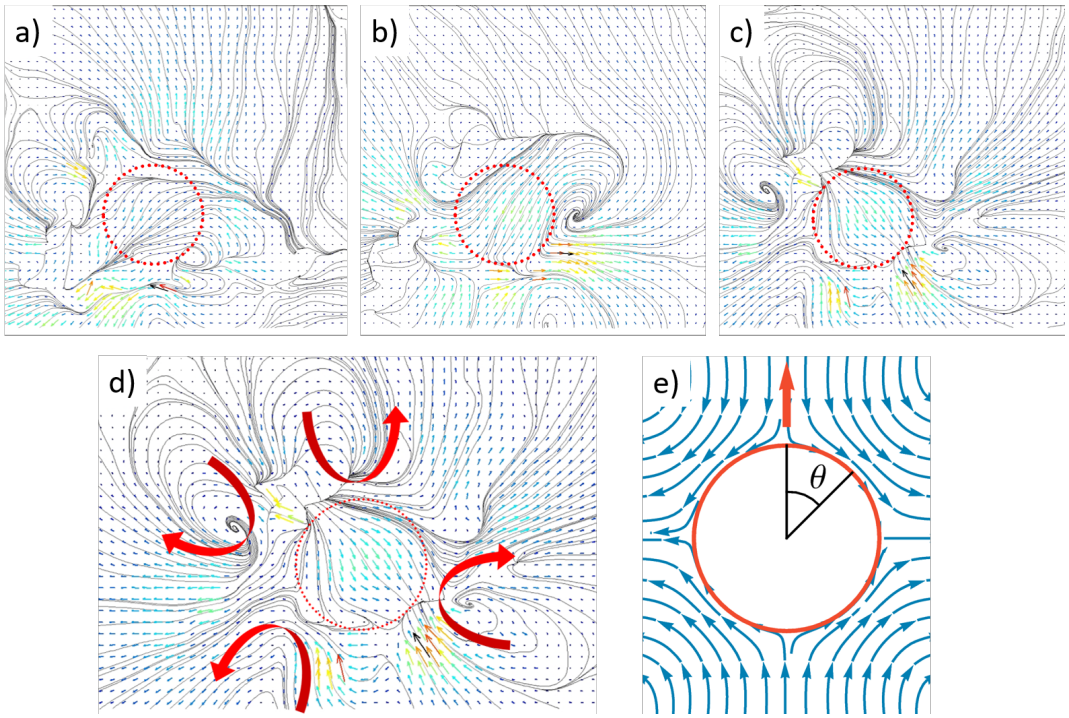


**Figure 5.10: Flow field around the main droplet visualized by $\mu$PIV.** The time interval is one second between each frame. d)-e) Convection rolls around the main droplet (red arrows) comparing to the squirmer model 'shaker'.

## 5.2 Chemotaxis attraction between droplet-pair

By our observation, two droplets are always attracted to each other in ethanol-saturated squalane. The attraction rate is dependent from saturation of ethanol in squalane, monoolein concentration and ethanol concentration in the droplets. To compare the attraction with different parameters, the distance between two droplets from four to two times radius is plotted as a function of time (Fig. 5.11).

Comparing different solid lines or dashed lines, the higher degree of saturation of ethanol in squalane, the faster two droplets attract each other. Comparing the solid lines with dashed lines, the higher the monoolein concentration in squalane, the faster the attraction is.

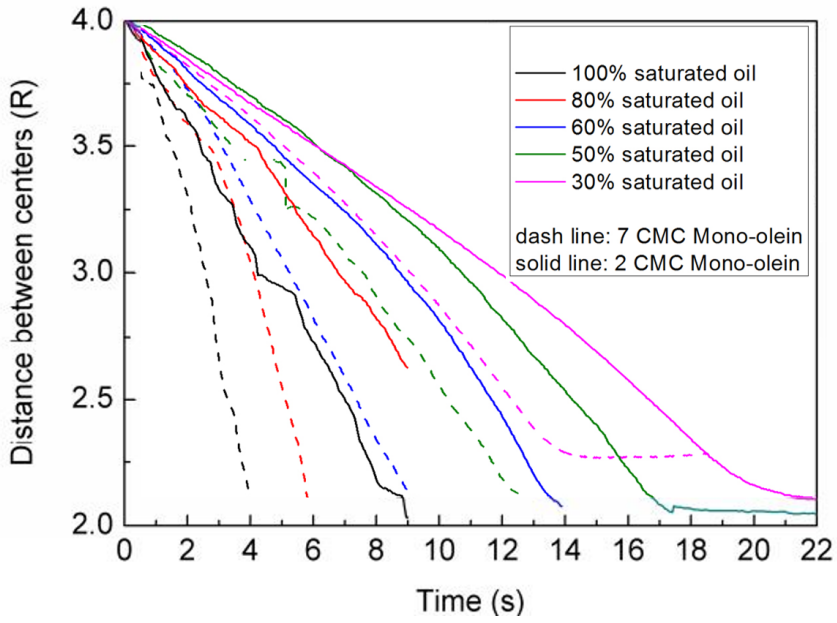


**Figure 5.11: The distance between two droplets as a function of time.** Color coding indicates different degrees of ethanol saturated squalane as the continuous phase. Dashed and solid lines indicate seven times CMC and two times CMC of monoolein in the continuous phase. The ethanol concentration in the main droplets is fixed to 50%. The radius of these droplets are about 50 $\mu$m.

The higher concentration of ethanol in the main droplets is, the more 'tiny' droplets appear, the faster the attraction is (Fig. 5.12).

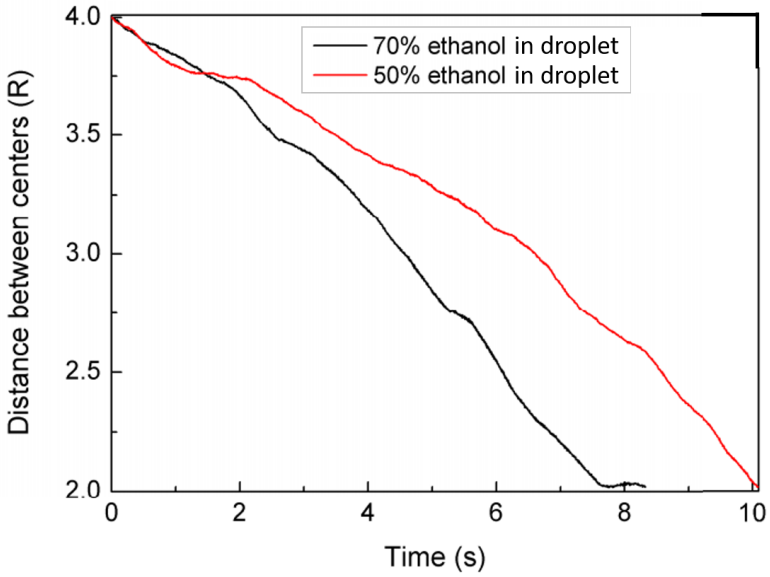


**Figure 5.12: The distance between two droplets as a function of time.** The continuous phase is fixed to 30% ethanol saturated squalane. The main droplets are made of 50% (black) and 70% (red) ethanol. The radius of these droplets are about 35 $\mu$m.

## 5.3 Chemo attraction/repulsion

To understand more about the interaction between two droplets, we demonstrate how single droplets attracted/repelled by controlled chemical gradient.

Half of the reservoir is filled with phase A with droplets (droplets are produced with the second method introduced in chapter 3), the other half of the reservoir is filled with phase B (Fig. 5.13). Both phase A and B are squalane, but with different concentration of monoolein and ethanol. By observing if droplets move from phase A to phase B, we can learn whether the chemical gradient between phase A and B is attractive or repulsive. The ethanol concentration in the droplets is fixed to 70%.

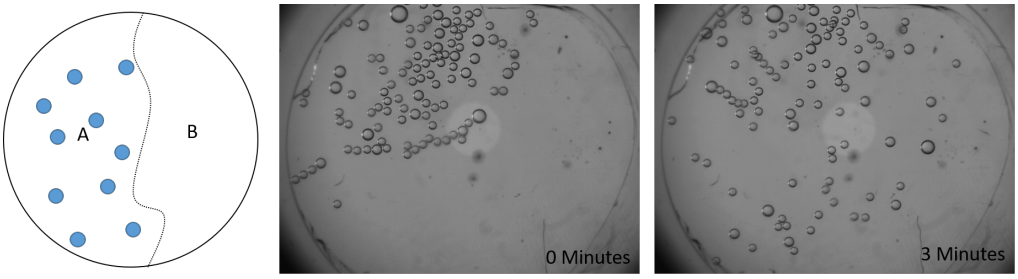


**Figure 5.13: Basic setup: droplets are on one side of a reservoir in phase A and the other half is filled with phase B.** Depending on chemotaxis attraction or repulsion, the droplets avoid entering region B or prefer to enter region B. In the shown example droplets prefer to enter region B.

The result is shown in the table below:

| Number | Phase A | Phase B | Move from A to B |
|---|---|---|---|
| 1 | 3.5mg/ml MO, no ethanol | 3.5mg/ml MO, no ethanol | Y |
| 2.1 | 3.5mg/ml MO, no ethanol | 3.5mg/ml MO with ethanol | N |
| 2.2 | 3.5mg/ml MO with ethanol | 3.5mg/ml MO, no ethanol | Y |
| 3.1 | 3.5mg/ml MO, no ethanol | no MO, no ethanol | N |
| 3.2 | 1mg/ml MO, no ethanol | 3.5mg/ml MO, no ethanol | Y |
| 4.1 | 3.5mg/ml MO, no ethanol | no MO, with ethanol | N |
| 4.2 | 1mg/ml MO, with ethanol | 3.5mg/ml MO, no ethanol | Y |
| 5.1 | 3.5mg/ml MO, with ethanol | no MO, no ethanol | N |
| 5.2 | 3.5mg/ml MO, with ethanol | 1mg/ml MO, no ethanol | Y1 |
| 5.3 | 3.5mg/ml MO, 80% ethanol | 1mg/ml MO, no ethanol | Y2 |
| 5.4 | 3.5mg/ml MO, 50% ethanol | 1mg/ml MO, no ethanol | Y3 |

**Table 5.1: A list of chemical reagent combination for chemotaxis attraction/repulsion test.** Taking the row 2.1 as an example: phase A is squalane with 3.5 mg/ml monoolein without ethanol with droplets, phase B is squalane with 3.5 mg/ml monoolein and saturated with ethanol. The result is, droplets move from phase A to B.

Number 1 is a control test. Droplets will cross to phase B when phase A and B are the same. Comparing number 1.1 and 1.2, when phase B is saturated with ethanol, it prevent droplets moving to phase B. Therefore droplets are repelled by ethanol in squalane. Comparing number 2.1 and 2.2, when the monoolein concentration is higher in phase A, droplets stay in phase A. Therefore droplets are attracted by monoolein in squalane. Number 4.1 and 4.2 show that the effect of monoolein (attraction) and ethanol (repulsion) are added on each other and the attraction/repulsion directions stay the same. Number 5.1 shows that the attraction of monoolein is stronger than the repulsion of ethanol, when phase B has no monoolein. In number 5.2 to 5.4, smaller numbers of droplets can move to phase

B, comparing to the rows above with 'Y'. The number of droplets, that can move to phase B, decreases by decreasing ethanol concentration in phase A.

We can conclude from the experiment above: droplets are attracted by monoolein and repelled by ethanol. When the two effects counter each other, it is depend on the exact concentration gradient and difficult to determine, which effect is significantly stronger.

## 5.4 Mechanism

From the experimental result above, we learned that, droplets are repelled by ethanol in squalane and droplets can absorb ethanol from squalane. Therefore, there will be an ethanol-depleted area around a droplet. Between two droplets, there will be an overlap of the ethanol-depleted area and the two droplets will be attracted to it (Fig. 5.14).

On the other hand, droplets are attracted by monoolein and can absorb monoolein from squalane. But because the monoolein micelle is much bigger than the ethanol molecular, the monoolein-depleted area would be much smaller than the ethanol-depleted area. Therefore, two droplets are still attracted to each other.

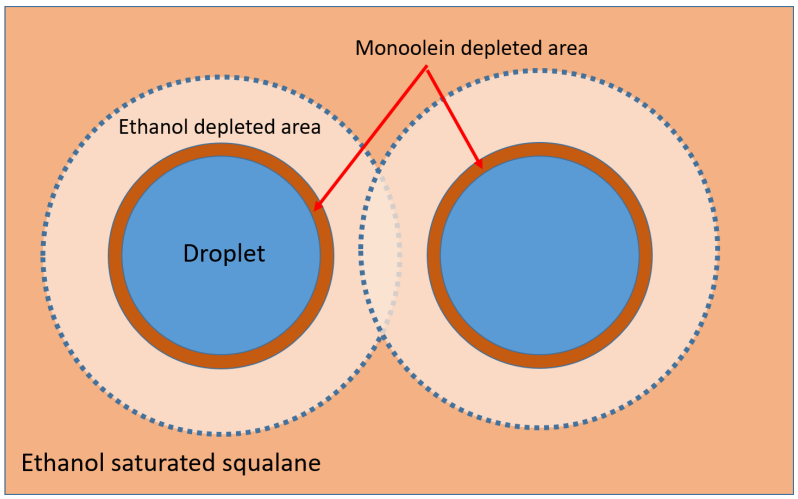


**Figure 5.14: An illustration of ethanol-depleted area (light yellow) and monoolein-depleted area (orange) around two droplets.**

# Chapter 6

# Active cluster

Droplets, which are confined in a reservoir with a low height ratio, which is defined as the height of the reservoir / the average diameter of the droplet and a low area ratio, which is defined as the area of all droplets / the area of the reservoir, typically self-propel randomly (Fig. 6.1a). With large height ratio and area ratio, droplets can form clusters, which barely move but individual droplets are active (Fig. 6.1b). After about 10 minutes since the droplets production, active clusters break up into individual droplets.

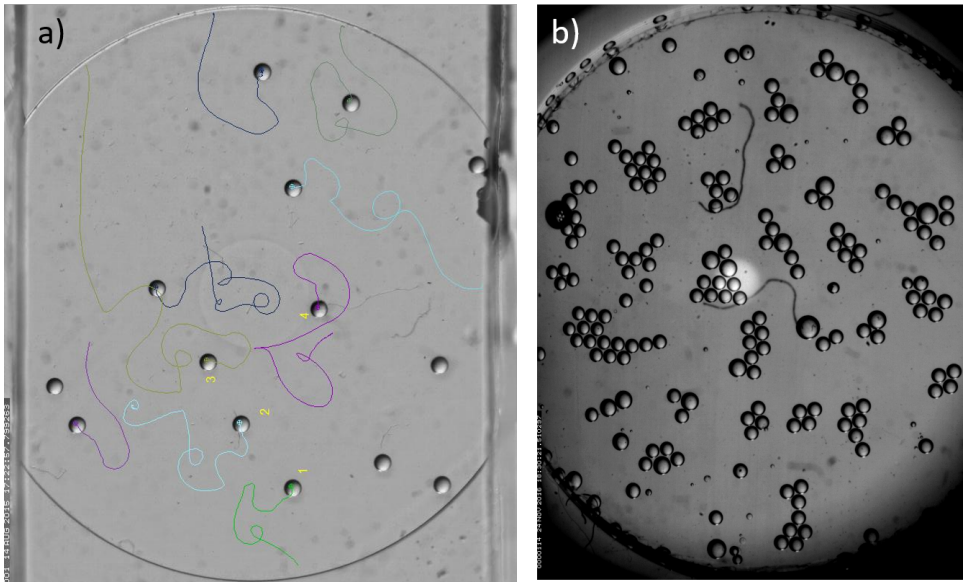


**Figure 6.1: Droplets with different number density in specific confinement.** a) With low number density and high vertical confinement, droplets move randomly. The colorful lines indicate the trajectories of the droplets. b) With high number density and low vertical confinement, droplets form clusters. The droplets are made of 70% ethanol. The radius of the two reservoirs is 6 mm. The heights of the reservoirs are 300 $\mu$m and 600 $\mu$m.

In this chapter, the formation and behavior of active clusters made of droplets are presented. Ethanol concentration of the droplets is fixed to 70%, so droplets move

fairly long (∼10 mins) as a pusher in stage 1 and not likely to attach to the bottom of the reservoir.

## 6.1 Two droplets interaction

Let's first take a look of two droplets interaction with low number density. Two pusher squirmers, i.e. our self-propelled droplets in stage 1, are typically attracted to each other by hydrodynamic interaction. When two pusher droplets encounter each other, they typically reorient to the same moving direction and propel in parallel (Fig. 6.2).

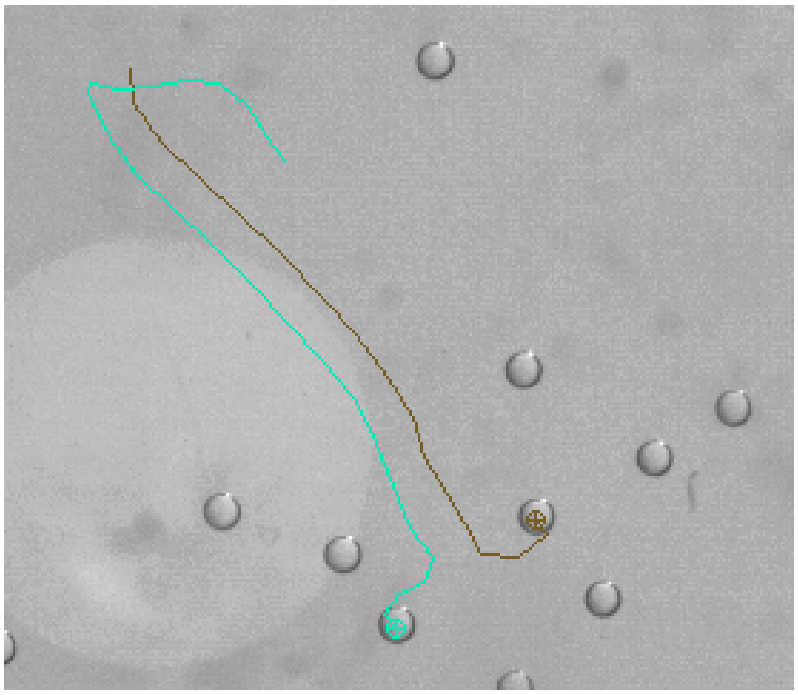

**Figure 6.2: Two droplets encounter, reorient and move in parallel.** The colorful lines shows the trajectories of the droplets. The diameter of the droplets is about 140 $\mu$m.

The reorientation of the droplets is driven by hydrodynamic interaction instead of chemotaxis, otherwise two droplets would avoid each other (Fig. 3.17). This reorientation provides the possibility of cluster formation. By increasing the number density and height of the reservoir, the horizontal confinement is increased and the vertical confinement is decreased. Droplets would tend to reorient upwards after encounter with each other.

## 6.2 Orientation of droplets determined by tracer particles

In case of cluster formation, droplets may lock each other and hardly move, whereas they still propel. To identify the propulsion direction, tracer particles for $\mu$PIV are added to the continuous phase. There are always some tracer particles attached to the surface of the droplet. Together with the Marangoni flow on the surface, tracer particles are transferred to the rear end of the droplet and accumulated. The opposite direction of the particle-accumulated spot is the propulsion direction of the droplet (Fig. 6.3).

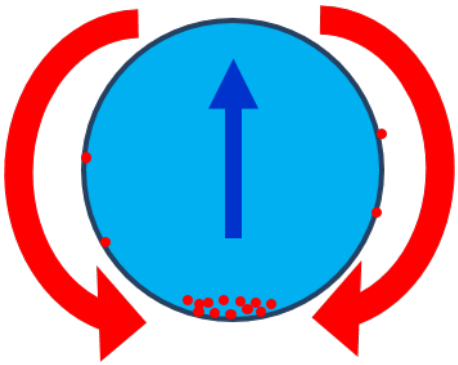

**Figure 6.3: Propulsion direction of a droplet revealed by the particle-accumulated spot.** The red arrows indicates the Marangoni flow on the droplet surface. The red dots indicate tracer particles attached on the droplet interface. The blue arrow indicates the droplet propulsion direction.

When the height ratio is low ($< 2.3$), the particle-accumulated spot is always on one side of the droplet (Fig. 6.4), which means the swimming direction of the droplet is only in 2D. In this case, the area ratio does not play a role and no stable clusters are formed.

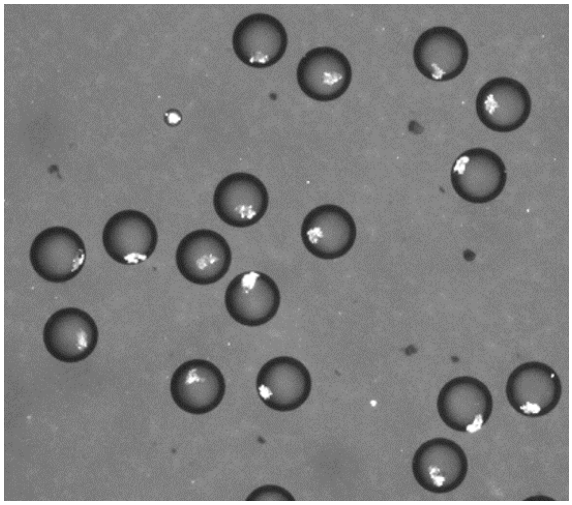

**Figure 6.4: With low height ratio, droplets are oriented to the sides.** The diameters of the droplets are about 240 $\mu$m, the height ratio is about 1.5

With high height ratio ($\approx 3$) and low area ratio ($\approx 0.1$), most droplets are still oriented to the sides at the beginning. After about 2 minutes, the particle-accumulated spot moves gradually to the middle in single droplets with tumbles. When two droplets close up to each other by chance, the particle-accumulated spots slightly away from the center and the propulsion directions of the two droplets point to each other (Fig. 6.5a). In some cases, the propulsion directions are not pointing to the center of the two droplets, the droplet pair turns around the center (Fig. 6.5b,c).

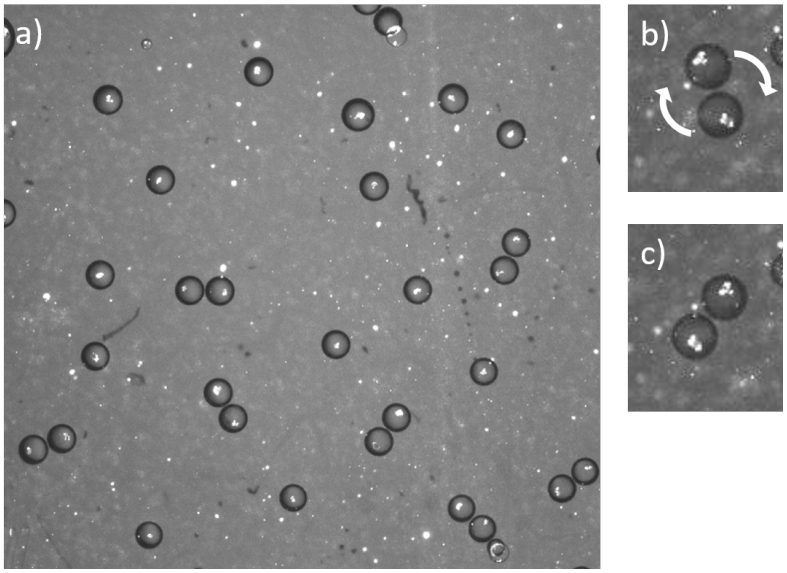


**Figure 6.5: Particle-accumulated spot in single and double droplets.** The diameter of the droplets in all three snapshots is about 200 $\mu$m, the height ratio is about 3.5. The time interval between b) and c) is 10 second.

With high height ratio ($\approx 3$) and higher area ratio ($\approx 0.2$), most droplets are also oriented to sides at the beginning (Fig. 6.6a). But then droplets turn to upwards gradually and tumble like a roly poly toy (Fig. 6.6b). By chance, these droplets close up and form a cluster (Fig. 6.6c, d).

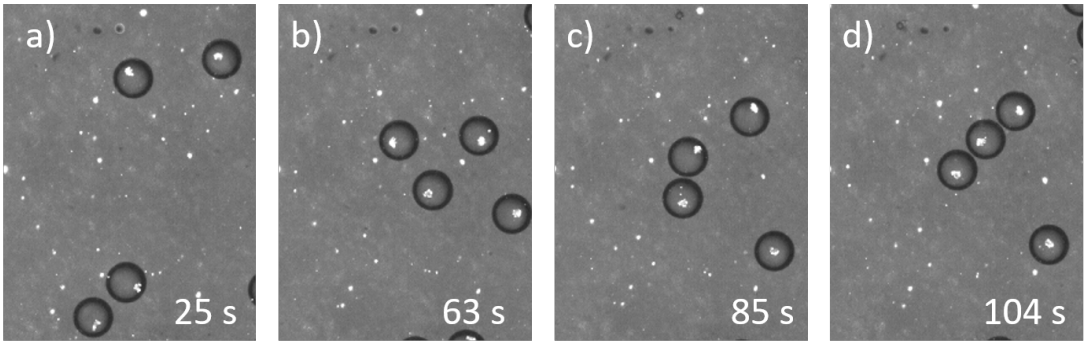


**Figure 6.6: Time series of a cluster formation.** The diameters of the droplets are about 210 $\mu$m, the height ratio is about 3.5.

After 1-2 minutes of the cluster formation, individual droplets become stable and the particle-accumulated spots stay at the same place. In a long-shaped cluster,

the particle-accumulated spots are in the center of each droplet (Fig. 6.7a). In a round-shaped cluster, the particle accumulated spot is in the center of the droplet, which is in the middle of the cluster. (The droplet in the center is out of focus, which could be because of the pushing and squeeze by the neighbor droplets.) For the droplets on the edge of the cluster, the particle accumulated spot is slightly away from the center to the outside of the cluster (Fig. 6.7b).

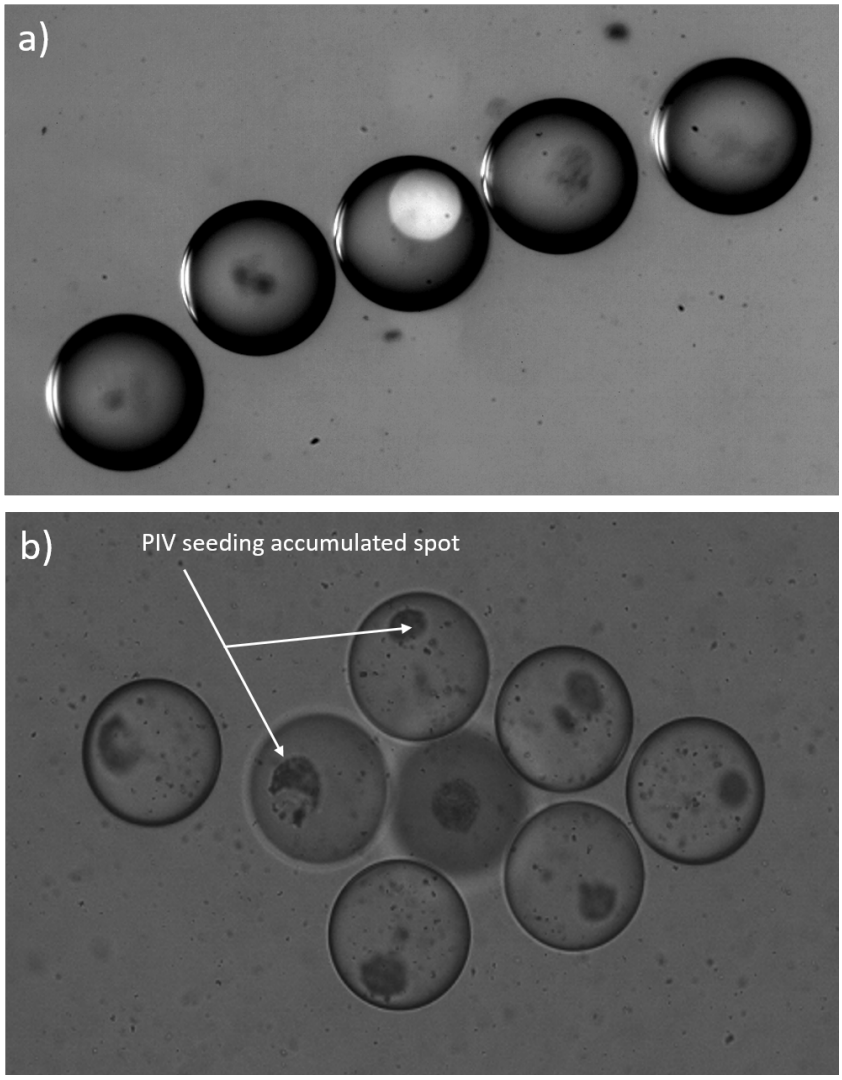


**Figure 6.7: Snap shot of a) an elongated cluster and b) a round-shaped cluster.** Tracer particles accumulate in the middle of each droplet in a) and on the outside of the cluster in b). The droplet diameters in both images are about 200 $\mu$m.

When the particle-accumulated spot is in the middle of the droplet, it means the propulsion direction is either upwards or downwards. During the focusing of the microscope on the active cluster, it was found that the tracer particle accumulated spot is lower than the center plate. So it determines that the individual droplets propels upwards (Fig. 6.8).

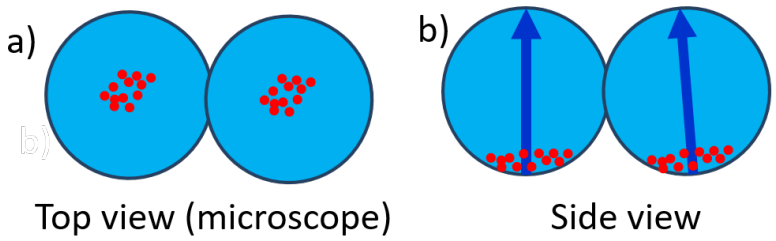


**Figure 6.8: A sketch of an active cluster with tracer particles.** Tracer particles accumulate at the bottom of the droplets, which indicates that individual droplets swim upwards.

When the particle-accumulated spot is slightly away from the center, the propulsion direction is tilted upwards, which means it has a horizontal component. In Fig. 6.5b,c, the horizontal component of the two droplets create a torque and turn around the center. In Fig. 6.7, the droplets on the edge tend to move towards the center.

## 6.3 Flow field measured by $\mu$PIV

For now, we learned that, the active clusters are formed in 3D. It is important to determine the flow field around the clusters, which could be the factor maintaining the structure of the clusters. $\mu$PIV is used to measure the flow field around the active clusters at different height sections. The flow field changes by changing focus of the microscope on z-direction. When the focus is above the top edge of the cluster (blue dashed line), the cluster is a sink (Fig. 6.9b). When the focus is below the top edge, the flow field shows the cluster is a source (Fig. 6.9c).

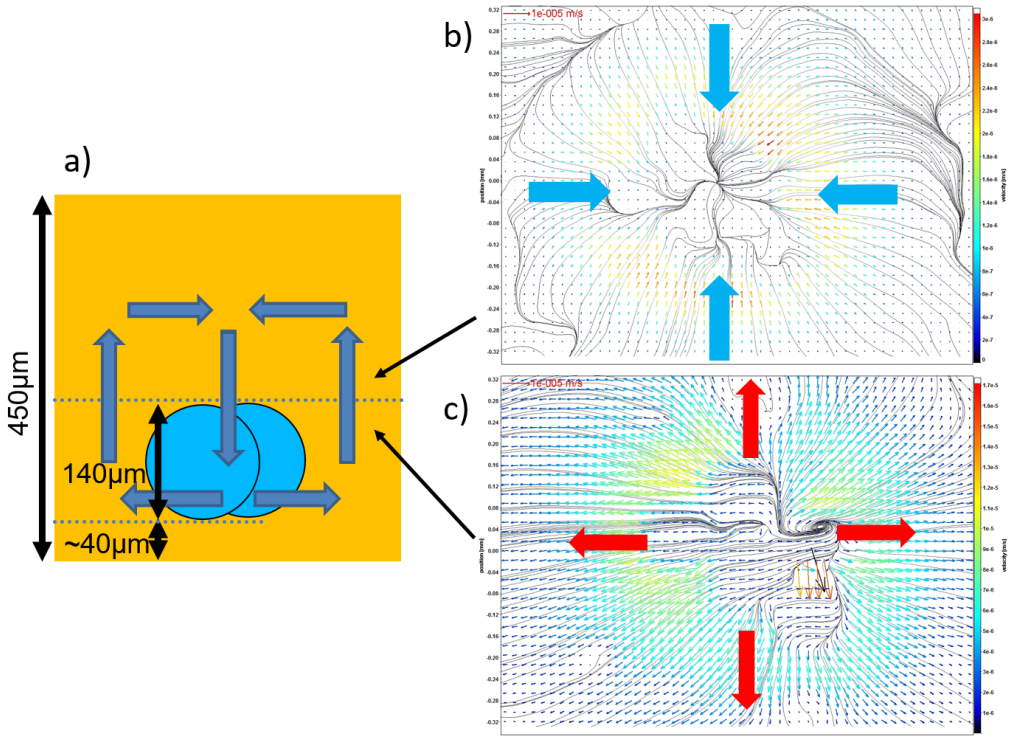


**Figure 6.9: Flow field around a cluster measured by PIV.** a) A sketch of the flow field (dark blue arrows) around a cluster from side view. b) The flow field is a 'sink' above the cluster. c) The flow field is a 'source' below the cluster. The depth of correlation of the microscope is about 15 $\mu$m.

In addition, during the change of the focus, the distance between the center plane of the active cluster and the bottom of the reservoir can be read from the microscope. So the active cluster hoovers above the bottom instead of standing on it. The density of 70% ethanol is higher than the density of squalane (0.89 and 0.81 $g/cm^{-3}$,). In combination with the flow field, we can determine that there is a convection flow around the active cluster, with outflow from below the top edge of the cluster and influx from above the top edge (Fig. 6.9a).

Each cluster stays in a 'cell', which is defined by the convection flow. Such cells can be visualized by tracer particles. The density of the tracer particles is higher than the continuous phase, so some of the particles will sediment along the convection flow. There is a dead-zone between two cells, where the flow is very weak and there is no tracer particles sediment (Fig. 6.10).

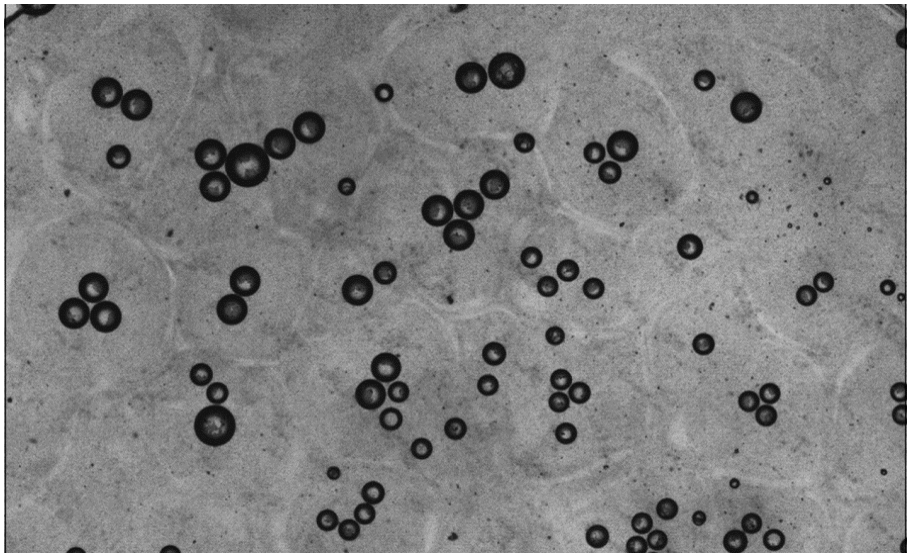

**Figure 6.10: Cells visualized by tracer particles sediment.** Bigger droplets are from the merging of two or more smaller droplets.

The border of the cells can also be visualized by the stream lines of the flow field with large field of view (Fig. 6.11).

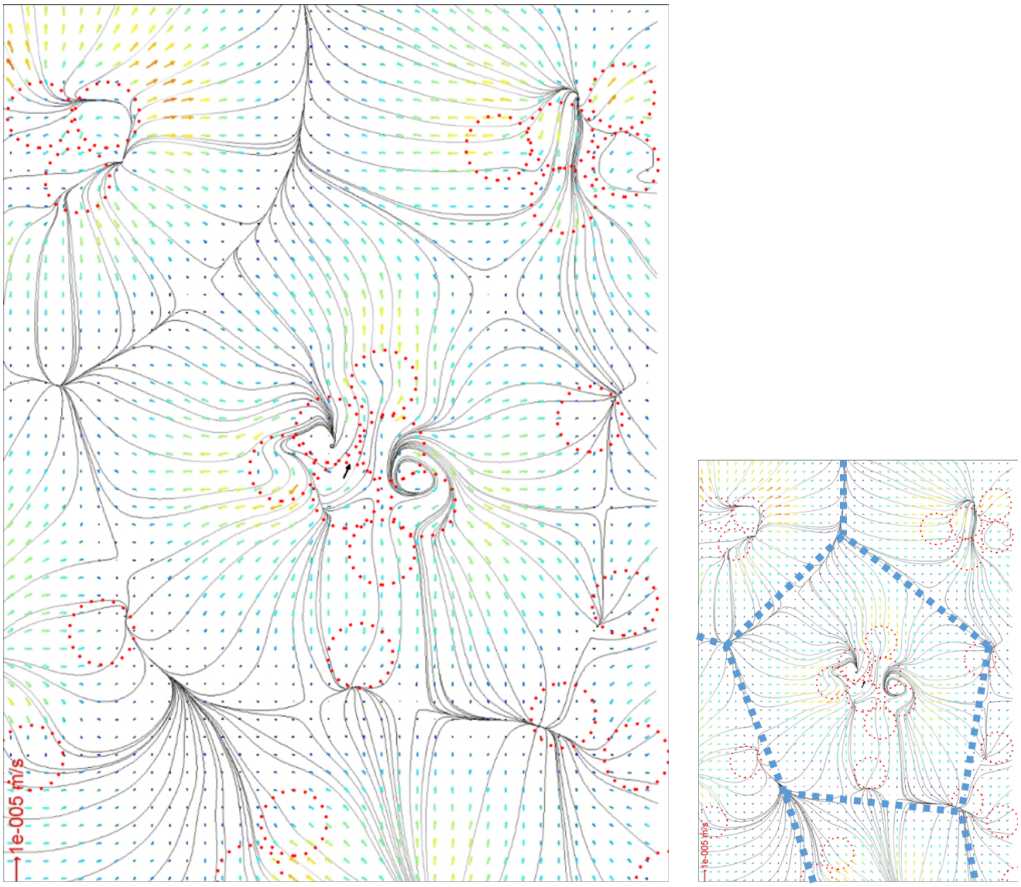


**Figure 6.11: Flow field around a cluster measured by $\mu$PIV.** The border between clusters can be visualized by stream lines. The position of the individual droplets are indicated by red dashed circles, which are added by comparing with the raw fluorescent image. The blue dashed lines help to visualize the border of the cell. The droplet diameters are about 200 $\mu$m.

The shape of such cells is dependent from the shape of the clusters. For the long-shaped clusters, the shape of the cells is also elongated (Fig. 6.12).

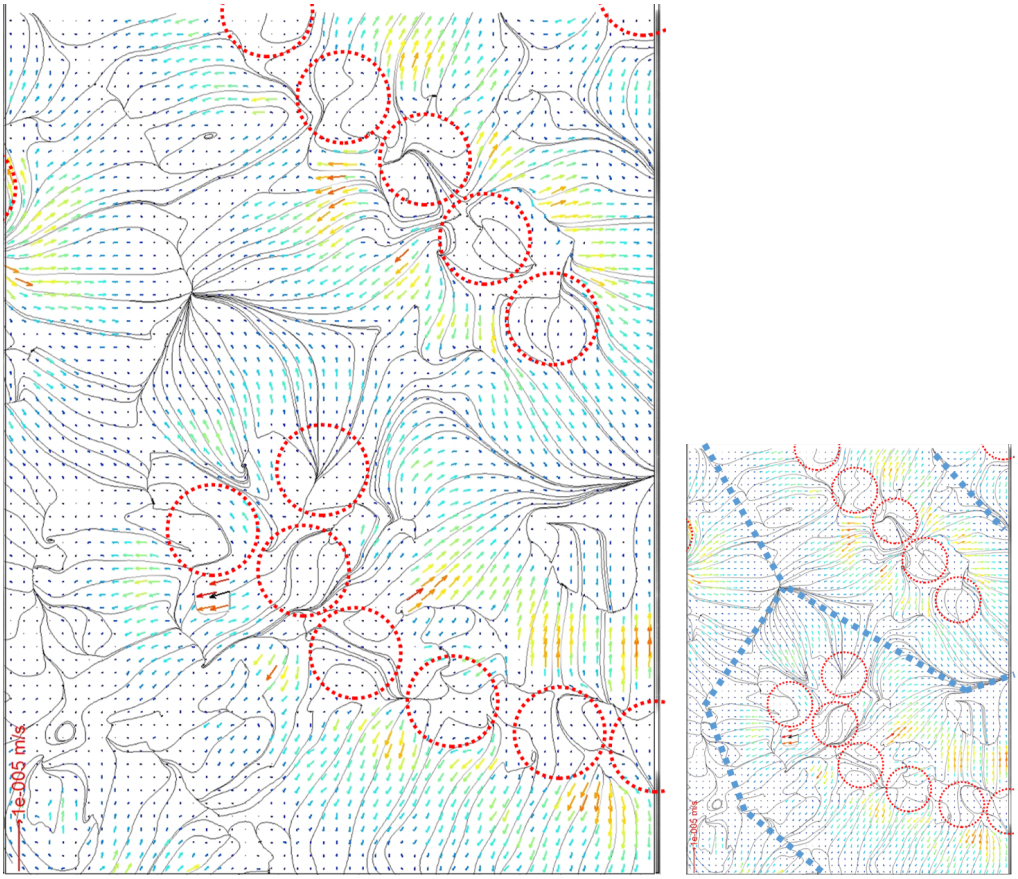


**Figure 6.12: Long-shaped clusters with long-shaped cells visualized by stream lines.** The position of the individual droplets are indicated by red dashed circles. The blue dashed lines help to visualize the border of the cell. The droplet diameters are about 200 $\mu$m.

The match between the shape of the cluster and the shape of stream lines indicates that the clusters are maintained by the convection flow.

## 6.4 Cluster phase diagram

Here is a global description of the shape of the clusters on a phase diagram as a function of height ratio and area ratio.

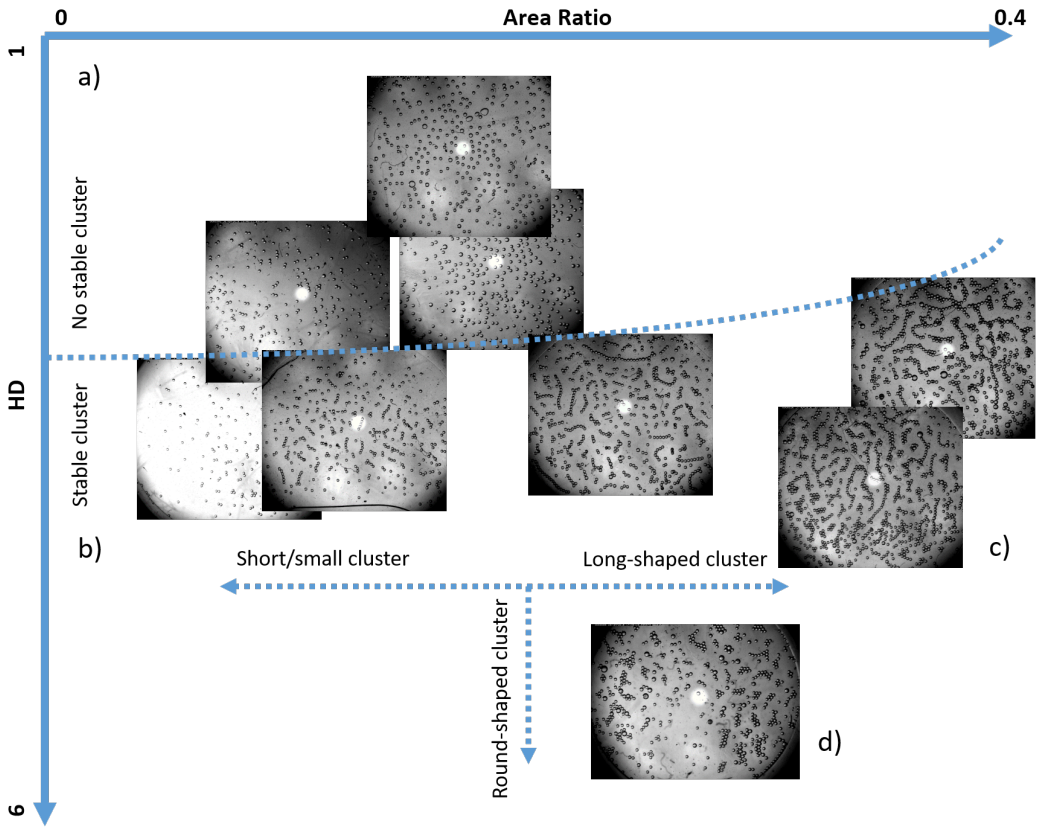


**Figure 6.13: Cluster phase diagram**

With a low height ratio ($< 2.3$) and a low area ratio ($< 0.15$), there is no stable cluster formed (Fig. 6.13a). With a low area ratio ($< 0.1$) but high height ratio ($\approx 3$), small and short clusters are formed. In addition, there are also single 'cluster' formed (stable single droplet with certain distance to each other, Fig. 6.13b). With a high area ($> 0.2$), long-shaped clusters are formed (up to 25 droplet in a line, Fig. 6.13c). With highest height ratio, round-shaped clusters are formed (Fig. 6.13d).

Similar work about 'flowing craft' active clusters is reported in [49] (Fig. 1.11b, c), where active clusters made of liquid crystal dropets 'hover' in the continuous phase with different density by confection flow. But in [49], there is no single-droplet cluster reported and the formation of such clusters cannot be fully understood yet.

# Conclusion

In this thesis, a novel self-propelled droplet system made of ethanol/water dispersed in monoolein/squalane is studied. The droplet releases ethanol into the surrounding squalane and uptakes monoolein from there during the movement, which leads to a spontaneous phase separation in the droplet. The evolving motion scheme of the droplet is divided into three stages according to the phase separation. Before phase separation, the droplet is driven by Marangoni flow, which is caused by monoolein absorption and ethanol release. After phase separation, a Janus droplet is formed and it is driven by Marangoni flow from the water-rich leading droplet with lower interfacial tension to the ethanol-rich trailing droplet. The duration time before phase separation, $t_1$, can be controlled by changing the ethanol concentration in the droplet, droplet size and monoolein concentration in squalane. $t_1$ can be calculated with a simple mathematical model by considering monoolein absorption. This provides the possibility to control switching of stages and different swimming modes, which is a pusher before phase separation and a neutral squirmer after phase separation. The driving mechanism of solubilization makes the self-propelled droplet system robust. This allows extra chemical reagent added to the droplet without significantly influencing the movement, which makes the application cargo delivery possible.

We demonstrated that the self-propelled droplet can perform controlled cargo delivery. DNA or RNA, as a demonstrated cargo, can be controlled to accumulate in water-rich phase or ethanol-rich phase during phase separation by adding salt to the droplet. We can control the long-range interaction by switching swimming mode of the droplet and changing the target form, so that the droplet is either attracted or repelled by the target. We can control the short-range interaction by coating the target, so that the droplet is either attached to the target or passing it. This results in controlled cargo delivery.

The self-propelled droplets absorb ethanol when they are dispersed in ethanol-saturated squalane. This supposedly creates an ethanol-depleted area around each droplet and this ethanol gradient is responsible for the chemotaxis attraction between two droplets within a certain distance. This attraction can be increased by increasing monoolein and ethanol concentration in squalane and ethanol concentration in the droplets. We also confirmed that droplets are repelled by ethanol and attracted by monoolein in squalane.

A collective behavior can be observed in the self-propelled droplet system. With certain number density and vertical confinement, droplets spontaneously orient the

propulsion direction upwards by hydrodynamic and build up active clusters. The active clusters are stabilized by the convection flow around them. Clusters with different shapes, including no cluster, 'single' cluster, elongated cluster and round cluster, are controlled by number density and vertical confinement.

# Acknowledgment

First of all, I would like to thank Prof. Ralf Seemann giving me the chance taking PhD in his group. Thanks a lot for the guidance and long discussions during the whole PhD work.

Second, I would like to thank Dr. Jean-Baptiste Fleury. It is never boring working with you and your fancy ideas can always surprise me and make break through.

Many thanks to theorist Dr. Martin Brinkmann. Your thoughtful theories and strict requirement of experiment make my work solid.

It is great experience working with other research group members. I would like to especially thank Dr. Michael Jung for helping me so much from all aspect.

Last but not least, I would like to thank the exchange student Mahmoud Hosseinzadeh providing me tons of interesting results for chemotaxis.

# Bibliography


[1] A. van Leewenhoeck. Observations, Communicated to the Publisher by Mr. Antony van Leewenhoeck, in a Dutch Letter of the 9th of Octob. 1676. *Philosophical Transactions of the Royal Society of London*, 12(133-142):821–831, jan 1677.

[2] C M Diesing. *Revision der Prothelminthen: Abtheilung: Amastigen (Schluss) : (vorgelegt in der Sitzung vom 14. December 1865)*. Gerold, 1866.

[3] I. Ibanez-Tallon. To beat or not to beat: roles of cilia in development and disease. *Human Molecular Genetics*, 12(90001):27R–35, 2003.

[4] E. M. Purcell. Life at low Reynolds number. *American Journal of Physics*, 45(1):3–11, 1977.

[5] Marco Polin, Idan Tuval, Knut Drescher, J. P. Gollub, and Raymond E. Goldstein. Chlamydomonas Swims with Two. *Science*, 325(2009):487, 2009.

[6] Raymond E. Goldstein, Marco Polin, and Idan Tuval. Noise and Synchronization in Pairs of Beating Eukaryotic Flagella. *Physical Review Letters*, 103(16):1–4, 2009.

[7] Raymond E. Goldstein, Marco Polin, and Idan Tuval. Emergence of synchronized beating during the regrowth of eukaryotic flagella. *Physical Review Letters*, 107(14):1–5, 2011.

[8] David M Woolley. A novel motility pattern in quail spermatozoa with implications for the mechanism of flagellar beating. *Biology of the cell*, 99:663–675, 2007.

[9] D. M. Woolley, R. F. Crockett, W. D. I. Groom, and S. G. Revell. A study of synchronisation between the flagella of bull spermatozoa, with related observations. *Journal of Experimental Biology*, 212(14):2215–2223, 2009.

[10] Nicholas C Darnton, Linda Turner, Svetlana Rojevsky, and Howard C Berg. On Torque and Tumbling in Swimming Escherichia coli. *Journal of Bacteriology*, 189(5):1756–1764, 2007.

[11] Linda Turner, William S. Ryu, and Howard C. Berg. Real-time imaging of fluorescent flagellar filaments. *Journal of Bacteriology*, 182(10):2793–2801, 2000.

[12] Panteleimon Rompolas, Ramila S. Patel-King, and Stephen M. King. An outer arm dynein conformational switch is required for metachronal synchrony of motile cilia in planaria. *Molecular Biology of the Cell*, 21(21):3669–3679, 2010. PMID: 20844081.

[13] P M Rao. Mathematical Model for Unsteady. I(I):839–851, 1988.

[14] J.˜R.˜Blake. A shperical envelope approach to cilary propulsion. *J.Fluid.Mech.*, 46:199–208, 1971.

[15] Lailai Zhu, Eric Lauga, and Luca Brandt. Self-propulsion in viscoelastic fluids: pushers vs. pullers. pages 1–28, 2012.

[16] C Casagrande, P Fabre, E Raphael, and M Veyssie. Janus Beads - Realization and Behavior At Water Oil Interfaces. *Europhysics Letters*, 9(3):251–255, 1989.

[17] John L Anderson, Dennis C Prieve, Peter O Staffeld, John A Quinn, and A N D D C Prieve. Separation and Purification Reviews Diffusiophoresis : Migration of Colloidal Particles in Gradients of Solute Concentration. *Journal of Colloid and Interface Science*, 130(March 2012):37–41, 1989.

[18] Ramin Golestanian, Tanniemola B. Liverpool, and Armand Ajdari. Propulsion of a molecular machine by asymmetric distribution of reaction products. *Physical Review Letters*, 94(22):1–4, 2005.

[19] Jonathan R. Howse, Richard A.L. Jones, Anthony J. Ryan, Tim Gough, Reza Vafabakhsh, and Ramin Golestanian. Self-Motile Colloidal Particles: From Directed Propulsion to Random Walk. *Physical Review Letters*, 99(4):8–11, 2007.

[20] Stephen J. Ebbens and Jonathan R. Howse. Direct observation of the direction of motion for spherical catalytic swimmers. *Langmuir*, 27(20):12293–12296, 2011.

[21] Hong Ren Jiang, Natsuhiko Yoshinaga, and Masaki Sano. Active motion of a Janus particle by self-thermophoresis in a defocused laser beam. *Physical Review Letters*, 105(26):1–4, 2010.

[22] Walter F. Paxton, Ayusman Sen, and Thomas E. Mallouk. Motility of catalytic nanoparticles through self-generated forces. *Chemistry - A European Journal*, 11(22):6462–6470, 2005.

[23] Walter F. Paxton, Paul T. Baker, Timothy R. Kline, Yang Wang, Thomas E. Mallouk, and Ayusman Sen. Catalytically induced electrokinetics for motors and micropumps. *Journal of the American Chemical Society*, 128(46):14881–14888, 2006.

[24] Sumit Gangwal, Olivier J Cayre, Martin Z Bazant, and Orlin D Velev. Induced-Charge Electrophoresis of Metallodielectric Particles. 058302(February):1–4, 2008.

[25] Shashi Thutupalli, Ralf Seemann, and Stephan Herminghaus. Swarming behavior of simple model squirmers. *New Journal of Physics*, 13, 2011.

[26] Martin M. Hanczyc, Taro Toyota, Takashi Ikegami, Norman Packard, and Tadashi Sugawara. Fatty acid chemistry at the oil-water interface: Self-propelled oil droplets. *Journal of the American Chemical Society*, 129(30):9386–9391, 2007.

[27] Taisuke Banno, Rie Kuroha, and Taro Toyota. PH-sensitive self-propelled motion of oil droplets in the presence of cationic surfactants containing hydrolyzable ester linkages. *Langmuir*, 28(2):1190–1195, 2012.

[28] Naoko Ueno, Taisuke Banno, Arisa Asami, Yuki Kazayama, Yuya Morimoto, Toshihisa Osaki, Shoji Takeuchi, Hiroyuki Kitahata, and Taro Toyota. Self-Propelled Motion of Monodisperse Underwater Oil Droplets Formed by a Microfluidic Device. *Langmuir*, 33(22):5393–5397, 2017.

[29] Karthik Peddireddy, Pramoda Kumar, Shashi Thutupalli, Stephan Herminghaus, and Christian Bahr. Solubilization of thermotropic liquid crystal compounds in aqueous surfactant solutions. *Langmuir*, 28(34):12426–12431, 2012.

[30] Stephan Herminghaus, Corinna C. Maass, Carsten Krüger, Shashi Thutupalli, Lucas Goehring, and Christian Bahr. Interfacial mechanisms in active emulsions. *Soft Matter*, 10(36):7008–7022, 2014.

[31] Ziane Izri, Marjolein N. Van Der Linden, Sébastien Michelin, and Olivier Dauchot. Self-propulsion of pure water droplets by spontaneous marangoni-stress-driven motion. *Physical Review Letters*, 113(24):1–5, 2014.

[32] Sébastien Michelin, Eric Lauga, and Denis Bartolo. Spontaneous autophoretic motion of isotropic particles. *Physics of Fluids*, 25(6), 2013.

[33] Chenyu Jin, Carsten Krüger, and Corinna C. Maass. Chemotaxis and autochemotaxis of self-propelling artificial droplet swimmers. 114(20):5089–5094, 2016.

[34] Chenyu Jin, Babak V. Hokmabad, Kyle A. Baldwin, and Corinna C. Maass. Chemotactic droplet swimmers in complex geometries. *Journal of Physics Condensed Matter*, 30(5), 2018.

[35] Krishna Kanti Dey, Satyapriya Bhandari, Dipankar Bandyopadhyay, Saurabh Basu, and Arun Chattopadhyay. The pH taxis of an intelligent catalytic microbot. *Small*, 9(11):1916–1920, 2013.

[36] Larysa Baraban, Stefan M Harazim, Samuel Sanchez, and Oliver G Schmidt. Angewandte Chemotactic Behavior of Catalytic Motors in Microfluidic Channels **. pages 5552–5556, 2013.

[37] Larysa Baraban, Robert Streubel, Denys Makarov, Luyang Han, Dmitriy Karnaushenko, Oliver G. Schmidt, and Gianaurelio Cuniberti. Fuel-free locomotion of janus motors: Magnetically induced thermophoresis. *ACS Nano*, 7(2):1360–1367, 2013.

[38] Victor Garcia-gradilla, Jahir Orozco, Sirilak Sattayasamitsathit, Fernando Soto, Ashley Pourazary, Adlai Katzenberg, Wei Gao, Yufeng Shen, and Joseph Wang. Functionalized Ultrasound-Propelled Magnetically- Guided Nanomotors : Towards Practical Biomedical Applications. 2013.

[39] Li Zhang, Tristan Petit, Yang Lu, Bradley E. Kratochvil, Kathrin E. Peyer, Ryan Pei, Jun Lou, and Bradley J. Nelson. Controlled propulsion and cargo transport of rotating nickel nanowires near a patterned solid surface. *ACS Nano*, 4(10):6228–6234, 2010.

[40] Saverio E. Spagnolie and Eric Lauga. Hydrodynamics of self-propulsion near a boundary: predictions and accuracy of far-field approximations. *Journal of Fluid Mechanics*, 700:105–147, 2012.

[41] Gao Jin Li and Arezoo M. Ardekani. Hydrodynamic interaction of microswimmers near a wall. *Physical Review E - Statistical, Nonlinear, and Soft Matter Physics*, 90(1):1–12, 2014.

[42] Saverio E. Spagnolie, Gregorio R. Moreno-Flores, Denis Bartolo, and Eric Lauga. Geometric capture and escape of a microswimmer colliding with an obstacle. *Soft Matter*, 11(17):3396–3411, 2015.

[43] Juliane Simmchen, Jaideep Katuri, William E. Uspal, Mihail N. Popescu, Mykola Tasinkevych, and Samuel Sánchez. Topographical pathways guide chemical microswimmers. *Nature Communications*, 7(May 2015):1–9, feb 2016.

[44] Ethayaraja Mani and Hartmut Löwen. Effect of self-propulsion on equilibrium clustering. *Physical Review E - Statistical, Nonlinear, and Soft Matter Physics*, 92(3):1–7, 2015.

[45] Andreas Zöttl and Holger Stark. Hydrodynamics determines collective motion and phase behavior of active colloids in quasi-two-dimensional confinement. *Physical Review Letters*, 112(11):1–5, 2014.

[46] Arthur A. Evans, Takuji Ishikawa, Takami Yamaguchi, and Eric Lauga. Orientational order in concentrated suspensions of spherical microswimmers. *Physics of Fluids*, 23(11):2–6, 2011.

[47] Aparna Baskaran and M. Cristina Marchetti. Statistical mechanics and hydrodynamics of bacterial suspensions. *Proceedings of the National Academy of Sciences*, 106(37):15567–15572, 2009.

[48] Carsten Krüger, Christian Bahr, Stephan Herminghaus, and Corinna C. Maass. Dimensionality matters in the collective behaviour of active emulsions. *European Physical Journal E*, 39(6), 2016.

[49] Jeremie Palacci, Stefano Sacanna, Asher Preska Steinberg, David J Pine, and Paul M Chaikin. Living Crystals of Light-Activated Colloidal Surfers. 579(2005), 2012.

[50] Ivo Buttinoni, Julian Bialké, Felix Kümmel, Hartmut Löwen, Clemens Bechinger, and Thomas Speck. Dynamical clustering and phase separation in suspensions of self-propelled colloidal particles. *Physical Review Letters*, 110(23):1–5, 2013.

[51] Jing Yan, Ming Han, Jie Zhang, Cong Xu, Erik Luijten, and Steve Granick. Reconfiguring active particles by electrostatic imbalance. *Nature Materials*, 15(10):1095–1099, 2016.

[52] Daniel Kagan, Rawiwan Laocharoensuk, Maria Zimmerman, Corbin Clawson, Shankar Balasubramanian, Dae Kang, Daniel Bishop, Sirilak Sattayasamitsathit, Liangfang Zhang, and Joseph Wang. Rapid delivery of drug carriers propelled and navigated by catalytic nanoshuttles. *Small*, 6(23):2741–2747, 2010.

[53] J.M. Andreas, E.A. Hauser, and W.B. Tucker. Boundary tension by pendant drops. *The journal of physical chemistry*, 42(1984):1001–1019, 1938.

[54] Drew Myers. Surfactant science and technology, third edition. *Surfactant Science and Technology, 3rd Edition, by Drew Myers, pp. 400. ISBN 0-471-68024-9. Wiley-VCH , October 2005.*, 10 2005.

[55] Milton J. Rosen and Joy T. Kunjappu. *Surfactants and Interfacial Phenomena* -. John Wiley and Sons, New York, 4. aufl. edition, 2012.

[56] *Rayleigh-benard Convection: Structures And Dynamics* -. World Scientific, Singapur, 1998.

[57] Alexandre Joel Chorin. *The Numerical Solution of the Navier-Stokes Equations for an Incompressible Fluid* -. FRANKLIN CLASSICS TRADE Press, 2018.

[58] Henry Shaw. *Investigation of the nature of surface resistance of water and of stream-line motion under certain experimental conditions*, volume 40. 1898.

[59] Pep Español, Miguel A. Rubio, and Ignacio Zúñiga. Scaling of the time-dependent self-diffusion coefficient and the propagation of hydrodynamic interactions. *Phys. Rev. E*, 51:803–806, Jan 1995.

[60] J. K. G. Dhont. *An Introduction to Dynamics of Colloids* -. Elsevier, Amsterdam, 1996.

[61] Keith J. Laidler. *Physical chemistry* -. Benjamin/Cummings Pub. Co., Amsterdam, new edition edition, 1982.

[62] Jozef Markos. *Mass Transfer in Chemical Engineering Processes*. BoD – Books on Demand, Norderstedt, 2011.

[63] Suhas V. Patankar. *Numerical Heat Transfer and Fluid Flow* -. CRC Press, Boca Raton, Fla, 1980.

[64] Takuji Ishikawa. Suspension biomechanics of swimming microbes. (August):815–834, 2009.

[65] Eric Lauga and Thomas R Powers. The hydrodynamics of swimming microorganisms. *Reports on Progress in Physics*, 72(9):096601, aug 2009.

[66] Allison P. Berke, Linda Turner, Howard C. Berg, and Eric Lauga. Hydrodynamic attraction of swimming microorganisms by surfaces. *Physical Review Letters*, 101(3):1–4, 2008.

[67] M. J. Lighthill. On the squirming motion of nearly spherical deformable bodies through liquids at very small reynolds numbers. *Communications on Pure and Applied Mathematics*, 5(2):109–118, 1952.

[68] Jacob Sagiv. Organized monolayers by adsorption. 1. Formation and structure of oleophobic mixed monolayers on solid surfaces. *Journal of the American Chemical Society*, 102(1):92–98, jan 1980.

[69] Todd Thorsen, Richard W. Roberts, Frances H. Arnold, and Stephen R. Quake. Dynamic pattern formation in a vesicle-generating microfluidic device. *Physical Review Letters*, 86(18):4163–4166, 2001.

[70] P. B. Umbanhowar, V. Prasad, and D. A. Weitz. Monodisperse emulsion generation via drop break off in a coflowing stream. *Langmuir*, 16(2):347–351, 2000.

[71] Image pro plus (online). *http://www.mediacy.com/imageproplus*.

[72] Matlab instruction (online). *https://www.mathworks.com/help/images/*.

[73] Matlab instruction (online). *https://www.mathworks.com/help/vision/ref/*.

[74] Ronald J. Adrian. Particle-Imaging Techniques for Experimental Fluid Mechanics. *Annual Review of Fluid Mechanics*, 23:261–304, 1991.

[75] Adam Gasiorowski and Jacek Dutkiewicz. Liquid micellar discontinuous cubic mesophase from ternary monoolein/ethanol/water mixtures. *Annals of Agricultural and Environmental Medicine*, 20(3):606–612, 2013.

[76] Patrick T. Spicer, Kristin L. Hayden, Matthew L. Lynch, Akua Ofori-Boateng, and Janet L. Burns. Novel process for producing cubic liquid crystalline nanoparticles (cubosomes). *Langmuir*, 17(19):5748–5756, 2001.

[77] M. J. Lydon, K. D. Keeler, and D. B. Thomas. Vital DNA staining and cell sorting by flow microfluorometry. *Journal of Cellular Physiology*, 102(2):175–181, 1980.

[78] Marc E Lalande, Victor Ling, and Richard G Miller. Hoechst 33342 dye uptake as a probe of membrane permeability changes in mammalian cells C-O. *Proc. Nati Acad. Sci. USA*, 78(1):363–367, 1981.

[79] V. P. Chuprina, U. Heinemann, A. A. Nurislamov, P. Zielenkiewicz, R. E. Dickerson, and W. Saenger. Molecular dynamics simulation of the hydration shell of a B-DNA decamer reveals two main types of minor-groove hydration depending on groove width. *Proceedings of the National Academy of Sciences*, 88(2):593–597, 1991.

[80] ZBIGNIEW DARZYNKIEWICZ. Differential Staining of DNA and RNA in Intact Cells and Isolated Cell Nuclei wit, Acridine Orange. *Gait and Posture*, 33, 2017.

[81] Veniamin Grigorevich Levich. *Physicochemical Hydrodynamics*. Englewood Cliffs, N.J., Prentice-Hall, 1962, 1962.

[82] J. J. Barlow, A. P. Mathias, R. Williamson, and D. B. Gammack. A simple method for the quantitative isolation of undegraded high molecular weight ribonucleic acid. *Biochemical and Biophysical Research Communications*, 13(1):61–66, 1963.

[83] GUY CATHALA, JEAN-FRANCOIS SAVOURET, BERNARDITA MENDEZ, BRIAN L. WEST, MICHAEL KARIN, JOSEPH A. MARTIAL, and JOHN D. BAXTER. A Method for Isolation of Intact, Translationally Active Ribonucleic Acid. *Dna*, 2(4):329–335, 1983.